

# On the diversity of elasticity exploration for legged robot locomotion

**Doctoral Thesis**

**Author(s):**

Günther, Fabian S.

**Publication date:**

2016

**Permanent link:**

<https://doi.org/10.3929/ethz-a-010796963>

**Rights / license:**

[In Copyright - Non-Commercial Use Permitted](#)

DISS. ETH NO. 23609

# On the diversity of elasticity exploration for legged robot locomotion

A thesis submitted to attain the degree of  
**DOCTOR OF SCIENCES of ETH ZURICH**  
(Dr. sc. ETH Zurich)

presented by

**FABIAN SIEGFRIED GÜNTHER**  
MSc ETH ME, ETH Zurich

born on 25 December 1984  
citizen of Germany

Committee:

Prof. Dr. Fumiya Iida, examiner  
Prof. Dr. Roland Siegwart, co-examiner  
Prof. Dr. Mirko Meboldt, co-examiner

2016



# On the diversity of elasticity exploration for legged robot locomotion

Fabian Siegfried Günther

2016

Compiled November 29, 2016

Department of Mechanical and Process Engineering  
ETH Zürich  
Switzerland

© 2016 Fabian Günther. All rights reserved.

# Abstract

Legged mobile robots can negotiate unstructured terrain, jump over obstacles, and climb on rocks, trees, or buildings. With the ability to go where no wheeled robot can go, legged mobile robots can fulfill a large variety of tasks from household over exploration up to search and rescue missions. However, beside the impressive advances legged robots experienced over the past decades, their performance is still moderate when compared to their biological counterparts. Terrestrial animals cover a similar range of tasks than legged robots, but are still far superior in terms of speed, efficiency, agility and robustness.

Legged locomotion in general requires constant acceleration and deceleration of all parts of the body, which leads to fluctuations in kinetic energy and is a challenge for every actuation system. Most of today's robotic actuators work best at constant speed, and permanent speed changes complicate their control and lower their possible power output and energy efficiency. A way to negotiate this problem is shown by nature, which demonstrates that elastic elements like tendons are an approach to store and recoil energy, which can lead to increased performance and energy efficiency. In legged robots, springs can act as such elastic elements, and many successful concepts for spring implementation have been developed so far. However, exploration of springs in legged robots is still an ongoing process and many possible applications of springs are yet not sufficiently investigated.

In this dissertation, we introduce the general concept of *springy dynamics* to describe different ways springs can be employed in robotic legs. Based on the assumption that an understanding of all possible dynamics is necessary to successfully make use of springs in legged robots, we aim to extend the existing knowledge containing mainly series elastic and passive springy dynamics by investigating two alternative dynamics, namely the preloading and the parallel elastic dynamic.

As a starting point, we extend a conventional series elastic actuator with discrete couplings, which allow for switching between different springy and non-springy dynamics. Based on this mechanism, we then investigate the preloading dynamic, where the leg is locked during flight and the actuator preloads its spring, whose energy is then released during the subsequent stance phase. The series elastic dynamic is used as a comparison to demonstrate that the preloading dynamic can lead to better actuator performance, for example larger hopping height at limited actuator peak force. As a second dynamic, we then investigate parallel elastic actuation. By making use of a specialized robot platform, we demonstrate how the parallel spring can not only improve robustness in open loop monopod running, but also increase energy efficiency of a heavy payload carrier due to body weight support. Together with the very general approach of the coupling extended series elastic actuator from the first part of this dissertation, the specialist robots from the second part represent the whole bandwidth of spring implementation from general to specific approaches.



# Kurzfassung

Laufroboter können sich in sowohl schwierigem Gelände fortbewegen als auch über Hindernisse hinwegspringen oder Felsen, Bäume und Häuserfassaden hinaufklettern. Durch ihre Fähigkeit an Orte vorzustossen die kein Rad- oder Raupenfahrzeug jemals erreichen kann bieten sich Laufroboter für eine Vielzahl von Aufgaben an, welche von Hausarbeit über die Erkundung unbekannter Gebiete bis hin zu Rettungsmissionen reichen. Dennoch, trotz beeindruckender Fortschritte in den letzten Jahrzehnten, können Laufroboter noch nicht annähernd mit ihren biologischen Gegenstücken mithalten. Lauf- und Kriechtiere haben einen ähnlichen Einsatzbereich wie Laufroboter, jedoch sind sie ihnen in Sachen Geschwindigkeit, Effizienz, Agilität und Robustheit immer noch haushoch überlegen.

Laufende Fortbewegung im Allgemeinen verlangt nach dem ständigen Beschleunigen und Abbremsen aller Körperteile, was zu Schwankungen in der kinetischen Energie und zu zusätzlichen Belastungen für die Antriebe führt. Heutige Antriebe funktionieren, ganz im Gegensatz zu Muskeln, am besten bei konstanter Geschwindigkeit, und ständige Geschwindigkeitsänderungen verkomplizieren ihre Regelung, reduzieren die mögliche Leistungsabgabe und verringern die Energieeffizienz. Die Natur löst dieses Problem durch den Einsatz von elastischen Elementen wie Sehnen und Bändern, deren Möglichkeit zur Energiespeicherung sowohl Leistungsabgabe wie auch Energieeffizienz verbessern können. In Laufrobotern können Federn als elastische Elemente eingesetzt werden, und in den vergangenen Jahrzehnten wurden dafür verschiedene erfolgreiche Konzepte entwickelt. Trotzdem ist die Erforschung von Federn für Laufroboter noch längst nicht abgeschlossen, und viele mögliche Anwendungen von Federn sind noch nicht oder noch nicht ausreichend erforscht.

In dieser Dissertation benutzen wir das Konzept der *Federdynamiken*, um verschiedene Einsatzmöglichkeiten von Federn in Roboterbeinen zu beschreiben. Unser Ansatz basiert auf der Annahme, dass eine erfolgreiche Implementierung von Federn in Laufrobotern ein Verständnis aller Federdynamiken verlangt. Als Ergänzung zum bestehenden Wissen, welches hauptsächlich serielle und passive Federdynamiken umfasst, erforschen wir mit der Vorspanndynamik und der parallelen Dynamik zwei alternative Federdynamiken.

Wir starten dafür mit einem konventionellen, seriell elastischen Antrieb und ergänzen diesen durch Kupplungen, welche den Wechsel zwischen verschiedenen Feder- und Nichtfederdynamiken erlauben. Basierend auf diesem Mechanismus beschreiben wir die Vorspanndynamik, bei der der Motor die Feder des blockierten Beines in der Flugphase vorspannt. Die so gespeicherte Energie kann dann für die nachfolgende Standphase verwendet werden. Anhand der seriell elastischen Dynamik als Referenz zeigen wir, dass die Vorspanndynamik zu besserer Performance, namentlich zu höherer Sprunghöhe bei limitierter Motorenkraft führt. Als zweite Dynamik behandeln wir anschliessend die parallel elastische Dynamik. Mithilfe einer spezialisierten Roboterplattform zeigen wir, dass die parallele Feder nicht nur die Robustheit im open-loop gesteuerten einbeinigen Rennen verbessern kann, sondern auch bessere Energieeffizienz bei hoher Zusatzlast erlaubt. Zusammen mit dem allgemeinen Ansatz des kupplungsbasierten, seriell elastischen Antriebes decken die spezialisierten, parallel elastischen Roboter die gesamte Bandbreite der Federnutzung ab, vom allgemeinen bis hin zum spezifischen Ansatz.





# Acknowledgments

During my time as a doctoral student at the Bio-Inspired Robotics Lab, first in Zürich and then in Cambridge, I had the chance to work with many great people whom I would like to thank for their support during the completion of this dissertation.

First, I would like to thank my supervisor Prof. Dr. Fumiya Iida for giving me the opportunity to work with him on many exciting projects during my doctoral studies. He has been my mentor in scientific and philosophical questions, he taught me to think outside the box and his enthusiasm and constant search for new, alternative solutions for the big problems have been a motivation for me to push the limits of both me and my robots.

I would also like to thank my co-examiners, Prof. Dr. Roland Siegwart and Prof. Dr. Mirko Meboldt for their contribution to my dissertation and their valuable feedback on the thesis.

During my studies, I have had the privilege to work with a large group of people due to my times at ETH Zürich and University of Cambridge. I am thankful to Dr. Hung Quy Vu and Fabio Giardina for their prior influence on my research and Dr. Surya G. Nurzaman, Dr. Andre Rosendo, Josie Hughes and Dr. Hugo G. Marques for their collaboration during my studies. I would also like to thank Dr. Liyu Wang and Dr. Luzius Brodbeck who have successfully completed their degrees, and Utku Culha who has been going through the same process as I am, and former members Derek Leach, Xiaoxiang Yu Bryan Anastasiades and Nandan Maheshwari. They all deserve gratitude for sharing their expert knowledge and enriching our lab life. I also would like to thank Ji Hyun Lee and Rahel Haller for keeping the lab running smoothly due to their administrative support.

My research presented in this dissertation has also been shaped by many Bachelor and Master students, whose projects I had the pleasure to supervise. I want to thank Fabio Giardina, Yafeng Shu, Jonathan Hunt and Jia W. Lei for their hard work and excellent Ideas throughout their projects.

Finally, I would like to thank my family and my friends both in Zürich and in Cambridge for their support, for many fruitful discussions and for all the guidance which is necessary when going through such a project.

## Financial Support

This work was supported by the Swiss National Science Foundation Professorship Grant No. PP00P2123387/1, and the ETH Zurich Research Grant ETH-23-10-3.



# Contents

<b>Abstract</b>	<b>i</b>
<b>Kurzfassung</b>	<b>iii</b>
<b>Acknowledgments</b>	<b>v</b>
<b>Preface</b>	<b>xi</b>
<b>1 Introduction</b>	<b>1</b>
1.1 Background . . . . .	1
1.1.1 Elastic elements in the animal kingdom . . . . .	1
1.1.2 Elastic elements in mobile legged robots . . . . .	2
1.1.3 Understanding elastic elements . . . . .	3
1.1.4 Actuating elastic elements . . . . .	3
1.1.5 Limb configurations and springy dynamics . . . . .	6
1.1.6 Controlling elastic elements . . . . .	7
1.1.7 Non steady-state locomotion . . . . .	8
1.1.8 Coupling mechanisms and preloading in nature and robotics . . . . .	9
1.2 Problem statement . . . . .	10
1.3 Hypothesis . . . . .	11
1.4 Contribution . . . . .	11
1.5 Structure of the dissertation . . . . .	12
<b>2 Coupling-based series elastic actuation through linear multimodal design</b>	<b>13</b>
2.1 Introduction . . . . .	15
2.2 Multimodal actuation . . . . .	17
2.2.1 Basic concept of multimodal actuation . . . . .	17
2.2.2 Linear eight-mode actuation . . . . .	17
2.2.3 Characteristics of multimodal actuation . . . . .	19
2.3 Design of the linear multimodal actuator . . . . .	20
2.3.1 LMMA design overview . . . . .	20
2.3.2 Design of the coupling mechanism . . . . .	22
2.4 Modelling and analysis of the LMMA . . . . .	23
2.4.1 Modelling the LMMA . . . . .	23
2.4.2 Impedance switching of the LMMA . . . . .	25
2.4.3 Importance of braking force on actuator performance . . . . .	27
2.5 Stand-alone performance of the LMMA . . . . .	27
2.5.1 Test rig and control architecture of the LMMA . . . . .	27
2.5.2 Clutch performance . . . . .	28
2.5.3 Impedance switch . . . . .	29
2.6 Integration of the LMMA into a robotic leg . . . . .	30
2.6.1 ETH hopping robot . . . . .	30

## CONTENTS

2.6.2	Electronics and control . . . . .	31
2.7	Hopping control strategies . . . . .	31
2.7.1	Series elastic hopping . . . . .	32
2.7.2	Preloaded hopping . . . . .	33
2.8	Physical experiments . . . . .	33
2.8.1	Methods . . . . .	33
2.8.2	Hopping trajectory and stability . . . . .	34
2.8.3	Energy consumption . . . . .	35
2.9	Conclusion . . . . .	36
<b>3</b>	<b>Improving hopping height control of legged robots by using coupling-based series elastic actuation</b>	<b>39</b>
3.1	Introduction . . . . .	40
3.2	Hopping robot template with discrete couplings . . . . .	41
3.2.1	Hopping dynamics and actuation without discrete couplings . . . . .	41
3.2.2	Hopping dynamics and actuation with discrete couplings . . . . .	44
3.3	Simulation experiments . . . . .	46
3.3.1	Mechanical efficiency . . . . .	46
3.3.2	Asymptotic behavior of hopping height . . . . .	47
3.3.3	Hopping height with limited actuator peak force . . . . .	48
3.3.4	Influence of nominal mechanical efficiency to hopping height . . . . .	50
3.3.5	Hopping height controllability . . . . .	51
3.4	Mechanical realization and physical experiments . . . . .	53
3.4.1	Hopping robot platform with discrete couplings . . . . .	53
3.4.2	Parameter extraction . . . . .	57
3.4.3	Physical hopping experiments . . . . .	59
3.5	Discussion . . . . .	63
3.6	Conclusion . . . . .	65
3.7	Simulation results for damping and impact losses . . . . .	65
<b>4</b>	<b>Parallel elasticity for robust and versatile monopod running</b>	<b>69</b>
4.1	Introduction . . . . .	70
4.2	Design and modeling . . . . .	71
4.2.1	Simulation model . . . . .	72
4.2.2	Parameters . . . . .	72
4.2.3	Control strategy . . . . .	72
4.2.4	Hopping pattern . . . . .	72
4.3	Simulation setup . . . . .	72
4.3.1	Ground contact model . . . . .	72
4.3.2	Simulation environment . . . . .	75
4.4	Simulation results . . . . .	75
4.4.1	Stability . . . . .	77
4.4.2	Cost of transport and forward speed . . . . .	77
4.5	Physical experiments . . . . .	78
4.5.1	Physical platform . . . . .	78
4.5.2	Simulation tuning and accordance analysis . . . . .	79
4.6	Conclusion . . . . .	79

<b>5</b>	<b>Improved energy efficiency through body mass support in parallel elastic monopod running</b>	<b>81</b>
5.1	Introduction . . . . .	82
5.2	Design and modeling . . . . .	83
5.2.1	Physical model . . . . .	83
5.2.2	Equations of motion . . . . .	84
5.2.3	Actuation strategy . . . . .	86
5.3	Simulation results . . . . .	87
5.3.1	Simulation setup . . . . .	87
5.3.2	Running dynamics . . . . .	87
5.3.3	Running stability . . . . .	88
5.3.4	Conditions for successful running . . . . .	89
5.3.5	Energetic characteristics . . . . .	90
5.3.6	Forward speed effects . . . . .	90
5.3.7	Influence of payload . . . . .	93
5.4	Physical platform and data acquisition . . . . .	95
5.4.1	Experimental platform . . . . .	95
5.4.2	Data acquisition . . . . .	96
5.5	Experimental results . . . . .	97
5.5.1	Trajectories and running stability . . . . .	97
5.5.2	Natural frequency . . . . .	99
5.5.3	Energetic characteristics and forward speed effects . . . . .	99
5.5.4	Influence of payload . . . . .	100
5.6	Discussion . . . . .	100
5.7	Conclusion . . . . .	103
<b>6</b>	<b>Conclusion and future directions</b>	<b>105</b>
6.1	Contributions of the dissertation . . . . .	105
6.2	Future research and applications . . . . .	106
6.2.1	Coupling-based multi-dynamics Actuation . . . . .	107
6.2.2	Coupling development . . . . .	107
6.2.3	Unify series and parallel elastic actuation . . . . .	107
6.2.4	Complexity Trade-Offs . . . . .	108
<b>A</b>	<b>Comparison between muscles and electric actuation element</b>	<b>111</b>
	<b>Bibliography</b>	<b>127</b>
	<b>List of publications</b>	<b>129</b>
	<b>Curriculum vitae</b>	<b>131</b>



# Preface

The content of this dissertation is based on six peer-reviewed publications. The three conference publications and one journal publication are already published, while another two journal publications are currently under review. All publications have been combined, edited and extended to match the context of this dissertation. It is indicated at the very beginning of each chapter, which publication(s) the content presented is drawn from. These chapters have been written to be self-contained, i.e. they can be read independently. This means on the other hand, that there is some overlap between these chapters. Most of the projects presented in this dissertation were collaborative, thus their content is based on the cooperation with the respective co-authors of the relevant publications, namely Derek Leach, Nandan Maheshwari, Hung Quy Vu, Fabio Giardina, Yafeng Shu and Fumiya Iida.

The publications are:

1. D. Leach, F. Günther, N. Maheshwari, and F. Iida. Linear multimodal actuation through discrete coupling. *IEEE/ASME Transactions on Mechatronics*, 19(3):827–839, 2014
2. F. Günther and F. Iida. Preloaded hopping with linear multi-modal actuation. In *Proc. 2013 IEEE/RSJ Int. Conf. Intelligent Robots and Systems (IROS)*, pages 5847–5852, Tokyo, Japan, 2013
3. F. Guenther, H.Q. Vu, and F. Iida. Improving hopping height control of legged robots by using coupling-based series elastic actuation. *Conditionally accepted for publication in IEEE Transactions on Robotics*
4. F. Günther, F. Giardina, and F. Iida. Self-stable one-legged hopping using a curved foot. In *Proc. 2014 IEEE Int. Conf. Robotics and Automation (ICRA)*, pages 5133–5138, Hong Kong, China, 2014
5. F. Guenther and F. Iida. Energy efficient monopod running with large payload based on open loop parallel elastic actuation. *Accepted for publication in IEEE Transactions on Robotics*
6. F. Günther, Y. Shu, and F. Iida. Parallel elastic actuation for efficient large payload locomotion. In *Proc. 2015 IEEE Int. Conf. Robotics and Automation (ICRA)*, pages 823–828, Seattle, WA, 2015





# Chapter 1

## Introduction

Legged mobile robots face a set of unique challenges due to the way they move. Unlike wheeled machines, which can make use of constantly rotating components, legged locomotion requires constant acceleration and deceleration of all parts of the body as well as dealing with complex hybrid dynamics, including impacts and discrete footholds.

The constant acceleration and deceleration of the body parts of legged robots leads to fluctuations in kinetic energy and is a challenge for the actuation system. Most of today's actuators work best at constant speed, and permanent speed changes complicate their control and lower their possible power output and energy efficiency. A way to negotiate this problem is shown by nature, which demonstrates that elastic elements like tendons are an approach to store and recoil energy, which leads to increased performance [7,8] and energy efficiency [9] of the musculoskeletal systems of animals. In engineering, springs can act as such elastic elements in legged robots and have been explored since the early 80s [10], and many successful concepts for spring implementation have been developed so far [11]. However, exploration of springs in legged robots is still an ongoing process and many possible applications of springs are yet not sufficiently investigated.

The goal of this dissertation is to explore alternative ways of spring usage in legged robots, namely preloading a spring for increased power output and parallel elastic actuation for improved robustness and energy efficiency.

### 1.1 Background

#### 1.1.1 Elastic elements in the animal kingdom

Legged vertebrates show impressive locomotion skills, from traveling distances at high energy efficiency [12], over negotiating unstructured terrain [13], climbing on trees [14] or performing highly agile movements [15]. These capabilities cannot be explained by the properties of their muscles alone. It rather turns out that elastic elements in their musculoskeletal system contribute significantly to the animals performance.

The majority of the elastic elements in vertebrates is arranged in the form of tendons in series to the muscles. Mechanically, tendons represent a passive elastic element, able to store and recoil mechanical energy by lengthening and shortening under load with very low internal dissipation [7, 16]. The muscle contractile elements on the other hand are able to actively shorten and withstand lengthening and therefore act as an actuation element, being able to input and dissipate mechanical energy to and from the animal. Every major muscle contributing to vertebrate locomotion has tendons attached and therefore limb actuation always includes series elasticity. Muscles and tendons are often considered independently, but functionally they are tightly integrated [17]. To emphasize this fact, we will refer to them as *muscle-tendon units* throughout this dissertation.

During locomotion, the series elasticity introduced by the tendons of the muscle-tendon unit

contributes in three major fields [8]:

1. Tendons enable energy conservation by passively lengthening and shortening while for example the animal bounces on the ground during running. While the muscle produces the full tendon force, its necessary contraction distance and therefore its necessary mechanical work is greatly reduced due to the energy conservation in the tendon. For example, both horses and wallabies recover up to 40% of the mechanical work by elastic savings in their tendons [18,19]. In humans, the contribution of tendon strain energy to the positive work generated by the ankle plantar-flexors during sprinting amounts up to 74 % [20].
2. Tendons allow for muscle peak power amplification. If a tendon is preloaded by the active work of muscle contraction, it can release this energy more rapidly than it was stored, and therefore muscle peak power is amplified. This allows for example for increased muscle speed during limb retraction in running [21]. Another example for power amplification are various insects, where preloading enables fast hopping motions [22].
3. Tendons finally allow for rapid energy absorption, for example at touchdown during hopping and running. There the tendon gets lengthened nearly instantly, storing the kinetic energy. The muscle is then lengthening at a slower rate to dissipate this energy [23]. The tendons thereby act as a protection mechanism for the muscle tissue, which itself would not be able to handle the large velocities occurring at impact without injury like strain or muscle fiber rupture [24].

In addition to tendons, there are parallel elastic components in each muscle itself [25–27], which allow the muscle to keep its structural integrity when lengthened passively. Described for example by the three element Hill muscle model [28], these passive components contribute to every muscle contraction above rest length.

Another important application of elasticity in animals is the use of the viscoelastic properties of fat pads for shock absorption [29], for example in the feet of nearly all mammals. The main contribution of this shock absorption lies in improved ground contact and protection of the mechanical structure above the foot [30,31].

Finally, the ligaments of the joint capsule [32] act as an elastic end stop in order to limit the rotational motion of a joint. While this joint capsule can produce high torques at its end positions, its stiffness over the joint work range during normal locomotion is too small to have significant influence on locomotion ([33], Fig 4).

### 1.1.2 Elastic elements in mobile legged robots

In engineering, springs can act as passive elastic elements. In addition to the commonly used coil spring, bow springs and various specialized designs are widely used in legged robotics. The principle is the same as in nature, springs can store and recoil mechanical energy with low internal dissipation and large power amplitudes. In limbs containing of rigid segments, springs can be attached to both telescopic and rotational joints, and in this case we will refer to such a joint as a *springy joint*. Another option is to make a segment or even the whole leg elastic, for example by using bow springs as legs [34,35]. In this case, we will refer to *springy legs* and *springy segments*, respectively. Springy joints, legs and leg segments without further actuation have a fixed rest length (at which the spring is relaxed), and every deviation from this rest length causes a counter-force of the spring.

The basic principles of legged locomotion and therefore the requirements to the springs remain the same for both animals and robots. Legged locomotion requires fluctuations in the kinetic energy of all body parts [36], with the vertical bouncing motion of the main body and the swing motion of the limbs being the main contributors [29]. The exploration of springs for the vertical bouncing started in the early 80s [10] and incorporates telescopic as well as articulated limb designs in monopod [34,37,38], bipedal [39], quadrupedal [40,41] and hexapedal [35] robots.

Apart from bouncing, only few other applications of mechanical energy storage using springs have been explored so far, namely energy transfer from front to hind legs using artificial spines [42], combined bouncing and leg swing in acrobot designs [4, 6] and power amplification through preloading for jumping [43–45] and running robots [2, 34]. Surprisingly, from our best knowledge, springs specifically for leg swing have only been implemented in one robot [46] so far.

To absorb impact shock and to limit joint positions, viscoelastic rubber elements are commonly used on most legged robots. Apart from shock damping, rubber pads allow for increased ground friction and therefore improved power transfer through the legs. According to the definition in the beginning of this section, a segment with a shock absorber can be seen as a springy segment.

### 1.1.3 Understanding elastic elements

From the previous two subsections, one could get the impression that the application of elastic elements in the animal kingdom and springs in legged robots is simple and straight forward, but the appearance is deceiving. While describing elastic elements is one thing, understanding their influence on the animals’ and robots’ dynamics is another.

For the understanding of animal and legged robot locomotion, it turned out to be beneficial to describe both with minimalistic models, also known as templates [47]. These templates aim to model only the very basic properties of locomotion, namely the trajectory of the center of mass (COM) of the agent as well as limb position during stance and the ground reaction force. All other effects, especially specific joint forces or angles, are not considered. Introduced for running [48, 49] and walking [16, 50, 51], these templates helped gaining insight into legged locomotion concerning stability [52], power output [53] and energy efficiency [36]. While walking was first modeled using the inverted pendulum model with rigid legs, recent work [54] showed that the spring loaded inverted pendulum (SLIP), initially established for running, may be suitable to represent walking too.

Out of the study of these templates, the paradigm of passive dynamic walking and running was developed [51, 55]. This paradigm states that the walking and running motion should be determined by the passive dynamics of the robots mechanics, and that actuation should be used only for energy input to compensate for losses. Following this paradigm, legged locomotion with high energy efficiency [56], grace [57] and power output [38] based on some times minimalist design [34] becomes possible.

### 1.1.4 Actuating elastic elements

During legged locomotion, inevitable energy losses like friction and impact occur [58]. In addition, energy input is necessary for accelerating or moving uphill, and deceleration or moving downhill requires energy dissipation. The same holds true for moving outside of the trajectories given by the passive dynamics of the robot, where energy input for acceleration/deceleration of body parts is necessary as well. And finally, balancing especially in uneven terrain needs energy input. Therefore, legged robots need actuation elements for the mechanical energy input and brakes and/or actuation elements for the dissipation of mechanical energy.

Today’s *actuation elements*<sup>1</sup> for autonomous mobile legged robots contain of a motor converting chemical/electrical to mechanical energy (combustion engine or electric motor) and a transmission, usually to reduce the speed and increase the torque of the motor. This transmission can be either mechanical (gearbox) or hydraulic. When comparing usual performance metrics of both muscles and electric motors with gearboxes of similar mass and output torque (Tab. 1.1), one can see that the peak power density, the continuous power density, and the peak

---

<sup>1</sup>In this dissertation, “actuation element” refers to the combination of a motor converting energy and its primary transmission system. Springs are therefore not part of the actuation element itself, but together with the actuation element they form an actuator.

Table 1.1: Typical performance values for muscles and electric actuation elements. A detailed calculation can be found in Appendix A

Parameter	Electric actuation element	Vertebrae muscle
Mass [kg]	2.64	2.245
Continuous power [W/kg]	182	104
Peak power [W/kg]	889	615
Peak torque density [N m/kg]	97	104
Inertia [kg m <sup>2</sup> ]	1.027	0.000917

torque density are of similar magnitudes for both actuation concepts, even though the exact values may vary depending on which muscle and which motor-gearbox combination is reviewed. On the other hand, a difference of several magnitudes can be observed in the inertia of both concepts. While muscles have a relatively low inertia (less than their own mass), a gearbox dramatically increases the rotational inertia of an electric motor. For typical gear ratios around 1:100, the inertia of an actuation element often even much larger than the inertia of the limb this actuation element moves. As a side effect, large gear ratios often lead to poor back-driveability, which again increases the effective inertia. The use of high torque motors with low gear ratios can attenuate these effects [59], but the differences between muscles and actuation elements remain large.

Another striking difference between muscles and actuation elements lies in their scalability. A single motor unit (muscle fibers plus nervous intervention) of a muscle is extremely small and the intervention requires very low space. The medial gastrocnemius muscle, for example, contains around 579 motor units and the biceps up to 774 [60]. Adding up hundreds of individually controlled motor units in a certain volume leads to nearly the same power density as if all these units would have been one big muscle. This allows for very complex design with various small muscles, which eventually move a joint together. For example, the musculus trapezius, although considered as one muscle anatomically, contains of a manifold of motor units, and depending on the activation pattern it is able to move the human shoulder up or down.

While muscles can be scaled, divided or unified without loss in power density, the power density varies massively if the same is done with today’s actuation elements. For example, the smaller an electrical motor unit, the larger bearings or wiring become relative to the total motor volume. In addition, placement of multiple rigid actuation elements becomes complicated and the complexity of the system rapidly goes beyond manageable. Therefore, the musculoskeletal body plan of animals cannot be copied 1:1, but needs to be rethought for a lower number of larger actuation elements.

When actuating a robot with springy joint, three basic configurations become possible, depending if a springy joint is actuated at all and if yes, how the actuation element is placed with respect to the spring of the joint.

**Configuration 1: Series elastic** *Series elastic actuators* (SEA, [61–63], Fig. 1.1e) contain of a spring and an actuation element in series. During operation, spring force and actuation element force are the same<sup>2</sup>, while their motions are independent. Or when starting for a springy joint (see definition in Section 1.1.2), adding an actuation element in series means being able to change the rest length of the springy joint. Series elasticity, which is the main use of elasticity in nature, can be even more beneficial for an actuation element than for a muscle, since it can negotiate the large actuation element inertia. Among others, this might be one of the main reasons while series elastic actuators are popular in today’s legged robots. The advantages

<sup>2</sup>When assuming a spring with low or no inertia.

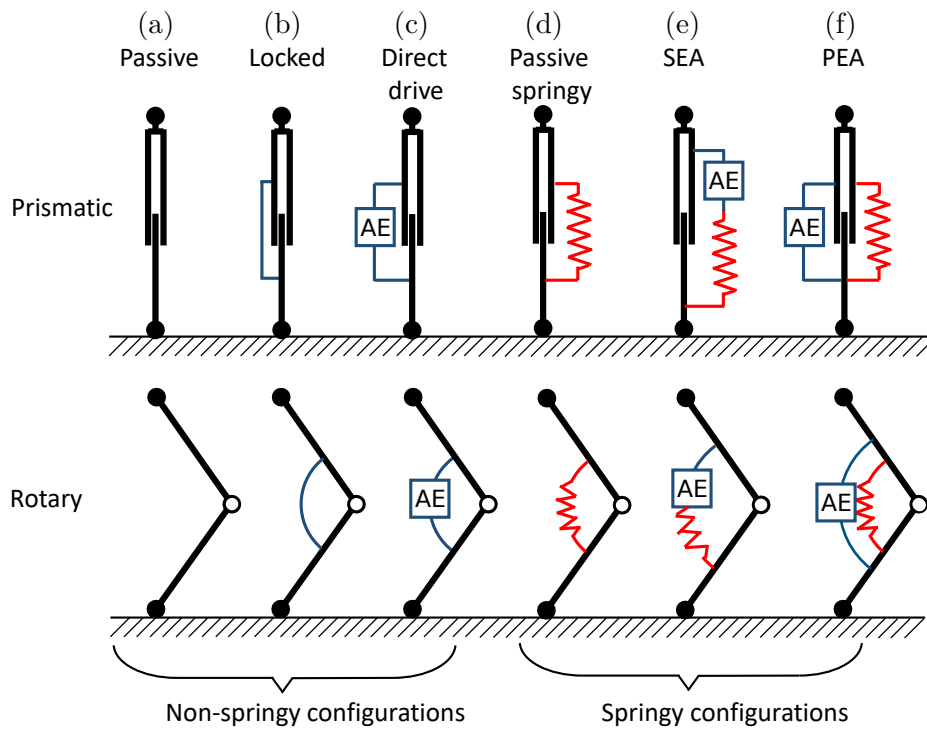


Figure 1.1: Six different joint configurations for both prismatic and rotary robotic limbs. Configurations a-c do not contain a spring and are therefore called non-springy. Configurations d-f show the three basic configurations with whom a spring can be attached to a robotic joint. The passive springy (d) and the parallel elastic (PEA, f) configuration both exhibit one springy dynamic, since every joint position leads to a defined spring force. The series elastic configuration (SEA, e) on the other hand can exhibit multiple springy dynamics, since the actuator length influences the spring force produced for a certain joint angle.

of energy conservation and power amplification (see Section 1.1.1) hold true for series elastic actuation too, and the ability of the spring to absorb impact energy nearly instantly protects the actuation element from damage. In most robotic applications, each joint has one series elastic actuator, which acts in both directions. However, in animals the muscle-tendon units are only able to generate force when pulling (and collapse when being pushed), and are therefore always arranged in an antagonistic setup, pulling on both sides of the joint. Regarding the fact that a “pull-only” actuator is often easier to build, and artificial tendons allow for force transfer over long distances and even multiple joints, antagonistic setups with series elastic actuators have been explored for robots too [64–66].

**Configuration 2: Passive springy** In a robot limb with multiple springy joints, not all joints need to be necessarily actuated. In fact, a common approach is to leave the leg joint (either telescopic, articulated or realized as a bow spring) passive and actuate only the hip joint [35], Fig. 1.1d. This approach allows for having the actuators concentrated at the main body, which allows for robust, lightweight and cheap leg design.

**Configuration 3: Parallel elastic** Without the limits of a specific anatomy, legged robots allow for more freedom in the use of springs and actuators. For example, in a *parallel elastic actuation* setup, an actuator is placed directly to a springy joint, ending up in parallel with the spring (Fig. 1.1f). During operation, the actuation and elastic element’s torque add up, and actuation element and joint motion are directly coupled. Therefore, the actuation element’s inertia directly adds to the joint inertia [67].

Vertebrates have two parallel elastic mechanisms which are relevant for locomotion, namely parallel elastic components in each muscle and the elastic joint capsule (see Section 1.1.1). However, the influence of these elements is way smaller compared to the series elasticity of the tendons. The parallel muscle elements contribute only above the muscle rest length [28], and the nonlinear stiffness of the joint capsule is low within the joint work range of normal locomotion and only contributes towards maximum joint positions ([33], Fig. 4).

Parallel elastic actuation therefore allows robots to go beyond the bio-inspired regime, by making use of the parallel spring force throughout the whole range of motion of a joint. One major application is gravity compensation, where the parallel spring can support static loads without the necessity of additional energy input from the actuation element [68]. Another application are repetitive movements, where the spring fulfils most of the energy transition and the actuation element torque can be used mainly for loss compensation. This mechanism has been exploited in elastic spines of quadrupedal robots, which allow for energy transfer between front and hind legs [42, 69, 70]. Other applications are repetitive motions with robotic arms [71] and actuation of the bouncing motions of running monopods [34, 72, 73]. Chapter 5 of this dissertation presents a robot which makes use of the oscillating and gravity compensating properties of parallel elastic actuation to enable energy efficient monopod running.

### 1.1.5 Limb configurations and springy dynamics

Fig. 1.1 summarizes the six different robotic joint configurations which are investigated in this dissertation. A configuration thereby refers to a specific way actuation elements, springs and other dynamic elements are attached to a joint of a robotic limb. Configurations (a)-(c) do not contain a spring and are therefore called non-springy. Configuration (d) represents the passive springy case, configuration (e) shows the series elastic case (SEA), and configuration (f) shows the parallel elastic case (PEA), all introduced in Section 1.1.4.

As introduced in the previous sections, the dynamic behavior of a robot changes depending on the way springs are integrated into its system. In order to characterize this spring influence, we refer to a *springy dynamic* as a specific relation between spring force and joint position. In the case of the passive (Fig. 1.1d) and the parallel elastic configuration (Fig. 1.1f), each

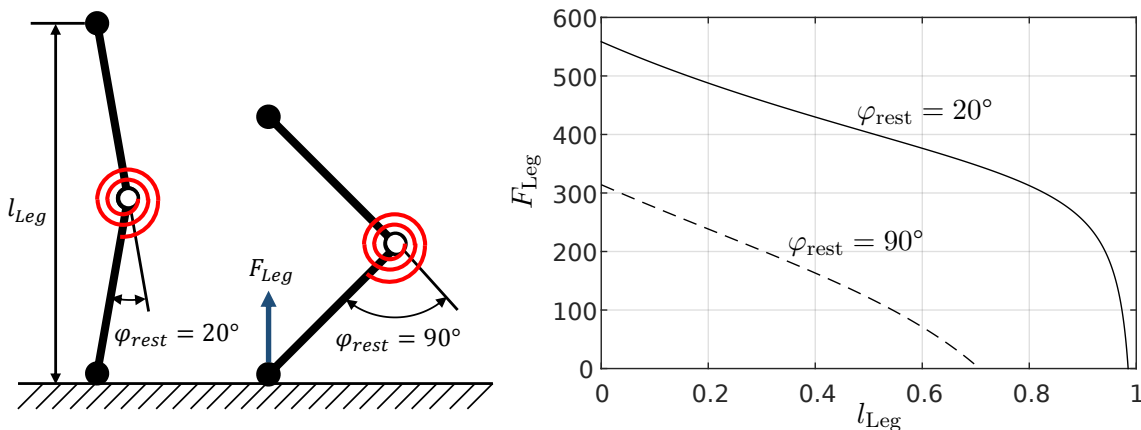


Figure 1.2: Different rest angles of the knee spring of a segmented leg lead to different springy dynamics. A rest angle of  $20^\circ$  leads to a nonlinear leg stiffness which decreases with decreasing leg length. A rest angle of  $90^\circ$ , on the other hand, leads to a nearly linear leg stiffness. A series elastic actuator can change the rest length of its spring by moving its actuation element, and therefore a SEA has multiple springy dynamics.

joint position leads to a defined spring force, i.e. once the attachment of the spring is set, both configurations exhibit only one springy dynamic. In the series elastic configuration (Fig. 1.1e) on the other hand, the actuation element length influences the spring force produced for a certain joint position, since it changes the rest length of the spring. In other words, when force is applied on a segmented leg equipped with a SEA, the overall spring stiffness of this leg depends not only on its segment lengths and its knee spring stiffness, but is significantly shaped by the actuation element position. An actuation element position leading to a rest angle of  $90^\circ$ , for example, results in a nearly linear behavior of the leg stiffness (Fig. 1.2). A rest angle of  $20^\circ$ , which corresponds to a nearly extended limb, results in high limb stiffness at the beginning, which then quickly drops when the leg shortens under load, therefore showing a non linear behavior. This example shows that a SEA can exhibit multiple springy dynamics, depending on the position of its actuation element.

An even larger variation in springy dynamics becomes possible with coupling-extended actuator, which is able to change its mechanical configuration depending on the state of its couplings. And finally, each stiffness of a variable stiffness mechanism is considered as one separate springy dynamic.

Analog to the springy dynamic, we define a *non-springy dynamic* as a distinctive mechanical configuration which does not include a spring. A completely passive joint as well as a mechanically locked joint or a joint directly driven by an actuator are examples for non-springy dynamics.

### 1.1.6 Controlling elastic elements

Elastic elements are not only able to conserve and transfer mechanical energy, they also influence the control of animals and robots. The simplest case is probably the springy joint without further actuation<sup>3</sup>. This introduces a rest position to the joint at which total elastic element torque is zero. Every deviation from this rest position causes a counter torque in the elastic element, pushing the joint backwards towards the rest position. The elastic element thereby acts as a simple P-controller with position dependent force feedback. When adding an actuation element in parallel, this mechanical feedback mechanism is strong enough to enable running with open

<sup>3</sup>In the case of an animal, this case occurs when the antagonistic muscles contract isometrically and allow only their elastic tendons for lengthening and shortening.



loop torque input without any sensory feedback, as presented in Chapter 4 of this dissertation.

Apart from acting as a controller themselves, springs can change the impedance of an actuator [61, 74]. In a series elastic actuator for example, the actuation element itself, which usually has a very high inertia due to its large gear reduction, is decoupled from the actuator output in terms of position due to the spring. The inertia which can be felt at the spring is nearly zero. This is especially beneficial for legged locomotion, since the low inertia of series elastic actuators can help reduce impact losses at touchdown. The low inertia can also release the requirements for the motor itself. Since for example locomotion on unstructured and unknown terrain with direct drive would require fast motors with high gain feedback to adapt to the unknown surface during each step, springs allow for much slower motor control.

Many springs show a distinct force-length relationship. Therefore, equipping a spring with a position sensor enables an easy and reliable way to measure the force on the spring, which makes series elastic actuators predestined for force control [62]. While the majority of the springs in legged robots shows a linear force-length relationship, recent research suggests that nonlinear springs may be beneficial for the robustness of running [75].

When multiple limbs touch the ground, closed kinematic chains are established, for example during double support phase in bipedal walking or more distinctive during quadrupedal standing. With rigid limbs with direct actuation, already small position errors can lead to large joint torques due to the limb motors acting “against each other” in the kinematic chain. Springy legs allow for compensation of these errors and therefore reduction of unwanted additional joint torques without any additional effort of the controller. Robots with direct actuation, on the other hand, need to establish a “virtual compliance” actively in their controller [76].

Beside these advantages, elastic elements also introduce large challenges to the controller. In the case of series elastic actuation for example, the spring dramatically lowers the bandwidth of the actuator [77]. If precise and fast force and position tracking is required, proper sensing and advanced control mechanisms are necessary.

### 1.1.7 Non steady-state locomotion

The majority of legged locomotion research deals with steady-state locomotion, for example walking or running with constant forward speed on level ground. However, the “daily life” of animals and mobile robots involves a large number of different maneuvers, from accelerating, breaking down, traveling over unstructured terrain up to falling down and, in the case of animals, hunting [15]. Given that, the question arises to what extent elastic elements may contribute to this large variety of non-steady motions.

A prominent example for research on non-steady locomotion is spring-mass running at variable forward speeds. McMahon [49] and Alexander [29] argued that the stiffness of the leg spring of a spring loaded inverted pendulum (SLIP) should increase with increasing forward speed. This assumption bases on relatively steep landing angles of the SLIP models, leading to shorter stance times at higher speeds. To implement this approach in legged robots, various concepts of actuators with variable stiffness have been developed so far [78]. In the animal kingdom, on the other hand, the stiffness of the passive elements (tendons) is nearly linear and cannot be changed significantly. Therefore, animals change their leg stiffness geometrically by varying the joint angles in their articulated limbs and decreasing their touchdown angle towards higher speeds [79].

Apart from this well documented mechanism, other applications of springs in dynamic maneuvers have been investigated selectively. For example, Roberts [80] found that tendons acting as series elastic elements can increase maximum muscle work production while Biewener [81] described a tradeoff between cyclic energy storage and explosive acceleration with respect to the tendon stiffness of kangaroo rats. Celik and Piazza [53] investigated the rapid accelerations during sprinting based on the spring loaded inverted pendulum.

Up to present day, most research still focuses on steady state locomotion. Therefore, to

contribute to the important field of non-steady locomotion, this dissertation presents a study where preloading of a spring can enhance the dynamic capabilities of a hopping robot (see Chapter 3.3.5).

### 1.1.8 Coupling mechanisms and preloading in nature and robotics

In this dissertation, a *coupling* refers to a mechanism which allows for locking the motion between two bodies of an agent with low or no energy expenditure necessary. If one of the bodies is an elastic element, couplings can enable the change of elastic properties of this agent, for example by adding new dynamics to the spring (see Section 1.1.5). *Preloading* on the other hand, which is one of many new dynamics enabled by couplings, describes the process of a muscle/actuator lengthening an elastic element in order to charge mechanical energy into this element. A coupling is used to lock the joint the elastic element is attached to, and later release of the coupling releases the strain energy.

In vertebrates, the muscle-tendon units are attached at fixed points on this skeleton and coupling mechanisms which would allow for reconfiguration of muscle-tendon attachment do not exist. However, some animals developed couplings based on singularities in lever mechanisms. Horses, for example, use their limb segments as such a lever mechanism. By locking the elbow during stance, they preload their biceps tendon, and this energy is released at liftoff due to buckling in the elbow joint, which acts as the singularity. The energy stored in the biceps tendon is then used for rapid limb protraction during flight phases [21]. Another example is demonstrated by several insects, which have developed a lever mechanism in their joints which allows them to lock this joint [22]. With the joint locked, the leg muscles preload their tendons and this energy is then released by the lever mechanism in order to achieve fast, catapult-like limb motions.

In legged robots, coupling and locking devices are widely used to lock springs and joints or to reconfigure robots [82]. In addition to lever mechanisms with singularities, robots can make use of geometric or friction clutches, which are able to connect or disconnect multiple rigid bodies. This leads to an even larger number of applications, where preloading is only one of many. Chapter 2 of this dissertation introduces such an actuator based on couplings, which is able to switch between different actuation modes depending on the task.

Depending on the configuration of actuation and elastic element and the control scheme applied, preloading can be used for four different purposes: Power/speed amplification, controlled energy input, decoupling the actuator, and power/speed reduction.

**Power/speed amplification** In contrast to an actuation element, whose speed is limited, preloaded elastic elements can release their energy instantly, and therefore preloading is often used when high speed and peak powers are required. In the animal kingdom, horses preload their biceps during stance, which allows for fast limb protraction after liftoff [21]. In order to enable preloading and release of energy in the biceps tendon, the horse makes use of the forward movement of its trunk. Together with the changing orientation of the ground reaction force during stance, this forward motion stretches the biceps muscle-tendon unit while the carpus is locked in extension. In late stance, the carpus buckles and releases the energy stored in the biceps muscle-tendon unit. Another very familiar example is finger snapping of humans, where the *musculus flexor digitorum profundus* preloads the tendon of the middle finger. The middle finger itself is held against the thumb and a sideways motion of the middle finger releases the energy of the tendon. Further examples of preloading occur in some insects, which use a preloading mechanism for rapid acceleration in jumping [22]. In this case, a lever mechanism in their leg joint locks this joint during preloading and releases the energy for a single jump [22]. This mechanism has been successfully applied to multiple small scale jumping robots, which make use of an eccentric cam mechanism [43–45] or a ratchet mechanism [83] to preload their springs.

**Controlled energy input** In robotics, preloading proposes a simple way to insert a defined amount of energy into the system. This is exploited for example by passive dynamic walkers, where the ankle joint is preloaded with a defined amount of energy during flight and this energy is then used for ankle push during the next stance phase [84]. In hopping robots, the same principle allows for an easy and reliable control of the steady state hopping height, as demonstrated in Chapter 3 of this dissertation.

**Decoupling of the actuator** While the elastic element is releasing the energy, the actuation element does not need to move at all. Therefore, it becomes possible to decouple the actuation element after preloading, for example by making use of an additional coupling mechanism. This allows for example to use an actuation element with limited peak force for hopping, since it can be decoupled after preloading during flight, and therefore does not have to bear the whole ground reaction force during stance. Such a mechanism is described in Chapter 3 of this dissertation.

**Power/speed reduction** Unlike muscles, which become weaker when contracting faster, speed and force are much less coupled in electric motors. In fact, when neglecting the motor inertia, the output torque of an electric motor is entirely defined by its current, while the motor voltage mainly determines the speed. Out of the motor equations, it can be seen that in terms of energy efficiency it is beneficial to preload the spring as fast as possible. For most legged robots, the ideal motor speed would be much too high when applied directly during the stance phase. Instead, the spring can be preloaded during flight phase with this speed, and the energy is then released much slower during the subsequent stance phase.

## 1.2 Problem statement

Elastic elements introduce strong passive dynamics to a legged system. The exploitation of these dynamics can improve robustness, energy efficiency, power output and control of animals as well as legged robots. In the animal kingdom, elastic elements are therefore used in manifold ways and optimized to achieve maximum overall performance. Unfortunately, due to the large differences between muscles and actuators in terms of inertia and scalability, the musculoskeletal body plan of animals cannot be adapted 1:1 to robotic systems. In legged robots, many applications of elastic elements, their interconnection with the actuators and their influence to the robots performance are not completely explored and only a small portion of them is properly investigated. Even though various applications of springs have been demonstrated in specialized platforms, more complex designs like humanoids [85] often make no use of mechanical springs at all.

One underlying reason for this disproportion between theoretical advantages and practical use might be the limitations these same passive dynamics introduce to the system. Being beneficial for the motions they were tuned for (for example forward walking or running at a certain speed), the same passive dynamics become obstructive when fulfilling other motions, like manipulation or climbing for example. Nature might solve this problem with a large number of independent motor units, but today's actuators do not allow the same for robots. Being equipped with a low number of large actuators, even walking or running over unstructured terrain can lead to a point where passive dynamics optimized for level ground locomotion do more harm than benefit to a legged robot. From this perspective, it seems understandable that more versatile robots do not carry additional parts (springs and their implementation) with them whose overall benefits in specific motions are consumed by their drawbacks in all other motions.

## 1.3 Hypothesis

Despite elastic elements having a hard time in today’s versatile robots (by simply not being included), animals show that systems based on elastic elements can be efficient, powerful and extremely versatile at the same time. Therefore, since a 1:1 copy of the musculoskeletal system is not possible with today’s actuation technology, we state that a deeper understanding of *all* possible interactions between springs, actuators and their joints, i.e. all possible springy dynamics, is a necessary first step to make springs successful in legged robots. Since past investigations mainly focused on the role of springs in supporting the bouncing motion in running [41, 48, 86] using series elastic actuation [61], and easing the control of legged robots [62], this thesis contributes by investigating two alternative ways of spring exploitation, namely (1) preloading for increased power output and reduced actuator load, and (2) parallel elasticity for robust and energy efficient monopod running with large payload.

## 1.4 Contribution

This dissertation investigates alternative springy dynamics in legged mobile robots. Two main contributions have been identified throughout the presented research. First, the number of different dynamics and the output performance of conventional series elastic actuators has been increased by making use of discrete couplings and preloading of the actuator spring. Second, mechanical feedback and body weight support through parallel elastic actuation has been investigated in two monopod runners. Both topics contribute towards the goal of a deeper understanding of springy dynamics in mobile legged robots. The two contributions of this dissertation are organized in four chapters. The first two chapters describe the preloading dynamic, while the last two chapters investigate the parallel elastic dynamic.

**1. Coupling-based series elastic actuation through linear multimodal design** Conventional series elastic actuators feature a fixed spring stiffness and therefore exhibit only a limited number of springy dynamics. By equipping such a series elastic actuator with mechanical couplings, the configuration of the spring can be changed and additional dynamics become possible. This dissertation presents an investigation of a coupling-extended series elastic actuator (CE-SEA) suitable for actuation in legged robots, whose three couplings allow for nine different configurations.

**2. Improving hopping height control of legged robots by using coupling-based series elastic actuation** In addition to the isolated investigation of the CE-SEA, this paper investigates two of its possible dynamics in a one legged hopping robot setup. First, the couplings allow for decoupling the actuation element of the series elastic actuator during part of the stance phase, therefore allowing for higher actuator loads and therefore higher hopping height. And second, the couplings allow for preloading of the spring during flight, and releasing this energy during the subsequent stance phase. Since the actuation element is decoupled during stance, again higher actuator loads and therefore higher hopping heights become possible.

**3. Parallel elasticity for robust and versatile monopod running** Biological systems and most legged robots exploit their springs in a series elastic configuration. In order to go beyond the bio-inspired regime, this dissertation exploits parallel elastic actuation as an alternative springy dynamic. It is shown that parallel elastic actuation allows for robust mechanical feedback at a large variation of forward speeds, which is exploited in a monopod runner.

**4. Improved energy efficiency through body mass support in parallel elastic monopod running** In a parallel elastic setup, the spring can support the body weight of a robot and

the motor can be used for loss compensation only. In this dissertation, we show that monopod running with parallel elastic actuation can heavily profit from this weight support. In fact, it turned out that this approach showed better energy efficiency than any other legged robot.

## 1.5 Structure of the dissertation

Following this introductory chapter, the contributions of this dissertation are presented in four chapters. Each chapter closely follows one or more publications. These chapters have been written to be self-contained, i.e. they can be read independently. This means on the other hand, that there is some overlap between these chapters.

Chapter 2 presents an approach to increase performance and variability of dynamics of a series elastic actuator by equipping it with discrete couplings. This so called coupling-extended series elastic actuator (CE-SEA) is then analyzed in simulation and physical experiments once in stand alone operation and then in Chapter 3 in a robotic leg with respect to maximum hopping height and controllability of hopping height. Both chapters present couplings as a reasonable candidate for increasing the variability of spring-induced dynamics in legged robots. Chapter 4 introduces a minimalistic monopod runner concept based on parallel elastic actuation. It is shown in simulation and physical experiments that this design enables stable hopping with open-loop control over a large variation of parameters. Chapter 5 investigates the use of parallel elastic actuation for energy efficient monopod running. It is shown that this robot is able to outperform existing robots and animals in terms of energy efficiency while providing a large parameter region of self-stable forward running. Chapter 6 concludes this dissertation and identifies directions for future research.

## Chapter 2

# Coupling-based series elastic actuation through linear multimodal design<sup>1</sup>

A spring attached in a specific way to a joint of a robotic limb adds *springy dynamics* to this joint, for example with the spring producing counter torques when the joint is deflected from its rest position. These springy dynamics thereby change when the spring is attached differently to the same joint. In today's legged robots, springs are used mostly in series with an actuation element, forming a series elastic actuator (SEA). When such a SEA is attached to a joint of a robotic limb, its actuation element is able to change the rest position of the springy joint by changing its own deflection. This allows an SEA to achieve multiple springy dynamics, as illustrated in Section 1.1.5.

Despite having multiple springy dynamics, the range of these dynamics in a SEA is limited. While being able to span from walking to highly dynamic applications like running or hopping, there are applications where no adequate springy dynamic is available and therefore the spring can become obstructive. One example occurs with a SEA used for hip actuation. As long as the stride frequency matches the natural frequency of the spring mass system containing limb and SEA spring, the SEA shows good performance with minimum actuator input necessary. However, the further the stride frequency is away from this natural frequency, the more the actuator needs to deflect with (low frequencies) or against (higher frequencies) the spring to achieve the desired limb movement. This results in increased energy consumption and often poor energy efficiency. Another limitation of SEA's occur during precise manipulation with high forces. When pushing an object with a SEA, the actuator first needs to compress its spring to create the necessary force, which uses energy and slows down the possible manipulation speed. In addition, the stored energy in the spring can release unintentionally and cause the object to move uncontrolled. In such situations, a nearly rigid spring (i.e. direct drive of the actuator) would perform better.

Both examples, the motion outside the resonance frequency and the precise manipulation can

---

<sup>1</sup>This chapter presents a collaborative work with my colleagues D. Leach and N. Maheshwari under the guidance of my supervisor F. Iida. I have designed the LMMA platform, conducted the physical experiments with the ETHOP and contributed to the writing of the manuscript. My colleague D. Leach has written the main storyline, performed the simulation experiments and contributed to the physical experiments and discussions with my colleague N. Maheshwari any my supervisor F. Iida. This chapter has been adapted and edited from the following publications:

- D. Leach, F. Günther, N. Maheshwari, and F. Iida. Linear multimodal actuation through discrete coupling. *IEEE/ASME Transactions on Mechatronics*, 19(3):827–839, 2014
- F. Günther and F. Iida. Preloaded hopping with linear multi-modal actuation. In *Proc. 2013 IEEE/RSJ Int. Conf. Intelligent Robots and Systems (IROS)*, pages 5847–5852, Tokyo, Japan, 2013

be addressed by changing the stiffness of the SEA spring. Therefore, variable stiffness actuators have been investigated extensively in the past [78], and certain models are able to change the spring stiffness from very low values to nearly rigid behavior. While the stiffness of a SEA means changing its dynamics, from another point of view, one can call this *adding new dynamics* to the SEA spring. Most variable stiffness mechanisms contain of one or multiple springs with a fixed stiffness, plus a lever mechanism to vary the resulting geometrical stiffness. Therefore, this lever mechanism is adding new dynamics to the spring(s) which would not be there without the mechanism.

In this dissertation, we investigate a more general approach of adding new dynamics to a SEA spring. By extending a SEA with discrete couplings, our *coupling-extended series elastic actuator* (CE-SEA) can connect its spring in multiple ways within the actuator to achieve a large variety of different dynamics. Namely, direct drive (infinite stiffness, large inertia), passive behavior (zero stiffness and zero impedance), series elastic behavior (normal stiffness at low inertia) and some additional dynamics like preloading become possible. This range goes way beyond the dynamic range of conventional SEA and even variable stiffness actuators and allows for a number of additional actuation strategies.

Changing the attachment of a spring to a joint requires a coupling, i.e. a mechanism which is able to actively connect and disconnect multiple bodies. These couplings can be realized using two different concepts, namely form fit or friction fit. A coupling based on form fit locks geometrically using bolt or lever mechanisms, for example a ratchet and a pawl. The parts are often designed in a way that no static friction is necessary to establish the contact. When making use of geometric singularities, these couplings require no energy once closed and allow for handling large forces on small space and weight. But, as a consequence of their design, these couplings feature only a finite number of closing positions and cannot dissipate significant amounts of energy while closing. This adds additional constraints to their control since the relative speed between the two bodies at the time the coupling closes is limited.

A more robust approach can be found in friction clutches, which make use of dynamic and static friction of two parts pressed against each other. These couplings are widely used in engineering, for example in most braking mechanisms in vehicles. Due to their ability to dissipate large amounts of energy, the coupling can be engaged independent from the relative speed of the bodies to be coupled, which leaves the controller more freedom. In addition, friction clutches allow for establishing connection at arbitrary positions, and when equipped with a self locking mechanism, they are able to hold connection without energy input too.

Due to this increased robustness, we decided to use friction clutches as the coupling element in the first generation of our CE-SEA. For simplicity, the clutches are actuated by a normal servo motor and a worm gear allows for holding the clutch force without additional energy input. After extensive tests with different material combinations, we found the combination of rubber clutch pads on steel rails to offer a good compromise between high friction coefficient, low abrasion and sufficient robustness against geometrical tolerances.

Although our CE-SEA was designed to actuate articulated legs, we decided to use a linear instead of a rotational setup. On the one hand, linear coil springs show better energy to weight ratio and easier implementation when compared to torsional springs, and on the other hand we found a modular design with independent clutches easier to realize in a linear setup. In order to have full flexibility when integrating the CE-SEA into robotic legs, we integrated actuation element, spring and clutch mechanisms in one unit, which can be mounted on two connection points (front and back) to any robotic structure, similar to conventional SEA's. Apart from the two connection points, our CE-SEA therefore has no additional requirements to the structure it drives.

The first part of this chapter introduces a mechanical prototype of our first generation CE-SEA, which is called *linear multi modal actuator (LMMA)*. After introducing the design idea of adding springy dynamics through coupling based linear multi modal actuation, we present

a simulation model of the LMMA and use it to analyze impedance and performance of elastic energy storage of the actuator. In a next step, we then validate the simulation model with physical experiments using our physical prototype. We first investigate the LMMA in a stand-alone test, i.e. the LMMA hops on its own without being attached to a robotic leg.

These first series of tests, including the stand-alone series elastic hopping, made use of the LMMA clutches in a static way, by changing the actuator’s mode only during standstill. To investigate the limitations of the friction clutches, we then run a second series of tests where the actuator changes its mode during operation. This enables the *preloading* dynamics to achieve energy input during the flight phase of steady state hopping by preloading the spring, and then release this energy during the subsequent stance phase. After investigating the preloaded hopping of the LMMA again in stand-alone operation, we then present a case study of robust preloaded hopping with the same LMMA attached to the knee joint of a robotic leg. During these physical experiments, we demonstrate how the energy input of the actuator changes from stance phase (conventional SEA hopping) to flight phase (preloaded hopping), and show the limitations of the friction clutches in preloaded hopping to be caused by increasing losses due to timing issues during touchdown.

## 2.1 Introduction

Biological muscles exhibit a diverse array of functions and behaviors when compared with robot actuators. Muscles provide full actuation of joints to produce large torques but can very quickly relax to allow completely passive movement with very low damping. When interacting with the environment, the viscoelastic properties of a joint can be flexibly regulated to adapt to many tasks, with the elastic properties of muscles and tendons used to store and recycle kinetic energy for efficient motion control [17] and disturbance rejection [87]. Many muscles can connect to the same skeletal joint providing redundancy and robustness against malfunction. Furthermore, these numerous connections allow for a variety of muscle configurations such as mono- and bi-articular connections while allowing other muscles to act in parallel. For example, the brachialis connects the upper and lower arm and the triceps connect the lower arm with the shoulder. Such a large variety of operations and functions in biological muscles are the foundation of an animal’s versatility in motor control when dealing with uncertain task environments.

A number of robotics researchers have previously explored how to engineer such muscle-like functions in robotic systems. One of the long standing investigations in this vain has been impedance and admittance control [88, 89]. The underlying idea of this line of research is to develop theoretical models of biological motor control and implement them into mechatronic devices. The implementation of these models has successfully demonstrated behaviors of biological motor control such as force/torque patterns in the sensory-motor loop. This technology has greatly contributed to medical and therapeutic robotic applications. A challenge of this approach, however, is the requirement of high bandwidth in the control architecture which makes it difficult to scale up the complexity for versatile robotic applications [90].

A more practical approach for mobile robot applications is the series elastic actuator (SEA) [61] in which mechanical springs are attached to an actuator in series to mimic the viscoelastic properties of biological muscles [29]. A number of advantages have been reported for this approach, these include storing kinetic energy in the mechanical springs for energy efficient motor control [38, 91, 92] as well as filtering instantaneous impacts even with relatively low control bandwidth. The dynamic range of SEA operation is thereby generally limited by the stiffness of the elastic element [61, 90]. The concept has also been extended to many other configurations of mechanical springs which have been investigated to see how they can contribute to different dynamic motion control of robotic systems [93–95].

More recently a research trend has shifted to a set of technologies that enable robotic systems to actively vary stiffness [96–101]. These variable stiffness actuators aim to have the benefit of



both compliance when it is required but also the ability to adjust the stiffness of the system to increase the bandwidth of the actuator or to match the resonant frequency to the task [102,103]. There is sound biological motivation for variable stiffness in actuators. For instance, animals and humans control the stiffness of their legs to adapt to the speed at which they are running [49]. It has also been shown that variable stiffness can be exploited in underactuated systems to improve the performance for explosive movement task [104].

There are many approaches to controlling the stiffness of a joint. One example is to use an agonist-antagonist set up with nonlinear springs, specifically stiffening, so that by increasing the tension of both springs the stiffness at the joint can be increased. An example of such an actuation method is the actuator with nonlinear elastic system which adjusts the effective length of a torsional spring and thereby adjusts the stiffness, and then places two such actuators antagonistically around a joint to produce variable stiffness [105]. Other methods include controlling the pretension of a single spring [101] or controlling the lever arm connecting the springs and a rotary joint [98].

Stiffness is not the only means to broaden the output impedance of an actuator. Indeed controlling the damping component has proven more beneficial for some applications, particularly in the fields of prosthetics [106], orthotics [107–109], and rehabilitation robotics [110] where energy efficiency is less of a consideration and safe human interaction is of prime concern. Damping is controlled by the inclusion of brakes and clutches and the development of such mechanisms is proving to be a fertile field of research [111–114]. Differentials have also been used to combine two inputs such as two motors [115] or a motor and brake [116].

The focus in this chapter is on a different method of implementing clutches with which we could mimic some aspects of biological muscles that have not been sufficiently explored in the past. This approach utilizes discrete coupling mechanisms like clutches in robotic systems with the aim to substantially increase the variations possible actuator dynamics. Discrete couplings have rarely been considered in robotic systems that are articulated with limbs and joints with some exceptions [117–119]. One important reason for this is that such extra mechanisms add an overhead in weight and size which reduces the absolute performance of an actuator. However, with well-designed miniaturized mechanisms, the potential benefits in diversity can outweigh some of the performance losses.

If compared to the previous approaches mentioned, the innovation explained in this chapter lies in the use of multiple mechanical couplings in the operation of one kinematic joint in articulated mechatronic systems such as robotic manipulators and legged robots. As made clearer in the next section, by employing multiple mechanical couplings, we are able to achieve a number of favorable motor functions that are necessary in many dynamic robotic systems for their flexibility and behavioral diversity. For systematic modeling and analysis of the proposed approach, this chapter explains both the basic concept and the detailed design of our first physical actuator prototype.

The rest of this chapter is structured as follows. In Section 2.2, we introduce an overall concept of joint operation with dynamic couplings. In Section 2.3, we present a case study of a “linear multimodal actuator” (LMMA) in which we explain the design and control of our platform in detail. Using this platform, we go on to model the system in Section 2.4 and analyze it in stand-alone operation in Section 2.5. Section 2.6 shows the integration of the LMMA into a robotic leg, and Section 2.7 discusses possible control strategies for monopod hopping using coupling-extended actuation. Section 2.8 then shows physical results for clutch-extended and normal series elastic hopping. In Section 2.9, we discuss further challenges and perspectives to conclude this chapter.

## 2.2 Multimodal actuation

In this section, we discuss how we can take advantage of multiple discrete couplings in robotic systems, a general concept which approach which we call multimodal actuation.

### 2.2.1 Basic concept of multimodal actuation

Here we consider a robotic system that is articulated by limbs and joints (e.g., knee, hip, and elbow joints of legged robots or robotic manipulators), in which the joints are connected to the actuators via discrete couplings. In such a case there are two distinct ways couplings can be used: in series with the dynamic element (i.e. the actuation element) or in parallel, as illustrated in Fig. 2.1a and 2.1b. When the coupling acts in series it is operating as a clutch that switches between the output being connected to the motor or disengaged and completely passive. In contrast, the dynamic coupling acting in parallel indicates connects the output to the motor housing or “ground”, here the engaged coupling would cause the output to be rigid. Although the dynamic couplings have been described in relation to motors, the motors can be replaced by any dynamic element such as a spring or a damper.

The operation of brakes and clutches can be most intuitively illustrated by their use in motor vehicles. Just as with robot actuators, internal combustion engines have a limited range of performance in terms of output speed and torque. Brakes and clutches are then used to extend this performance range. The brakes act to stop the wheels rotating relative to the rest of the vehicle, they can provide much greater force and control and can operate at speeds that would cause the engine to stall. The clutch in a manual transmission acts to connect and disconnect the wheels to the motor output, or more specifically the motor and the gearbox. Without the clutch engaged the wheels spin freely in relation to the rest of the vehicle. Through the use of a clutch and gearbox the same motor can then have different speed and torque ranges at the output.

Using the two basic blocks of couplings acting in series or parallel many different configurations can be constructed, one of the most general formulations is represented in Fig. 2.1c. This configuration has a dynamic element, such as a motor, paired with a coupling at the center as the foundation. This central block can then be bypassed by any number of couplings acting in parallel. The motor and clutch allow the output to be actuated or passive. With a chain of dynamic elements connected in series, a coupling can bypass the dynamic elements it is acting in parallel with and connect the dynamic elements acting in series with it directly to the output. Ultimately, engaging the final coupling  $c_n$  would make the output rigid.

### 2.2.2 Linear eight-mode actuation

There are many possible configurations using this basic concept. One possible configuration that could be useful for legged robot locomotion would be a series elastic actuator (SEA) with three couplings. These three couplings can control the two dynamic elements of an SEA, namely the motor and the spring. This configuration can be seen in Fig. 2.1d.

In this implementation, the three couplings can switch between two discrete states, engaged or disengaged, consequently eight modes of operation are possible. These eight modes are outlined in Table 2.1. As a shorthand notation, the configurations are numbered from the binary number produced when reading the couplings as engaged or disengaged with 1 indicating the coupling is engaged and 0 that it is disengaged.

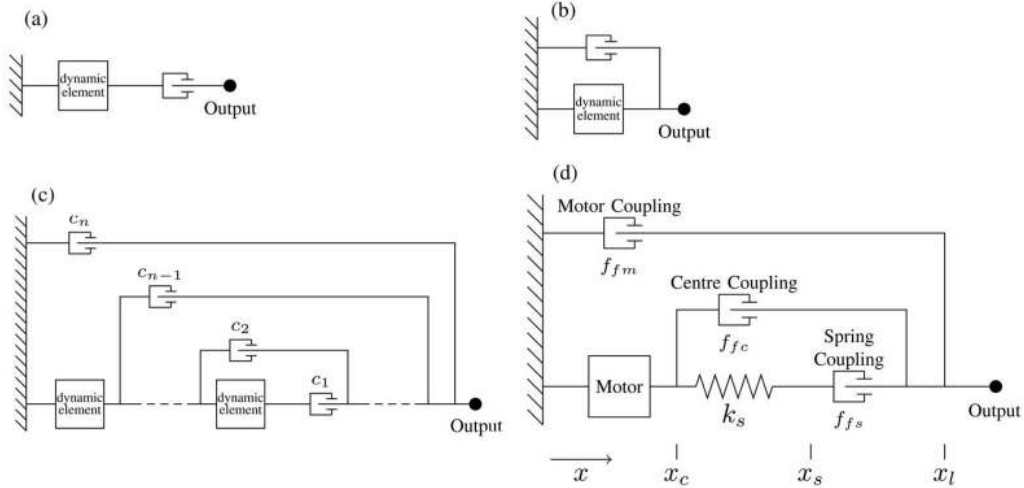


Figure 2.1: Block diagram representations of (a) a coupling acting in series, and (b) a coupling acting in parallel. (c) The generalized linear case for multimodal actuation with  $n$  couplings labeled with  $c$ . (d) The implementation to a series elastic actuator, the configuration implemented in the physical prototype of the linear multimodal actuator (LMMA). The lengths  $x_c$ ,  $x_s$ , and  $x_l$  are illustrated in Fig. 2.3

Table 2.1: Eight Modes of the LMMA

Configuration	Coupling			Mode
	Spring	Centre	Motor	
0	0	0	0	Passive
1	0	0	1	Rigid
2	0	1	0	Position
3	0	1	1	Transition
4	1	0	0	SEA
5	1	0	1	Preloading
6	1	1	0	Storing
7	1	1	1	Transition

Configurations of the couplings, in the middle three columns 0 indicates the coupling is disengaged and 1 that is engaged.

Important to note here is that the motor output can either connect directly to the output when the spring is bypassed, or otherwise it controls the input position of the spring. This makes it possible for the motor to compress the spring and store energy. The eight different modes are now described in more detail.

1. *Mode 0*: The actuator is passive and completely free to move.
2. *Mode 1*: The actuator is rigid and will only move if the force applied to the couplings overcomes the force of the coupling mechanism.
3. *Mode 2*: The actuator output is directly controlled by the motor.
4. *Mode 3*: This configuration allows a charged spring to be discharged while the actuator output is rigid. It also serves as a transition configuration between modes 1 and 2.
5. *Mode 4*: The actuator becomes a SEA.

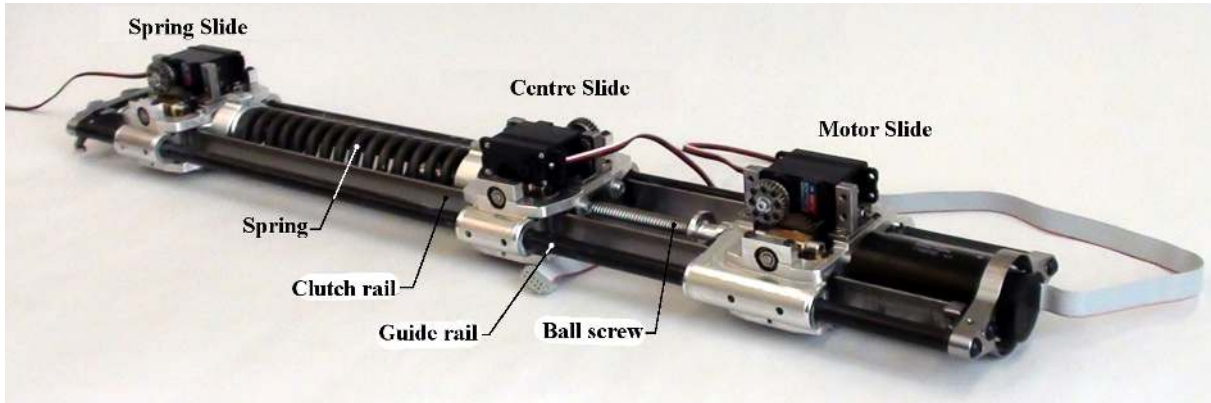


Figure 2.2: Physical prototype of the linear multimodal actuator with the main components annotated, the two flat clutch rails run in between and parallel to the guide rails. Specifications are listed in Tab. 2.2.

6. *Mode 5*: The actuator is rigid but the spring can be preloaded by the motor.
7. *Mode 6*: This mode allows energy to be stored in the preloaded spring while also providing stiff position control (mode 2). The spring is preloaded during mode 5 and then mode 7 is used to transition from modes 5 to 6.
8. *Mode 7*: Provides a safe transition from mode 5, the spring being preloaded, to mode 6, stiff position control once the spring is preloaded.

The eight modes outlined above are very much dependent on the order of the spring and motor. With the order reversed it would not be possible to bypass the spring to have a stiff position controlled mode and so mode 2 would instead become a passive spring mode without actuation. It would also not be possible to store energy in the spring while having position control of the output (mode 6), instead the output would have to remain rigid.

Although there are eight different modes, there are only four distinct outputs produced by the actuator. These are the passive, rigid, series elastic, and stiff position controlled modes. The remaining four modes, however, are not redundant but provide important additional features such as charging the spring and safe transitions between modes.

### 2.2.3 Characteristics of multimodal actuation

A robotic system can benefit from this actuation strategy in many ways. The system is capable of operating a joint with different mechanical characteristics by configuring the couplings. Unlike conventional systems, a legged robot, for example, would be able to passively swing joints for energy-efficient walking by disengaging all couplings; it could also switch some of the joints to the series elastic mode for fast running by storing energy in the spring; and a precise control of legs is possible while carrying large payloads when switched to the stiff position actuated mode.

The discrete mechanical couplings also enable rapid switches between different modes. The switching between series-elastic and the stiff position modes, for example, is controlled through a single discrete coupling.

Another important feature of the multimodal actuation lies in the redundancy of motor control. Since each dynamic element is independent with respect to output of the actuator, malfunction of elements can be isolated from the joint operation through the discrete couplings. This property could help enhancing the adaptability of robotic systems as well as increasing safety of operation in human-oriented environments.

Finally, the proposed concept is intrinsically modular and allows us to flexibly design or re-configure robotic systems. With this actuation strategy, we are able to design a legged robot with

Table 2.2: Specifications of the actuator

Description	Value
Overall length	669 mm
Width	114 mm
Height	76 mm
Ball screw lead	2 mm
Ball screw diameter	12 mm
Ball screw range	145 mm
Knee lever	70 mm
Knee angle	0-120°
Mass of actuator	4.5 kg
Mass of Centre slide	0.503 kg
Nominal torque of motor	0.187 N m @ 7000rpm

a large actuation at hip joints, e.g., enhanced damping performance in knee joints and more passive elasticity in ankle joints. The flexibility is particularly helpful for designing and constructing bioinspired robotic systems (e.g., legged and manipulator robots that employ passivity-based underactuated motion control) that usually require large variations of actuator performance.

There are, however, a few drawbacks in the proposed approach. The most significant challenge lies in the fact that weight and physical dimension of each joint can be very large because discrete mechanical couplings are usually heavy and large. Furthermore, the proposed approach increases mechanical complexity. From this perspective, in the next section we explain how these challenges can be dealt with through a case study of a physical prototype we developed in our laboratory.

## 2.3 Design of the linear multimodal actuator

To test the proposed concept, we developed a physical platform of an eight-mode actuator in a linear configuration, which we call the “linear multimode actuator” (LMMA). This section first explains the design overview of the LMMA and the detailed mechanism of discrete mechanical couplings. Then, we explain the control architecture developed for the LMMA.

### 2.3.1 LMMA design overview

The main components of the LMMA are a linear actuator, slides housing the couplings, a spring, two guide rails, and two clutch rails, these are shown in Fig. 2.2. The main body of the LMMA consists of a linear actuator (a rotational DC motor connected to a ball screw) and a mechanical spring placed in series through one of the slides housing a discrete coupling. This series-elastic component also has two additional slides with couplings at both ends. The three connected slides are then mounted onto a pair of guide rails. Running parallel to the guide rails are a pair of clutch rails that pass through each slide. The couplings housed within each slide coupling with the clutch rails and so prevent the slide from moving along the guide rails. Therefore, when all three couplings are disengaged, the linear actuator and the spring can freely slide along the rails. Linear bearings are used between the guide rails and the slides so as to reduce friction losses.

The slides are designed to be modular so that different components can be mounted into them, for instance, in the LMMA prototype the spring can be interchanged to provide different stiffnesses. The spring could be replaced with a damper or motor instead. The modularity helps

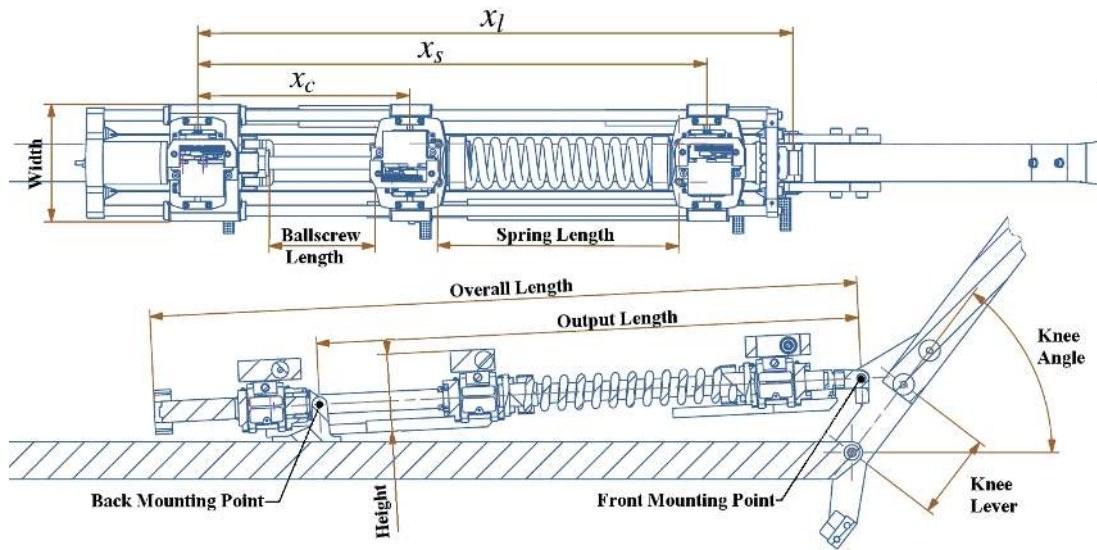


Figure 2.3: Top and side view of the LMMA mounted in the rotary joint of a two segment leg. The specifications of the actuator are listed in Tab. 2.2.

to reduce the mechanical complexity and manufacturing cost while increasing the flexibility and reconfigurability of the LMMA.

The three couplings are named motor, center, and spring slides as they characterize their functions, respectively. The left most block in Fig. 2.2, the spring slide, is connected to the spring on the one end, and nothing is connected on the other side. On the right-hand side in Fig. 2.2 is the motor slide which bridges the rotational dc motor on one end and a ball screw on the other. In between the spring and motor slides is the center slide housing the nut of the ball screw on one end and attached to the spring on the other end. In the platform shown, we used a Maxon RE 40 DC motor with Maxon MR Type L 256 CPT 3 channel Encoder with a resolution of 5012 counts per turn, and a steel spring with a stiffness of 10 N/mm. A DC motor was sufficient to power the actuator as the limiting force came from the coupling mechanism.

The LMMA can be mounted to actuate the rotary joint such as the knee of a robot system, this is shown in Fig. 2.3. The two mounting points of the LMMA are annotated, the motor slide acts as the rear mounting and the end of the guide rails as the front mounting point. The distance between these two points is then the output length of the actuator. The design of our LMMA prototype allows the knee joint to be operated between 0 and 120°. Further specifications of the LMMA are given in Tab. 2.2.

With this design, all eight modes described in Section 2.2.2 can be used in this joint. The action of four of these modes is illustrated in Fig. 2.4. The passive mode 0 is shown in Fig. 2.4a, here the knee angle and LMMA length move without resistance and the length of the spring and ball screw are unchanged. Fig. 2.4b shows the stiff position control mode 2 with only the center slide coupling engaged. Here the length of the ball screw changes to control the angle of the knee joint. By only engaging the spring slide coupling on the left in Fig. 2.4c, the actuator become series elastic so that the spring can deflect with changes in the knee angle. The ball screw can also regulate the deflection of the spring to provide force control. Finally, Fig. 2.4d shows mode 5 where the two outer couplings are engaged. This rigidly fixes the angle of the joint but allows the ball screw to compress the spring and store energy for short bursts of high output power.

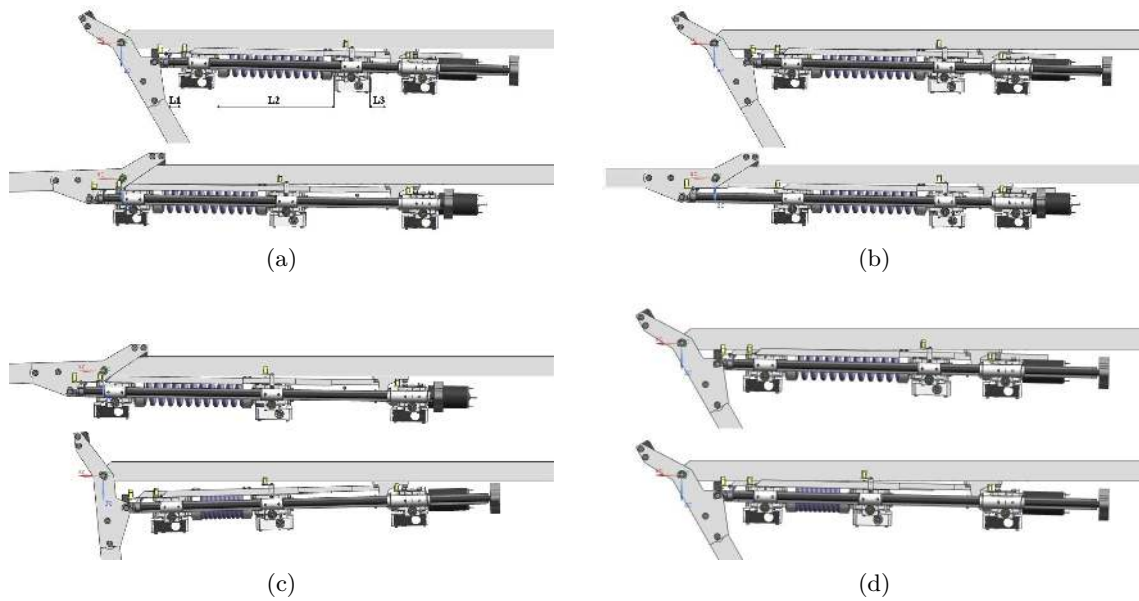


Figure 2.4: Depiction of different modes of actuation of the LMMA in the rotary joint of a two segment leg. (a) Mode 0: passive. (b) Mode 2: stiff position control. (c) Mode 4: series elastic (SEA). (d) Mode 5: preload spring.

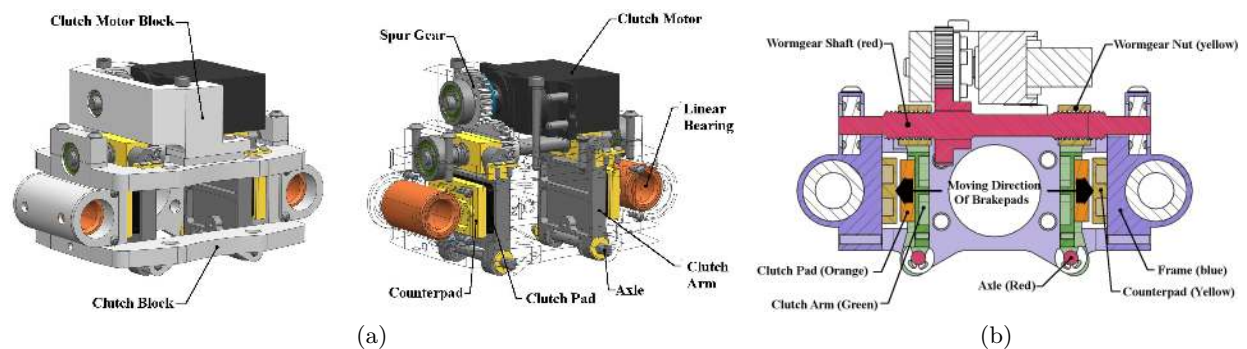


Figure 2.5: (a) CAD assembly showing different components of the coupling mechanism with and without the housing to illustrate the braking mechanism. (b) Cross section of the coupling mechanism.

### 2.3.2 Design of the coupling mechanism

The most significant challenge in the design of the LMMA was to develop a coupling mechanism that is able to generate a large dynamic range of braking forces while maintaining rapid transitions and the physical dimensions compact enough to be mounted in a robotic system. Our prototype of the coupling mechanism employed dry friction as this lent itself to miniaturization and can be controlled relatively easily. Rubber was found to be the best material for the clutch pads, we used shoe sole rubber with a Shore Type A durometer hardness of 70. The low shear strength of the rubber required an increase in the contact area, for this reason dedicated flat clutch rails were included which can be engaged from both sides.

The main components of the coupling mechanism housed in each slide are annotated in Fig. 2.5a. The coupling mechanism is illustrated in Fig. 2.5b and operates as follows. The clutch motor rotates the worm gear shaft (in red) via the spur gear, this pushes the worm gear nuts (in yellow) apart. The worm gear nuts are connected to the top of the clutch arms (in green) which pivot around their axles (in red). As the worm gear nuts move outward the clutch

arms push the clutch pads (in orange) against their counter pads (in yellow). A clutch rail runs between each clutch pad and counter pad, in this way the rail is engaged from both sides. The worm gear shaft can move freely along its axis of rotation, this ensures that the braking force is evenly distributed between the both clutch rails.

A Kondo KRS 2350 HV 12 V servomotor is used for each coupling, the motor is able to produce 3.3 N m of torque. The braking mechanism was designed such that an angular rotation of 60° of the motor shaft resulted in a displacement of 1 mm of the clutch pads. This particular servomotor had the feature that it could be switched ON and OFF when given the correct PWM signal. This, in conjunction with the non back-drivable worm gear mechanism of the coupling, meant that once a coupling had engaged or disengaged, no more energy needed to be consumed to maintain a given configuration.

## 2.4 Modelling and analysis of the LMMA

The LMMA can be characterized by its capability of generating several distinct mechanical dynamics ranging from completely passive and series elastic to high-gain actuation and rigid mechanics. For a systematic analysis and performance test, this section describes a model that represents the main characteristics of the actuator. Based on the model, we analyze two important performance metrics, impedance, and the energy storage capacity of the LMMA.

### 2.4.1 Modelling the LMMA

In the modeling process of the LMMA, braking forces in the couplings play a central role. Each coupling provides a variable force in phase with the velocity of the slide relative to the rails. In the physical prototype, the clutches produce dry friction, the Coulomb friction model can be used to model the relay behavior [120]:

$$f_f = f_C \operatorname{sgn}(v_r), \quad f_C = f_{fk} = \mu_k f_N \quad (2.1)$$

where  $f_f$  is the friction force,  $v_r$  is the relative velocity between the clutch pad and the rail and  $f_C$  is the Coulomb friction which for  $v_r \neq 0$  is equal to the kinetic friction  $f_{fk}$ . The kinetic friction is related to the normal force  $f_N$  by the coefficient of kinetic friction  $\mu_k$ . In the LMMA prototype  $f_N$  is an input that can be controlled by the servo and so consequently the friction force can be controlled. The friction force from each clutch will be denoted by  $f_{fm}$ ,  $f_{fc}$  and  $f_{fs}$  for the motor, centre and spring slide.

The motor slide is mounted at one end and so does not move, the centre and spring slide have mass  $m_c$  and  $m_s$  at positions  $x_c$  and  $x_s$  respectively. At the output of the actuator the position of the load is denoted by  $x_l$ ; when driving a load of mass  $m_l$ , three equations of motion describe the three degrees of freedom:

$$m_c \ddot{x}_c + k_s (x_c - x_s) + f_{fc} \operatorname{sgn}(\dot{x}_c - \dot{x}_l) = f_M \quad (2.2)$$

$$m_s \ddot{x}_s + k_s (x_s - x_c) + f_{fs} \operatorname{sgn}(\dot{x}_s - \dot{x}_l) = 0 \quad (2.3)$$

$$m_l \ddot{x}_l + f_{fs} \operatorname{sgn}(\dot{x}_l - \dot{x}_s) + f_{fc} \operatorname{sgn}(\dot{x}_l - \dot{x}_c) + f_{fm} \operatorname{sgn}(\dot{x}_l) = 0 \quad (2.4)$$

where  $f_M$  is the force provided by the motor. The mass of the LMMA's frame and the rails is fixed to the output and so is included in the mass of the load.

The friction from the clutches results in a nonlinear system with discontinuities, such a system is difficult to model and still more difficult to control. For any given slide, when  $v_r = 0$ , the slide is no longer moving and the braking force is subject to static friction, due to adhesive forces the coefficient of static friction  $\mu_s > \mu_k$ .



While a slide is in the stick state the actuator effectively loses a degree of freedom, this will hold as long as the sum of the forces on a slide is less than the limiting force due to the static friction. Combining this stick state in one or more slides with disengaged clutches in the remaining slides allows the actuator to switch between discrete states in which the equations of motion can be reduced and simplified, greatly reducing the control task for any given mode. This use of the couplings limits the output force from the actuator to the strength of the friction force provided by the clutch pads.

When all couplings are disengaged there is no force acting on the load from the actuator, the only effect is the weight of the LMMA's frame and the friction from the linear bearings of the slides.

When the motor slide coupling is engaged the output position is fixed, this is true if, ignoring output inertia  $m_l$ , the load force  $f_l$  does not exceed the static friction:

$$\dot{x}_l = 0 \quad \text{for} \quad f_l \leq f_{fm} = \mu_s f_N. \quad (2.5)$$

If the motor length is fixed then the force can be doubled by applying the coupling of the center slide (mode 3).

With the center coupling engaged (mode 2) the motor force directly effects the output, however the inertia from the center slide and the spring slide is added to the load. The spring slide's inertia either acts through the spring or otherwise directly with the spring slide coupling engaged (mode 6):

$$f_M = (m_c + m_s + m_l) \ddot{x}_l. \quad (2.6)$$

The final output mode is series elastic, where only the spring slide coupling is engaged. Again the mass of the spring slide is added to the load inertia

$$(m_s + m_l) \ddot{x}_l + k_s (x_l - x_c) = 0 \quad (2.7)$$

$$m_c \ddot{x}_c + k_s (x_c - x_l) = f_M. \quad (2.8)$$

If the motor provides a position input  $u(t) = x_c(t)$  instead of a force input, (2.7) can be written as

$$\ddot{x}_l + \frac{k_s}{m_s + m_l} x_l = \frac{k_s}{m_s + m_l} u. \quad (2.9)$$

This provides the simple second order transfer function:

$$\frac{X_l(s)}{U(s)} = \frac{\omega_n^2}{s^2 + \omega_n^2} \quad \text{where} \quad \omega_n^2 = \frac{k_s}{m_l + m_s} \quad (2.10)$$

with the inclusion of viscous damping this transfer function becomes

$$\frac{X_l(s)}{U(s)} = \frac{\omega_n^2}{s^2 + 2\zeta\omega_n s + \omega_n^2}. \quad (2.11)$$

Fig. 2.6 shows the bode diagram of the LMMA's series elastic mode for a number of small damping ratios  $\zeta$ , the values for  $k_s$ ,  $m_s$ , and  $m_l$  were taken from the experimental setup in Section 2.5.3. The plots show the 3-dB break frequency (see Fig. 2.6) to be at 19 rad/s. The stiff mode of the actuator in contrast does not have such a resonance and so a much larger bandwidth.

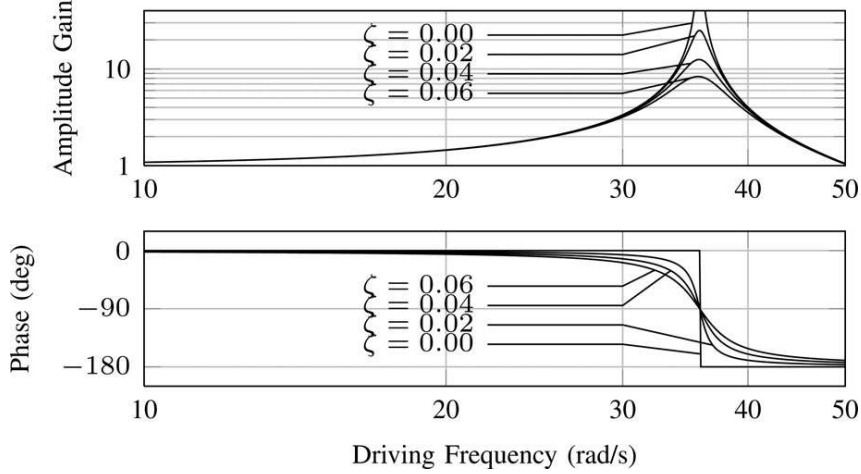


Figure 2.6: Bode plot of the open-loop response of the actuator in series elastic mode, using Eq. 2.11 with several damping ratios  $\zeta$ .

### 2.4.2 Impedance switching of the LMMA

An important property for robot actuators is the ability to control the output impedance. The LMMA prototype offers improved performance and flexibility in this regard by including both a stiff and a series elastic mode of operation. Impedance  $Z$  is the ratio of force to velocity and is a function of frequency

$$Z(\omega) = \frac{F(\omega)}{X(\omega)}. \quad (2.12)$$

For impedance control, we are interested in the force we can produce at the output of the actuator. Equation (2.6) shows the equation of motion for the actuator in the stiff position controlled mode, by ignoring load inertia  $m_l$  and converting to the frequency domain we can relate the force of the motor to the force of the load ( $F_l^{\text{stiff}}$ ):

$$F_m = F_l^{\text{stiff}} + (m_c + m_s)s^2 X_l. \quad (2.13)$$

Here it can be seen that the motor force consists of two components, the force applied to the load  $F_l^{\text{stiff}}$  and the force needed to accelerate the center and springs slides to track the load position.

A similar approach can obtain the same result for the series elastic mode, again by ignoring load inertia and converting to the frequency domain (2.7) and ((2.8) become

$$F_l + m_s s^2 X_l + k_s (X_l - X_c) = 0 \quad (2.14)$$

$$m_c s^2 X_c + k_s (X_c - X_l) = F_m. \quad (2.15)$$

Solving for  $F_m$  in terms of  $F_l$  and  $X_l$  yields:

$$F_m = F_l^{\text{elastic}} + \frac{m_c}{k_s} s^2 F_l + m_c s^2 X_l + m_s s^2 X_l \left( 1 + \frac{m_c}{k_s} s^2 \right). \quad (2.16)$$

As for the stiff actuator:  $F_l^{\text{elastic}}$  is the force applied to the load from the motor;  $\frac{m_c}{k_s} s^2 F_l$  is the force needed to accelerate the center slide to change the length of the spring;  $m_c s^2 X_l$  is the force needed to move the center slide to track the load position; and the final term is the force needed to accelerate the spring slide to track the load.

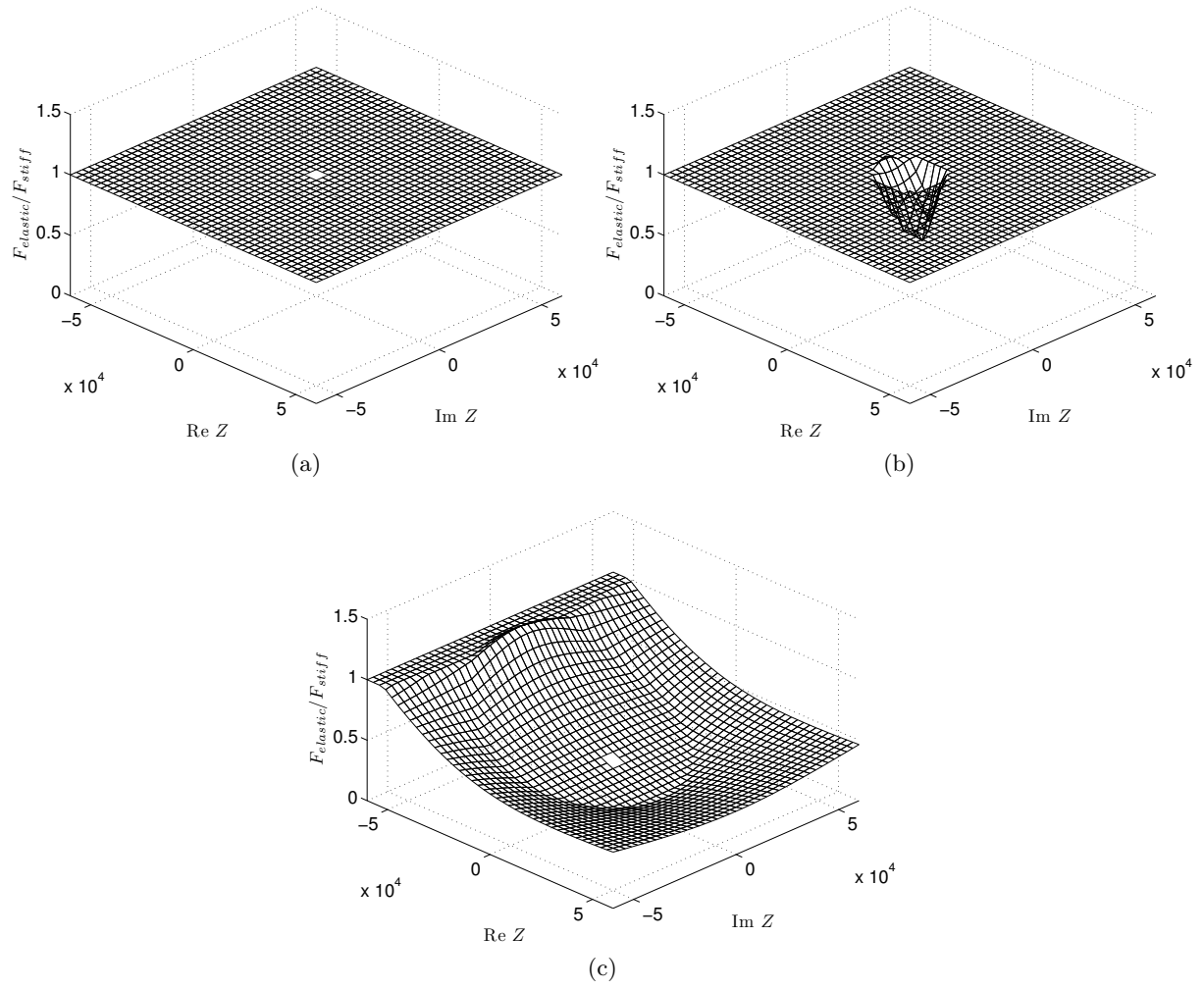


Figure 2.7: Ratio of maximum force between elastic and stiff actuation mode for a given impedance. (a) Response below resonance. (b) Response at resonance. (c) Response above resonance.

To see how much force the actuator can produce for a demand impedance at the output Eq. 2.13 and 2.16 can be written in terms of the output impedance  $Z$  from Eq. 2.12 and setting  $s = j\omega$  to give

$$F_l^{\text{stiff}} = \frac{F_m Z}{Z - (m_c + m_s)\omega^2} \quad (2.17)$$

for the stiff mode and

$$F_l^{\text{elastic}} = \frac{F_m Z}{\left(1 - \frac{m_c}{k_s}\omega^2\right)(Z - m_s\omega^2) - m_c\omega^2} \quad (2.18)$$

for the elastic mode. To compare the stiff mode with the series elastic mode the ratio of  $F_l^{\text{elastic}}$  to  $F_l^{\text{stiff}}$

$$\frac{F_l^{\text{elastic}}}{F_l^{\text{stiff}}} = \frac{Z - (m_c + m_s)\omega^2}{\left(1 - \frac{m_c}{k_s}\omega^2\right)(Z - m_s\omega^2) - m_c\omega^2} \quad (2.19)$$

can be plotted for a range of driving frequencies. Fig. 2.7 shows the result of this equation using parameters from the prototype, the maximum force for FI in both modes was limited to 400 N as this was experimentally found to be the maximum braking force. Fig. 2.7a shows the result below resonance, due to the braking limit there is no difference in performance for the two modes. At resonance the stiff mode can produce higher forces for low impedances, this is shown by the region on the surface below  $F_l^{\text{elastic}}/F_l^{\text{stiff}} = 1$  (see Fig. 2.7b). Above resonance, other than for a small region where the series elastic mode performs better the stiff mode is able to produce higher forces for a given impedance (see Fig. 2.7c).

### 2.4.3 Importance of braking force on actuator performance

In addition to the different outputs that the LMMA can produce, it also has the feature of being able to compress the on board spring to store and release energy. The spring used in this actuator is a simple linear spring with stiffness characteristics defined by Hooke's law  $f = k_s x_d$ , where  $f$  is the force applied to the spring and  $x_d$  is the deflection of the spring. The elastic potential energy of the spring  $E_e$  is given by

$$E_e = \frac{1}{2} k_s x_d^2. \quad (2.20)$$

Substituting Hooke's law back into (2.20) shows the relationship between the compression force and the stored energy

$$E_e = \frac{1}{2} \frac{f^2}{k_s}. \quad (2.21)$$

As can be seen the energy that can be stored in the spring is proportional to the square of the force available to compress it. This means that increasing the braking performance will have a large effect on the energy that can be stored in the spring.

## 2.5 Stand-alone performance of the LMMA

For the LMMA to function as intended, several different subsystems need to operate and perform correctly. In this section, we evaluate the performance of the LMMA with respect to clutch performance and the ability to switch its impedance.

### 2.5.1 Test rig and control architecture of the LMMA

The LMMA was tested experimentally by mounting it into a test rig which constrained its movement in one dimension. The test rig can be seen in Fig. 2.8, when in the vertical position the actuator could be loaded with weights, Fig. 2.8 shows the actuator loaded with 4 kg of mass. Furthermore, one end of the LMMA could be bolted to the base of the rig to prevent it from moving. A linear potentiometer measured the displacement between each of the couplings, this allowed the spring length to be recorded. The potentiometer had a range of 10 cm and was measured with an analog input built into the motor controller. The analog input had a 10 bit encoding which notionally allowed for a precision of approximately 0.1 mm although the actual precision was reduced by signal noise.

The control of LMMA was achieved through MATLAB running on a standard laptop computer. The computer communicated with a motor driver (Maxon EPOS2 70/10 motor controller) which was able to provide trajectory tracking using cubic interpolation. An Arduino Duemilanova micro controller was used to provide the control signal to the servomotors in the couplings. The specifications of the actuator are listed in Table 2.2.

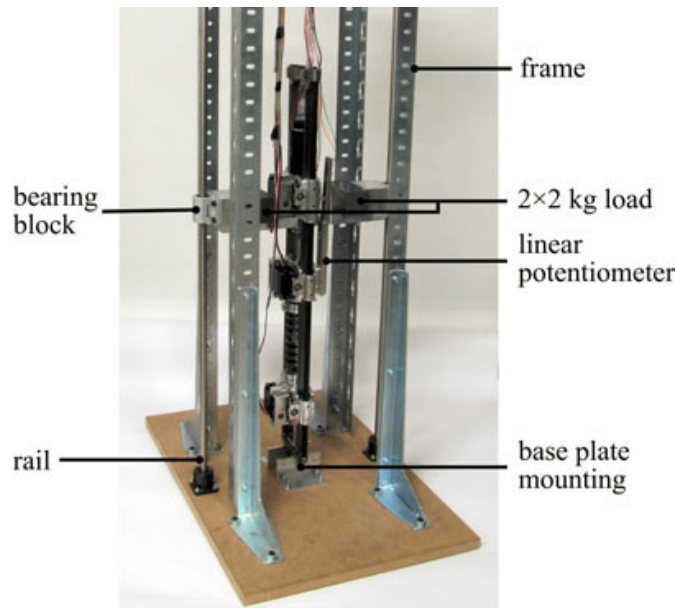


Figure 2.8: Dynamic response of the LMMA was tested while constrained to move in one dimension.

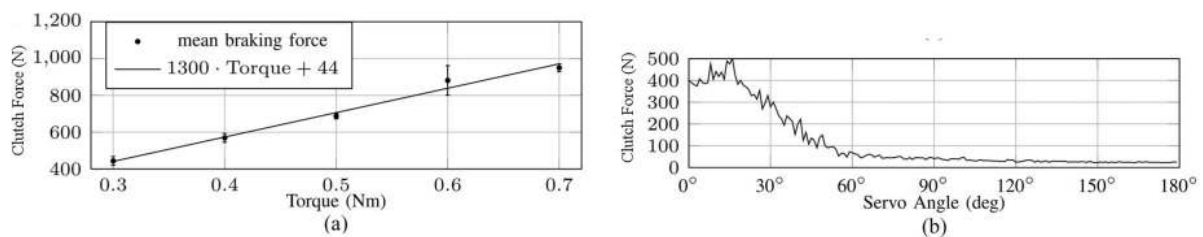


Figure 2.9: Plot of the clutch force provided by the motor slide (a) for a given torque of the worm gear shaft (see Fig. 2.5b) and (b) for a given servomotor angle.

For the LMMA to function as intended, several different subsystems need to operate and perform correctly. In this section, we evaluate the performance of the LMMA with respect to clutch performance and impedance switching performance.

### 2.5.2 Clutch performance

The braking performance was tested in two experiments. For the first experiment, the coupling servo motor was removed and a torque wrench was used to apply a specified torque to the worm gear shaft (see Fig. 2.5(b)). The relationship between the torque applied to the worm gear shaft and the braking force can be seen in Fig. 2.9(a). The error bars show the standard deviation from four measurements and a linear regression has been plotted.

For the second experiment, the coupling servomotor was used to turn the worm gear shaft to a specified angle. The relationship between servo angle and braking force is shown in Fig. 2.9(b). The servomotors have a range of  $180^\circ$  (at  $0^\circ$  the couplings are fully engaged and at  $180^\circ$  the couplings are disengaged). The time needed to move the servomotor through  $180^\circ$  is 0.7 s.

Both experiments were carried out in situ with the actuator positioned horizontally. To measure the braking force the center slide coupling was fully engaged and the motor slide coupling was engaged to the specified torque or angle. The EPOS2 motor controller permitted the motor current to be controlled. The current from the motor was gradually increased until the motor slide slipped at which point the motor current was recorded. The condition for slipping was one revolution of the ball screw which corresponds to 2 mm linear movement.

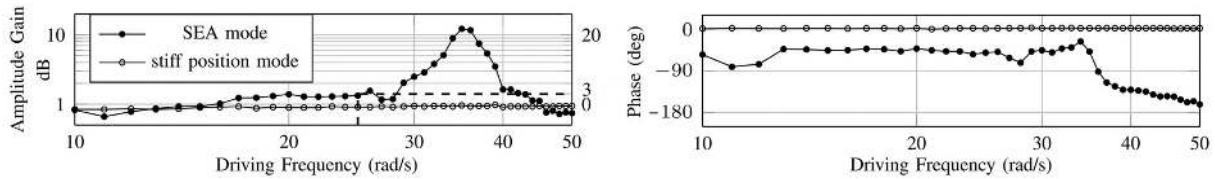


Figure 2.10: Bode plot of the open-loop response of the actuator in series elastic mode (solid circles) and the position controlled response (hollow circles) given the same input.

Using a linear spring with a stiffness of 10 N/mm, the relationship between force and current was found from the deflection of the spring for a given motor current while the actuator was in mode 5 (preloading).

The results in Fig. 2.9(a) show that the mechanism can produce braking forces of up to 1000 N. Higher forces may be possible but could not be measured as the stiffest spring available to us 25 N/mm began to buckle at this force due to its non-symmetric attachment.

Using the built in PD position control of the servomotors, the position error could be used to crudely control the braking force. When powered at 12 V the servomotors can produce 3.3 N m of torque for a position error of 30°. However, Fig. 2.9(b) shows the maximum braking force using the servomotor to be approximately 400 to 500 N. From approximately 60° and below the clutch pads start to contact the clutch rails, below 20° the clutch force levels off, this is perhaps due to saturation of the servos gain signal. There is a residual force of approximately 20 N from the thick rubber clutch pads not being fully disengaged due to the limited angular range of the servomotors.

The results show that it is possible to control the braking force with a fair amount of precision by controlling the servomotor angle between 20 and 60°. The actual switching to fully engage and disengage the couplings reduces to approximately 30% of the time required to fully rotate the servomotors, so approximately 0.2 s. Although the clutches are mainly needed to switch between modes, they may also be used to provide extra damping for the series elastic mode to prevent overshoots and oscillations.

### 2.5.3 Impedance switch

As outlined by Pratt and Williamson [61], the bandwidth of operation for a series elastic actuator is dictated by the open loop dynamics of the system, with the useful range of operation being approximately a third of the fundamental mode [90]. To identify the resonance frequency of the LMMA when operating series elastically, it was placed in the test rig to constrain it to move vertically. A 4 kg load was attached to the top of the actuator and the bottom was bolted to the test rig (see Fig. 2.8). By driving the motor with a sinusoidal position output the frequency response of the system could be identified.

This test was only carried out with loads and forces that did not cause the couplings to slip. For this LMMA, we were interested in assessing the performance of the individual discrete modes as this is how we intend to employ the LMMA. With larger forces the couplings would slip, which would cause highly nonlinear responses which are more difficult to control.

The bode plot for the series elastic mode can be seen as the filled circles in Fig. 2.10. From the plots, resonance occurs at a driving angular frequency of 36 rad/s. The usable bandwidth where the gain and phase are manageably small, is marked by the 3 dB break point which occurs at approximately 25 rad/s (3 dB corresponds to a 41% increase in amplitude). As mentioned in Section 2.5.2, even with the clutch pads fully disengaged there is still a small and inconsistent clutch force of approximately 20 N. As the friction is essentially constant for all velocities, it produces some nonlinear hysteretic behavior [121]. At low speeds especially, the residual friction force dominates and stiction can occur, this manifests itself as a phase delay in the frequency response at low frequencies. This however is an artifact of the residual friction, using

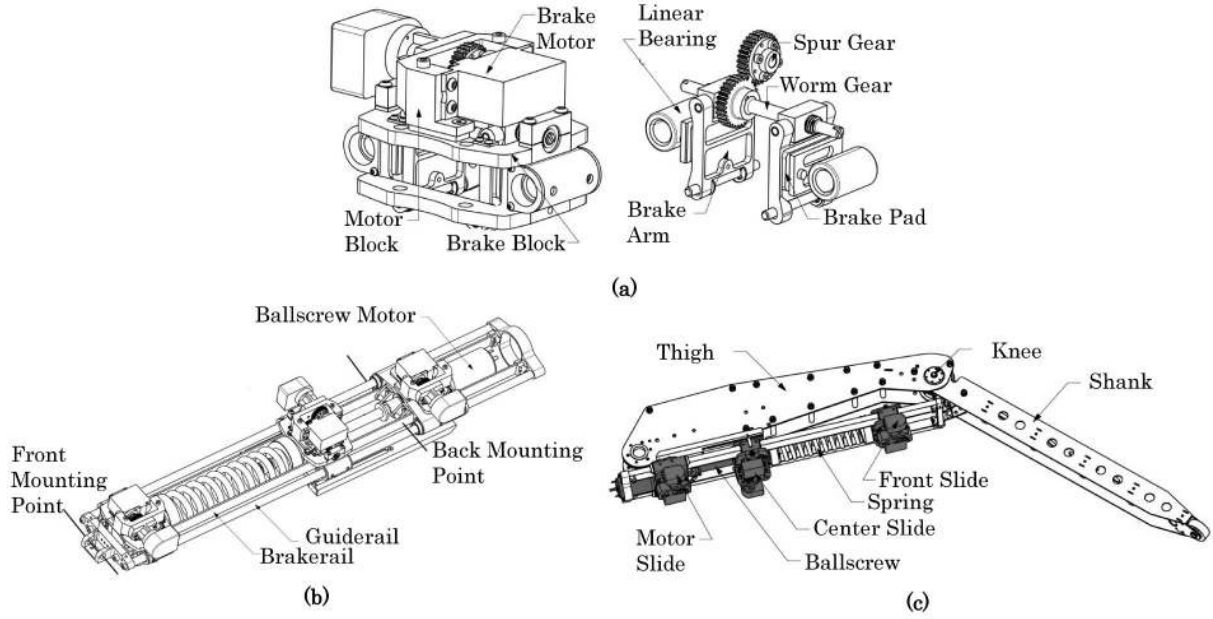


Figure 2.11: CAD Pictures of the LMMA clutch mechanism (a), the actuator itself (b) and the implementation in the robot leg (c).

a coupling mechanism that can completely disengage, the experimental response will much more closely approximate a second-order system. Although the modeled results in Fig. 2.6 are with viscous damping, the experimental results most closely match the response with a damping ratio  $\zeta = 0.02$ .

To demonstrate the benefit of being able to switch actuation modes the same test was carried out in stiff position control mode without the spring engaged, the result can be seen as the hollow circles in Fig.2.10. Across the same frequency range the gain and phase remain flat. This experimental result indicates that, because of the modes of actuation through discrete couplings, the LMMA is capable of controlling with two distinctive impedances.

## 2.6 Integration of the LMMA into a robotic leg

While the previous section investigated the performance of the LMMA in stand-alone operation, the following section aims demonstrate the use of the LMMA when attached to a robotic limb. For this purpose, we developed the planar one-legged robot ETHOP (Fig. 2.11), which is able to accommodate the LMMA for systematic experiments.

### 2.6.1 ETH hopping robot

The ETH Hopping Robot (ETHOP, Fig. 2.11) was developed specifically for the purpose of systematic investigation of the performance of LMMA in the context of hopping locomotion. The platform consists of a stand, a beam, a set of counter-weight, a hip motor, and a two-segment leg equipped with the LMMA. The technical specifications of the robot are shown in Tab. 2.3 and the dimensions are illustrated in Fig. 2.12.

The leg structure shown in Fig. 2.11(c) has two segments (thigh and shank) that are connected through a knee joint. The segments are mainly made of carbon fiber reinforced plastic, and a passive wheel is installed at the end of the shank segment, which allows the entire leg sliding lateral direction during the stance phases. In parallel to the thigh segment, the LMMA is implemented where the front mounting point of LMMA is connected to the shank segment through a pin joint fixation, and the back mounting point is connected to the thigh segment.

Table 2.3: Technical data of the ETHOP

Parameter	Value	Parameter	Value
$l_{\text{thigh}}$	600 mm	$l_{\text{kneelever}}$	70 mm
$m_{\text{thigh}}$	1100 g	$\varphi_{\text{kneelever}}$	32°
$\Theta_{\text{thigh}}$	$[2.5, 118.2, 119.5]^T \cdot 10^3 \text{kg} \cdot \text{mm}^3$	$l_{\text{x,BMP}}$	92 mm
$l_{\text{shank}}$	640 mm	$l_{\text{y,BMP}}$	56 mm
$m_{\text{shank}}$	620 g	$l_{\text{FS}}$	105 mm
$\Theta_{\text{shank}}$	$[0.3, 71.8, 71.8]^T \cdot 10^3 \text{kg} \cdot \text{mm}^3$	$lead_{\text{BS}}$	2 mm
$l_{\text{beam,Hip}}$	1830 mm	$l_{\text{S},0}$	261 mm
$l_{\text{beam,CW}}$	1490 mm	$l_{\text{S}}(t)$	221 - 281 mm
$m_{\text{beam}}$	32 073 g	$l_{\text{BS},0}$	191 mm
$\Theta_{\text{beam}}$	$[0.14, 69, 69]^T \cdot 10^6 \text{kg} \cdot \text{m}^3$	$l_{\text{BS}}(t)$	116 - 206 mm
$h_{\text{beamj}}$	980 mm	$\Theta_{\text{LMMA}}$	$[4.2, 797.2, 799.1]^T \cdot 10^3 \text{kg} \cdot \text{m}^3$
$m_{\text{LMMA}}$	4542 g	$c_{\text{spring}}$	25 N/mm
$h_{\text{hipaxis}}$	1060 mm		

The hip joint is directly mounted on the output shaft of the hip motor (MAXON RE65 with a gear head MAXON GP81, 1:25). In all of the following experiments, we assume that behaviors of this robot are only in a linear vertical hopping space. Namely, the supporting beam of the robot has two degrees of freedom (horizontal and vertical rotations) at the connection to the stand, and the horizontal rotations were set to zero by choosing adequate hip offset angles. With the counterweight, the leg mass (leg mass on the ground) can be adjusted between 0 and 14 kg.

## 2.6.2 Electronics and control

The electronics of the ETHOP consist of drivers with a power supply for hip, ball screw, and clutch motors, sensors, microcontrollers, and a host PC. For the motor drivers, we employed MAXON EPOS2 70/10, which were also used as the interface of analog sensors in the platform. Two rotational potentiometers are installed at the joint of supporting beam, one is installed at the knee joint and a linear potentiometer is installed to measure the spring length during operation. Additional rotational and linear potentiometers are installed on the hip axis and the ball screw for homing purposes.

The hip and knee actuator are controlled using the “Position-Mode” of the EPOS controllers. The host PC operates information processing and motor command communications through a Matlab interface. The PC sends the position signals with a control frequency of 50 Hz, which results in an acceptable smoothness of movement.

## 2.7 Hopping control strategies

In this section, we investigate the vertical hopping induced by two control of the eight strategies of the LMMA, namely series elastic hopping and preloaded hopping. Both hopping strategies consider the actuation in the knee joint, and the hip joint is simply compensate for the leg angle such that the ground contact should be always perpendicular, i.e  $\varphi_{\text{hipoffset}} = 0^\circ$ . This motion is achieved by measuring the knee angle  $\varphi_{\text{knee}}$  through the potentiometers in the LMMA, and the changes in this angle are reflected onto the position control of the hip motor by the target angle being  $\varphi_{\text{hip}} = -\delta\varphi_{\text{knee}}$ .



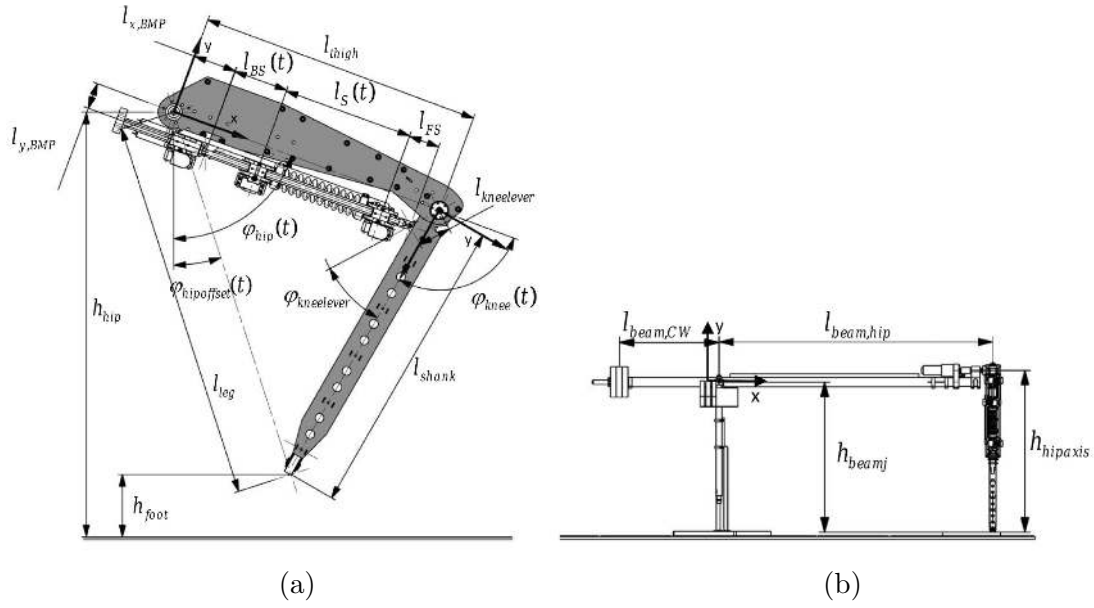


Figure 2.12: Parameters of the leg and the beam of the ETHOP.

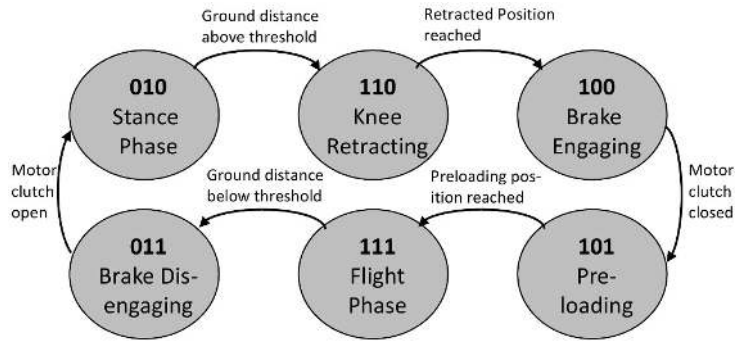


Figure 2.13: State machine diagram as we used it for the preloaded hopping experiments.

### 2.7.1 Series elastic hopping

The LMMA’s capability of switching between different actuation modes is particularly powerful in the context of tasks that require underactuated motion control such as throwing, walking, hopping, and running. The series-elastic mode for example can be used for energy efficient hopping locomotion by storing kinetic energy in the spring during a stance phase and to recycle it in the next flight phase. Series elastic hopping with open loop, sinusoidal motor position input is the simplest control strategy in our robotic platform, thus we employ this strategy as the baseline for the systematic analysis of more advanced controllers. In this strategy, the LMMA is set to mode 4 (i.e. the front slide clutch is engaged), and fixed to the same mode throughout. The ball screw motor is operated by a PID position controller, in which the host PC send a position signal as:

$$\varphi_{knee} = A \sin(\omega t) + B \quad (2.22)$$

where  $A$ ,  $B$ ,  $\omega$  are amplitude, offset, and frequency parameters, respectively. This controller does not require any global sensory feedback except for the internal position control of the ball screw and hip motors. Despite its simplicity, this controller usually results in a stable hopping behavior once the parameters in equation 2.22 are adequately adjusted.

Table 2.4: Variables of the state machine for preloaded hopping

Label	Object	State
0__	Hip height	below threshold
1__	Hip height	above threshold
.0_	Ball screw	retracted
.1_	Ball screw	protracted
__0	Motor clutch	disengaged
__1	Motor clutch	engaged

### 2.7.2 Preloaded hopping

Another unique and important feature of the LMMA is its ability to preload its spring without influencing the output and release the energy so that short bursts of high-output power can be provided. To do so, the spring is preloaded with the motor lengthening in mode 5 (preloading). To release the energy, the LMMA switches to mode 4 (SEA). In contrast to the series elastic hopping, preloaded jumping therefore requires switching between modes.

The preloaded hopping is a unique control strategy that requires a legged robot platform equipped with a LMMA. For continuous hopping, the preloading procedure is repeated during each flight phase. In theory, this strategy should provide a favorable characteristics to legged robot locomotion because the motor in the knee joint can be exploited not only during the stance phase but also in the flight phase, which is usually not the case with the conventional motors.

Practically, this control strategy can be achieved by a simple state machine, which is illustrated in Fig. 2.13 and 2.14. The state machine consists of six states that can be represented by the three-bit information shown in Tab. 2.4, and each bit indicates hip height (measured by the potentiometer on the y-axis of the beam), retract/protract of ball screw, and engage/disengage of motor side clutch, respectively.

The robot always start with “stance phase” (labeled as “010” in Fig. 2.13) in which the motor side clutch should be disengaged. Then, as soon as the leg leaves the ground and the hip height indicates above the threshold, the ball screw motor controls the knee joint to retract the leg until the knee joint reaches the desired angle (i.e. “110” state). The motor slide clutch is then engaged (i.e. “100” state), which bring the state machine to the next state “101”. In this state, the ball screw is extended for preloading the spring, which triggers the state “111”. As soon as the hip height passes the threshold again during the flight phase, the motor side clutch is disengaged such that the stored potential energy in the spring can be released to the system dynamics. In this state machine, we are able to adjust the following three parameters, i.e. the ball screw offset position, the spring compression during preloading, and the threshold of hip height.

## 2.8 Physical experiments

The two hopping control strategies were implemented and tested in the robotic platform, and we conducted a series of real-world experiments to analyze stability and power consumption of these strategies. This section explains the methods and results.

### 2.8.1 Methods

After a number of preliminary experiments, we identified a set of design parameters that facilitate the analysis of hopping performance. For a fair comparison of two control strategies explained

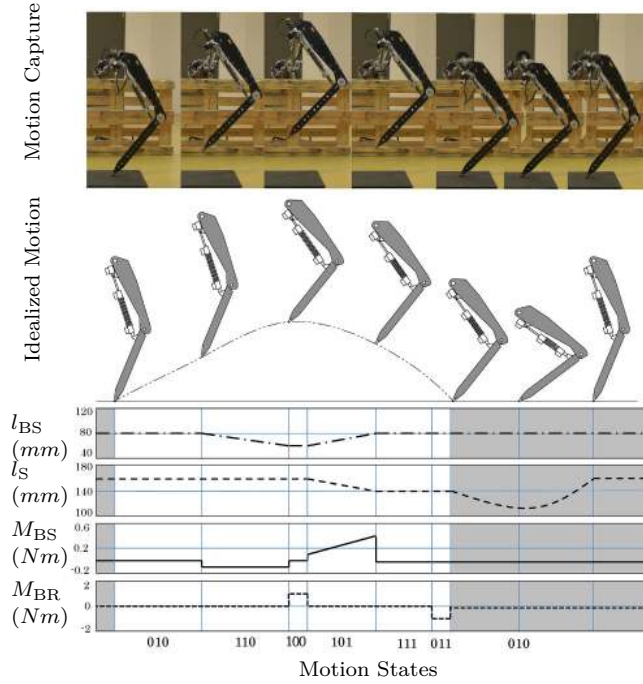


Figure 2.14: Preloaded hopping motion pattern. The stance phase is highlighted in grey. The labelling of the motion states follows Fig. 2.13 and Tab. 2.4. Below a motion capture series of one hop, the corresponding ball screw length  $l_{BS}$ , spring length  $l_S$ , ball screw motor moment  $M_{t_{BS}}$  and clutch motor moment  $M_{t_{Clutch}}$  is plotted.

in the previous section, we also tuned the control parameters such that they exhibit a similar hopping trajectory (i.e. the hopping height around 400 mm) regardless of the difference in control strategy. In the sinusoidal hopping controller, we employed a ball screw initial position of 176.2 mm (which results in an initial knee angle of  $72^\circ$ ), a ball screw amplitude of 16 mm, a ball screw frequency of 0.34 Hz and a hip offset of  $-2^\circ$ , with which the ETHOP reaches an average hopping height of 370 mm with 20 hops during the final run. And for the preloaded hopping controller, we set the control parameters as follows: a ball screw initial position of 186 mm (which results in an initial knee angle of  $64^\circ$ ), a spring compression of 24.8 mm, a spring compression speed of 45 mm/s and a hip offset of  $-2^\circ$ . With a height threshold of 174 mm the spring is released about 20 mm above the ground. Every joint angle, the ball screw and spring length as well as the current for hip, ball screw and clutch motor were measured and logged during the run. We performed 20 cycles of hopping experiments in each of the control strategies.

## 2.8.2 Hopping trajectory and stability

For each control strategy, we first analyzed the trajectory of stable hopping. In the sinusoidal hopping controller, the hopping height is mainly determined by the amplitude  $A$ . For each amplitude between 6 and 20 mm we found an optimal oscillation frequency  $\omega$  with which the hopping trajectory stabilizes into a steady state after 3-5 hops regardless of the initial hopping height. In contrast, for the preloaded hopping control, the hopping height is mainly determined by the amount of spring compression during the preloading processes.

Fig. 2.15a shows the trajectories of state variables in both control strategies. Due to the large mass and the low natural frequency of the whole system, both hopping behaviors have long flight phases (ca. 2.5-3.0 sec), and short stance phases (ca. 0.5 sec). The main difference between these two control strategies is most eminently shown in the flight-phase angular trajectories of knee joint  $\varphi_{knee}$ , which are periodic oscillation in the sinusoid hopping controller, whereas it appears to be step function in the preloaded controller. Despite the difference in joint operation,

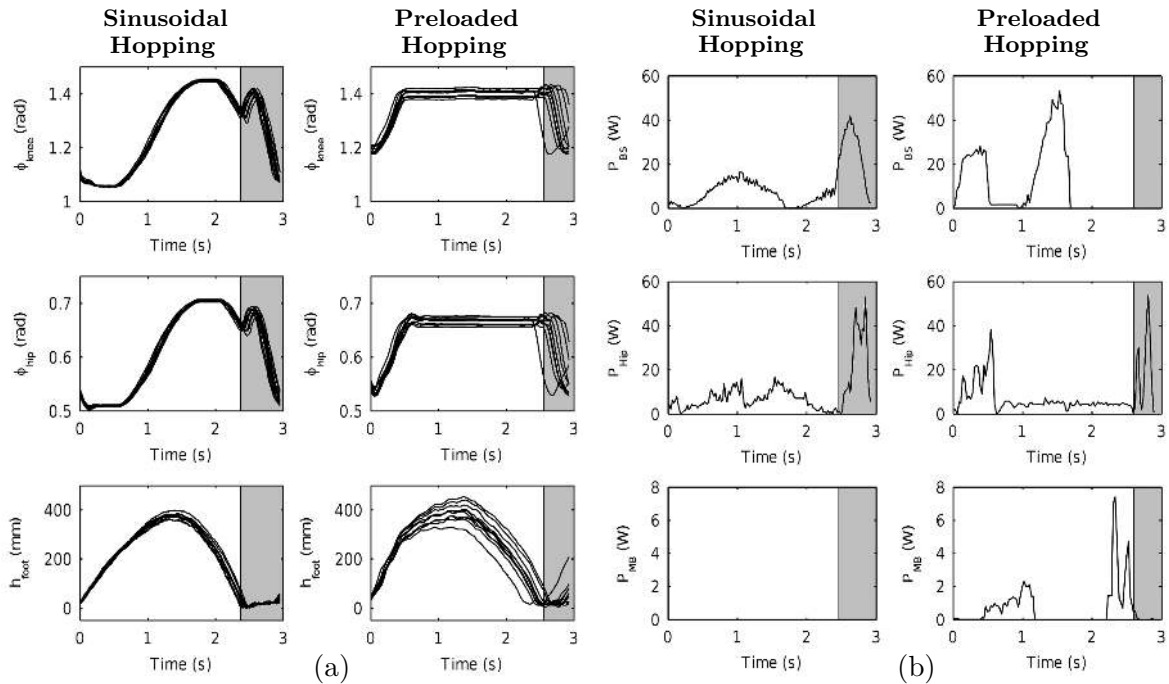


Figure 2.15: (a): Trajectory of state variables for one cycle stable behaviour during sinusoidal (left column) and preloaded hopping (right column). The trajectories of ETHOP during 10 consecutive cycles are plotted in one cycle period. The stance phase in each plot is indicated by grey areas. (b): Power consumption for one cycle stable behaviour during sinusoidal and preloaded hopping. The stance phase in each plot is indicated by grey areas.

both hopping strategies converge to a similar hopping height approximately at 370 mm.

During preloading, the knee angle in Fig. 2.15a remains at about 1.4 rad. The motor clutch starts disengaging slightly before touchdown, to ensure that the clutch rails start slipping at touch down and the motor clutch does not brake the stance phase too much. But even with ideal timing, during the slipping around touchdown with “half-engaged” clutch, a significant amount of energy is dissipated, and the motor clutch brakes down the robot at the first half of the stance phase. This can be seen in the knee angle trajectory of preloaded hopping too. Here the knee further bends at the beginning of the stance phase, but much less than one could expect.

### 2.8.3 Energy consumption

In order to further characterize the two hopping control strategies, we analyzed the power consumption of hip, ball screw and clutch motors based on the registered data during the experiments. Current and motor speed were measured during the experiments, and the voltage was estimated retroactively by using the motor constants given by the supplier. The input power consumption was calculated as the multiplication of voltage and current, the outcome of ball screw  $P_{\text{BS}}$ , hip  $P_{\text{Hip}}$ , and clutch  $P_{\text{MC}}$  motors for each of the sinusoidal and preloaded hopping controllers is shown in Fig. 2.15b. As expected, there are two significant differences in these two control strategies. On the one hand, we observe energy consumption in the clutch motors in the case of preloaded hopping, which do not appear in the sinusoid one; And on the other, the energy consumption of ball screw motor appears during the flight phase in the preloaded hopping whereas it is in the stance phase for the sinusoidal hopping. The differences in the behaviors of ball screw motor is mainly originated in the preloading of the spring during the stance phase, while this does not influence the energy consumption in the hip motor.

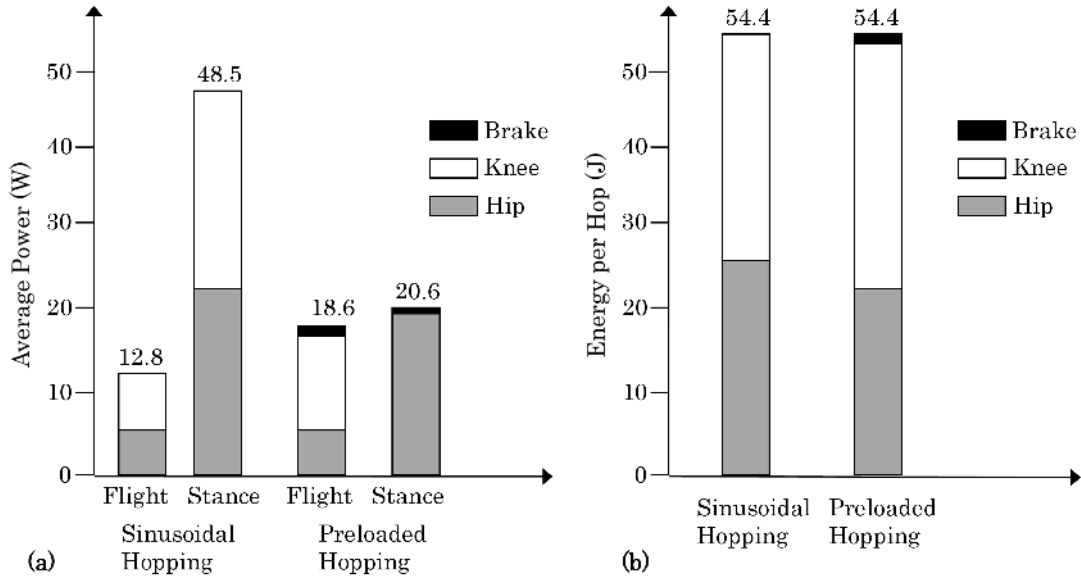


Figure 2.16: Power consumption of the two hopping control strategies at the same hopping height concerning the average power in flight and stance phase (a) and the total energy per hop (b).

Fig. 2.16 shows more comprehensive analysis on the energy expenditure during the stance and flight phases in each of the control strategies for identical hopping height. In general, the hip energy consumption is significant, up to 50 percent of the total energy consumption, but even due to a different distribution, the total hip energy consumption per hop is nearly equal for preloaded and sinusoidal hopping. The clutch energy consumption adds up to only one percent of the ball screw power consumption. The ball screw power distribution in flight and stance phase shows a totally different behavior between sinusoidal hopping and preloaded hopping. In preloaded hopping, all the energy is consumed during flight phase, while in sinusoidal hopping the consumption happens mostly during stance phase.

As stated in Section 2.8.2, preloaded hopping with friction clutches causes inevitable losses due to the slipping of the clutch around touch down. But even with these losses, the energy consumption of preloaded hopping is equal to sinusoidal hopping at the same hopping height. This means that, on the other hand, preloaded hopping has the potential to be more energy efficient than sinusoidal hopping, as soon as the slipping losses could be reduced.

## 2.9 Conclusion

We have introduced a new method of mechanically switching between different modes of operation within a single actuator online using discrete couplings. We first generalized the conceptual model of the use of discrete couplings, and analyzed a case study with a linear motor, a mechanical spring, and three couplings that yielded eight modes of operation. Even this relatively simple implementation showed how the mode switching could produce numerous outputs that improve the performance range of the series elastic actuator, by allowing stiff position control, as well as introducing new behaviors such as preloading energy into the spring and rigidly fixing the output length. The most significant challenge of this approach is to design a braking mechanism that could fit on board and provide a high enough braking force. The current solution using thick rubber clutch pads is able to provide up to 400 N that can be achieved by a switching operation of approximately 0.2s. A test rig was used to further evaluate the performances of LMMA, and demonstrated a large bandwidth of motion control and the ability to vary its impedance depending on the spring configuration. Furthermore, one of the most unique capa-

bilities of LMMA is the use of discrete couplings to charge the mechanical spring through the DC motor, with which the LMMA can trigger a short burst of energy for an instantaneous high jump. This preloading capability has been demonstrated with the LMMA mounted at the knee of a robotic leg, allowing for hopping through preloading the spring during flight and bouncing passively during stance.

Due to the fact that engagement and disengagement take a significant amount of time, friction clutches are most suitable for reconfiguration during standstill. Although constant reconfiguration during the run has been successfully demonstrated in this paper, the applied preloaded hopping scheme shows the limitations of friction clutches for these dynamic tasks. Due to the necessary disengagement time, the friction clutches dissipate energy at touchdown due to slipping, which lowers the potentially good energy efficiency of preloaded hopping.

The future work will therefore focus on the coupling mechanisms that can, on the one hand, increase holding forces, and on the other, minimize the physical size and weight as well as the necessary time for engaging and disengaging. According to our experimental results, the improvement of coupling mechanisms will further enhance the impact of this novel actuation strategy. In addition, we also expect to investigate the design principles of control architecture for this novel actuation strategy.



## Chapter 3

# Improving hopping height control of legged robots by using coupling-based series elastic actuation<sup>1</sup>

Coupling based series elastic actuation, as introduced in the previous chapter, represents a powerful approach to increase the possible number of actuation dynamics a series elastic actuator can exhibit. In this chapter, we present an in-depth investigation of three of the actuation strategies provided by this actuator, namely (1) the series elastic, (2) the actuator locking and the (3) preloading strategy. All three strategies are investigated in simulation and the series elastic and preloading strategy are then verified by using an experimental monopod hopping platform. In the simulation and physical experiments, we demonstrate that the springy dynamics enabled by the couplings allow for increased hopping height with under limited actuator peak force.

In the theoretical setup, an idealized model of couplings is used, which act as discrete switches between different configurations. These idealized couplings engage and disengage instantly with no energy consumption and at any position. They can produce infinite holding forces and while engaging can deal with arbitrary relative speeds of the bodies which need to be coupled. Physical clutches, on the other hand, have limitations in all their parameters, and these limitations strongly depend on their mechatronic design. Therefore, a physical actuator with identical theoretical setup can exhibit different behavior when equipped with a different type of couplings. Or, from the application point of view, different requirements strongly influence the choice of the coupling type.

Coupling based series elastic actuation is a general approach which can be realized with various coupling technologies. In the first generation of our CE-SEA presented in the previous chapter, we made use of friction clutches since they allow for coupling at arbitrary positions and enable energy dissipation while closing, i.e. the bodies to be coupled can have a relative speed while the coupling closes. Both features ease the control by reducing the number of constraints the controller needs to handle. In this chapter, we now present the second generation of this CE-SEA. It makes use of the same overall approach, but this time with ratchet pawl mechanisms, which belong to the group of form-fit clutches.

---

<sup>1</sup>This chapter presents the collaborative work with my colleague H.Q. Vu under the guidance of my supervisor F. Iida. I designed the physical platform, performed simulation and physical experiments and contributed to the writing of the manuscript. My colleague H.Q. Vu and my supervisor F. Iida contributed to the discussion and the writing of the manuscript. This chapter has been adapted and edited from the following publication:

- F. Guenther, H.Q. Vu, and F. Iida. Improving hopping height control of legged robots by using coupling-based series elastic actuation. *Conditionally accepted for publication in IEEE Transactions on Robotics*



In contrast to friction clutches, ratchet pawl mechanisms allow for very compact design with high force density. The mechanism itself is simpler and contains less parts, and when properly actuated, ratchet pawl mechanisms can open and close extremely fast. Another prominent difference lies in the fact that ratchet pawl mechanisms are unidirectional, i.e. they lock a motion in one direction but behave completely passive in the other. While this might be a drawback for some applications, this feature turns out to be very beneficial for the preloading strategy.

To preload the spring during flight phase, one coupling is necessary to lock the joint. And at touchdown, the same coupling needs to be able to release the joint instantly. Since preloading requires locking in one direction, and the release at touchdown occurs in the opposite direction, ratchet pawl mechanisms are a good match for this application. In order to protect the actuator from the high spring forces during stance, a second coupling is necessary which locks the actuator. Again, while the locking is only necessary in one direction (the compression direction in our case), preloading occurs in the opposite direction (extension), which makes a ratchet pawl mechanism again suitable for the task.

Ratchet pawl mechanisms feature a limited number of discrete closing positions. For preloaded hopping, we preload with the leg being at rest length, so a single closing position of the joint coupling is sufficient. For the actuator clutch, our mechanism allows for closing every 0.5 mm along the length of the actuator's ballscrew, which is sufficient for precisely controlling the energy input during preloading.

The LMMA presented in the previous chapter is a modular platform which can be extended with different clutch types and clutch motors, depending on the task. For the experiments presented in this chapter, the front clutch of the LMMA is closed, and in addition, the front slide touches the front of the rail. This acts as an additional geometric end stop, enabling the front clutch to handle the clutch forces up to 2100 N which occur during hopping in this chapter. Center and motor clutch are open, with the center clutch motor removed. The motor clutch motor drives not the motor clutch, but instead the two ratchet mechanisms in the knee and on the ballscrew. Due to an improved spring mounting, the buckling noted in the previous chapter does not occur and the spring can be compressed up to 2100 N spring force.

### 3.1 Introduction

Actuation dynamics has been a long-standing research topic for control of agile robot motions, in particular dynamic legged robot locomotion. As shown by a number of previous case studies [41, 86, 122, 123], a pertinent realization of actuator dynamics can not only provide better locomotion performance but also facilitate the control processes. In the past, many legged robots, especially for the hopping and running gait patterns based on the pogo stick principle [29], made use of series elastic actuation (SEA, [61]), where the actuation mechanism consists of a mechanical spring incorporated in series with an actuator. SEA dynamics can, on the one hand, offer a simple solution to cope with large impacts at touchdown [41], and on the other, provide energetic efficiency by elegantly storing and releasing elastic energy [122] as well as relax the control demand through the self-stabilizing characteristics [86] and increase the peak power output of the actuator [92].

Conventional SEA-based legged locomotion utilized the elastic elements only during the stance phase because of the necessity of counter force in the spring, i.e. the series elasticity cannot be used without the existence of the ground reaction forces. However, there has been also innovative solutions in which elastic elements can be utilized during the flight phase, for example based on an actuated string attached to the spring [34]. With such a mechanism, the elastic element can be charged during the flight phase, and this energy can then be utilized for the subsequent stance phase.

In this chapter, the main goal is to investigate a solution to do both flight and stance phase actuation within one and the same series elastic actuator. We therefore establish a template

[47] by extending a SEA with two independent discrete couplings (CB-SEA). In this template, counter-forces for the spring can be created regardless of stance or flight phases during the locomotion, and the system has therefore substantially more flexibility in actuation dynamics. Using both theoretical and physical platforms, we argue that, by employing a CB-SEA in a hopping robot, (1) the system is able to perform a larger maximum hopping height under the constraint of maximum force output of the actuation element, and (2) the system is able to adjust hopping height with a larger range given the design specifications of mechanical spring and actuation element. These two hypotheses were investigated both in simulation and physical experiments.

Similar to our approach, previous robots applying flight phase actuation all incorporate on some kind of coupling mechanism, which essentially enables engagement and disengagement of the spring and the actuator at desired timings. Previously there were a few coupling mechanisms proposed for the purpose of robot locomotion (for review, see [82]), like pulley-string mechanisms [34], [124] or friction clutches [2] for continuous hopping with monopods, solenoid-based solutions for passive dynamic walking with bipeds [57], electromagnetic clutches for prosthetic use [125], or eccentric cam mechanisms [43–45], ratchet pawl mechanisms [83] or linkage mechanisms with geometric singularities [126] in robots inspired by jumping insects [22]. Commercial electric clutches have also been used between gear stages to connect parallel elastic elements [127] to a robotic joint. More recently, a parallel spring mechanism was combined with a differential drive, and friction clutches allow the system to store energy in the spring at arbitrary positions [128]. Although these mechanisms are relevant to our work as discussed later in this chapter, none of these previous works have investigated actuation during stance and flight phase within one and the same actuator.

For a systematic investigation of CB-SEA, we structured the rest of the chapter as follows: Section 3.2 introduces a theoretical template of hopping robots with discrete couplings. Section 3.3 presents results of simulation experiments using this template, which compare the performance of different hopping control schemes and evaluates the advantages of the proposed approach. Section 3.4 presents a case study of a physical prototype equipped with discrete couplings, which is then followed by discussion and conclusion.

## 3.2 Hopping robot template with discrete couplings

This section introduces a new hopping robot template which we investigate in this chapter, together with three different control schemes for vertical hopping. The model we use for the simulation experiments (Fig. 3.1) consists of a mass  $m$ , a massless linear prismatic actuation element AE, a massless spring  $c$ , and a massless friction element FE<sup>2</sup>. The mass  $m$  is connected in series with the AE and the spring to represent a SEA. The energy losses in the system are modelled by the friction element FE acting in parallel with the SEA, and the spring has a point contact to the ground. In addition, the model contains two massless discrete coupling elements DC1 and DC2. With DC1, it is possible to lock the AE at any desired position while DC2 does the same with the entire SEA. Both coupling elements are assumed to open and close instantly without any time delays.

### 3.2.1 Hopping dynamics and actuation without discrete couplings

With the discrete couplings DC1 and DC2 open, the simulation model (Fig. 3.1) behaves like a normal SEA. Its leg length  $l_{\text{Leg}}$  and the initial leg length  $l_{\text{Leg},0}$  can be described as

$$l_{\text{Leg}} = l_{\text{S}} + l_{\text{AE}}, \quad l_{\text{Leg},0} = l_{\text{S,rest}} + l_{\text{AE},0} \quad (3.1)$$

---

<sup>2</sup>We chose friction instead of damping since damping is not able to represent the losses during coupling series elastic actuation adequately. See Section 3.5 and Appendix 3.7 for details

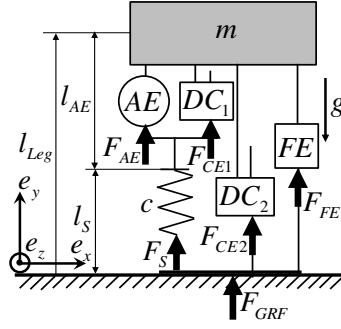


Figure 3.1: Simulation setup containing a mass and a spring with parallel friction element FE and serial actuation element AE. In addition, two discrete couplings are mounted in parallel to the the actuation element (DC1) and the whole actuator (DC2).

where  $l_S$  is the length of the spring ( $l_{S,\text{rest}}$  being the relaxed rest length of the spring), and  $l_{AE}$  is the length of the actuation element ( $l_{AE,0}$  being its initial length). These parameters which we use in the simulation can be found in Tab. 3.1.

During hopping, the position of the mass at time  $t$  is determined by  $y_m(t)$  and the model dynamics alternately switches between stance phase and flight phase. The transition from stance to flight, i.e. the leg leaves the ground during *liftoff* ( $LO$ ), is detected based on

$$y_m = l_{AE} + l_{S,\text{rest}}, \quad \dot{y}_m > 0, \quad (3.2)$$

with  $l_{AE}$  being the actuator length and  $l_{S,\text{rest}}$  being the rest spring length and  $\dot{y}_m$  being the velocity of the mass. The transition from flight to stance, i.e. the leg touches the ground at *touchdown* ( $TD$ ), is defined based on

$$y_m = l_{\text{Leg},0}, \quad \dot{y}_m < 0. \quad (3.3)$$

With these assumptions, the equation of motion of the present model can be described as follows. Since FE, AE and the spring are assumed to be massless, only gravitational force acts on the mass during flight:

$$\ddot{y}_m + g = 0. \quad (3.4)$$

In stance phases, the gravitational force and the ground reaction force are exerted to the system, thus:

$$m \cdot \ddot{y}_m - F_{\text{GRF}} + m \cdot g = 0. \quad (3.5)$$

The ground reaction force is equivalent to the sum of the friction force  $F_{\text{FE}}$  and the spring force  $F_S$ , therefore:

$$\ddot{y}_m - \frac{F_{\text{FE}}}{m} - \frac{F_S}{m} + g = 0. \quad (3.6)$$

Here we assume the spring force  $F_S$  is linear with spring stiffness  $c$  as:

$$F_S = c \cdot \Delta l_S = c \cdot (l_{S,\text{rest}} - l_S). \quad (3.7)$$

The friction element FE is in parallel to the SEA and is only active during stance phase. We assume Coulomb Friction [129], where the friction force at FE is linearly proportional to the spring force with friction coefficient  $\mu$

$$\text{Stance Phase: } F_{\text{FE}} = -\text{sign}(\dot{y}_m) \cdot F_S \cdot \mu \quad (3.8)$$

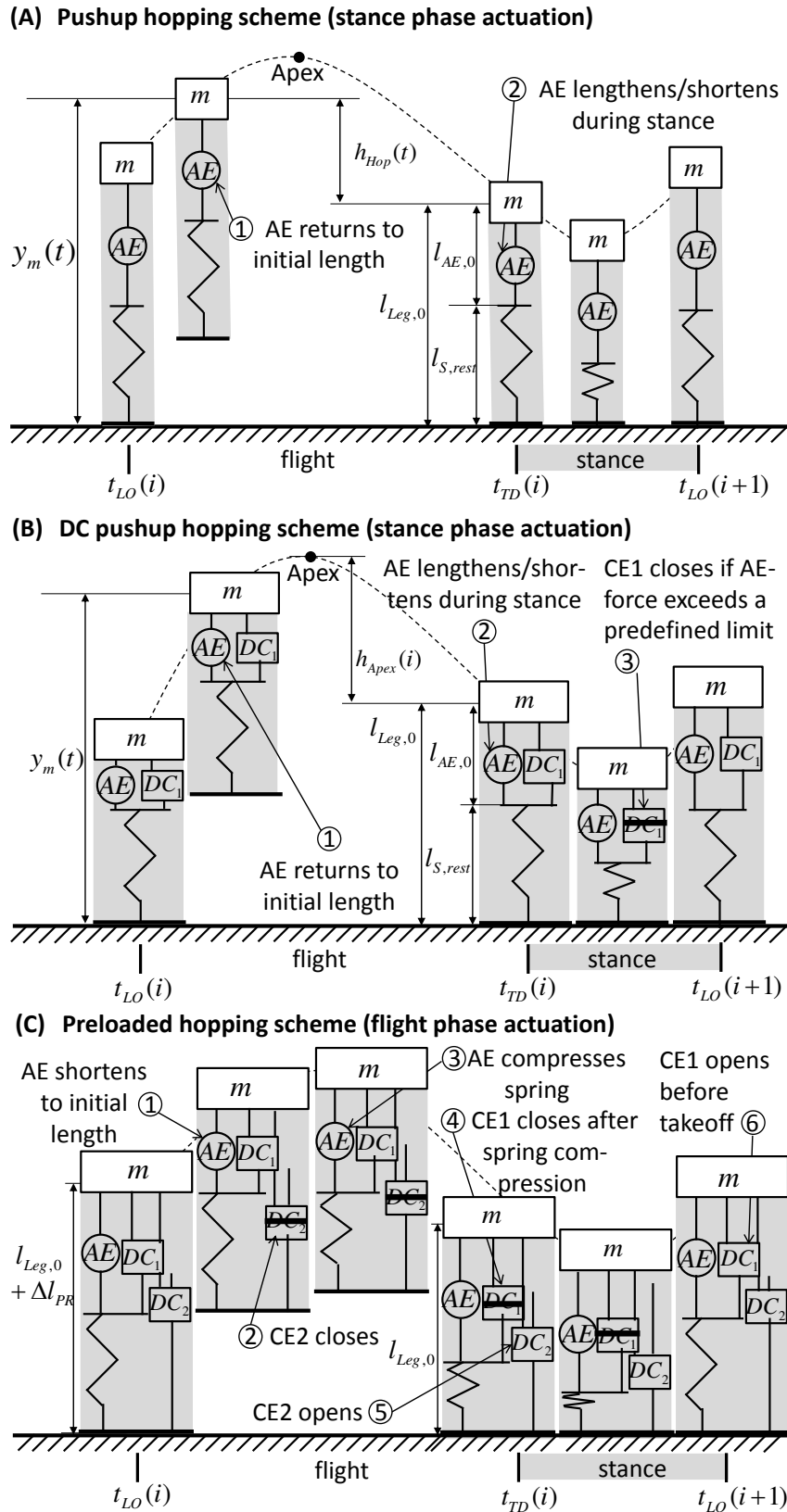


Figure 3.2: Illustrated time series of pushup, DC pushup and preloaded hopping with important variables. The friction element FE is not shown.

$$\text{Flight Phase: } F_{\text{FE}} = 0. \quad (3.9)$$

Due to the fact that spring, AE and FE are massless, no impact losses are assumed in this model.

The hopping height is defined with respect to the initial leg length:

$$h_{\text{Hop}} = \begin{cases} y_m - l_{\text{Leg},0} & \text{if } y_m \geq l_{\text{Leg},0} \\ 0 & \text{if } y_m < l_{\text{Leg},0}, \end{cases} \quad (3.10)$$

while the maximum hopping height within  $i$ th step is called apex hopping height and is defined as follows:

$$h_{\text{Apex}}(i) = \max(h_{\text{Hop}}(t)), \quad t \in [t_{\text{LO}}(i) \dots t_{\text{TD}}(i)]. \quad (3.11)$$

For convenience, we define dimensionless parameters, labelled as  $\tilde{l}$ ,  $\tilde{h}$ ,  $\tilde{F}$ , and  $\tilde{c}$ , which are used hereafter.  $l_{\text{AE}}$ ,  $\dot{l}_{\text{AE}}$ ,  $l_S$ ,  $\Delta l_S$  and  $h_{\text{Apex}}$  are thereby normalized with the initial leg length  $l_{\text{Leg},0}$  ( $\tilde{l}_{\text{AE}} = \frac{l_{\text{AE}}}{l_{\text{Leg},0}}$ , ...) while  $F_{\text{AE}}$  and  $F_{\text{GRF}}$  are normalized with body mass  $m$  and gravity  $g$  ( $\tilde{F}_{\text{AE}} = \frac{F_{\text{AE}}}{m \cdot g}$ , ...). Finally, the dimensionless spring stiffness  $\tilde{c}$  is defined as

$$\tilde{c} = c \cdot \frac{l_{\text{Leg},0}}{m \cdot g}. \quad (3.12)$$

Because we assume friction losses in our simulation model, it is necessary for the AE to supply energy into the system for continuous hopping. To hop without discrete couplings (stance phase actuation), the AE *pushes* (i.e. lengthens) with fixed velocity  $\tilde{l}_{\text{AE}}$  during stance phase and returns to initial length during flight phase (Fig. 3.2a). For the sake of clarity and to differentiate from the other control strategies presented later in this chapter, we call this control strategy *pushup hopping*. One step of simulated pushup hopping (Fig. 3.3a) starts at liftoff, where the AE shortens back to initial length and remains there until touchdown. At touchdown, the AE starts lengthening with constant velocity and stops either if the maximum AE length is reached or if liftoff occurs. At the beginning of the stance phase, spring and ground reaction force increase. At mid stance, where the spring force  $F_S$  has its maximum, the friction force  $\tilde{F}_{\text{FE}}$  changes direction which causes a step in the ground reaction force. After mid stance, the spring lengthens and bounces the mass back up.

One of the characteristics for pushup hopping is that actuation element AE has to bear the whole spring force during stance. Because of that, pushup hopping is only applicable if the peak spring force and therefore the peak AE force  $\tilde{F}_{\text{AE,peak}}$  lies below the maximum AE force  $\tilde{F}_{\text{AE,max}}$ . If the maximum AE force is exceeded during stance, the AE continues moving and the run will be considered as AE-overload afterwards. In addition to supply energy, the AE is also able to remove energy by shortening from its initial length after touchdown either until liftoff occurs or the minimum AE length is reached.

### 3.2.2 Hopping dynamics and actuation with discrete couplings

By making use of the discrete couplings DC1 and DC1 (Fig. 3.1), a few additional ways to achieve vertical hopping become possible. In this chapter, we focus on two additional control schemes which we call pushup hopping with discrete couplings (DC pushup hopping) and preloaded hopping.

*DC pushup hopping* (Fig. 3.2b) is similar to pushup hopping with the AE lengthening/shortening during stance and returning to initial length during flight. But in DC pushup hopping, the discrete coupling DC1 avoids a rise of the actuator force above a given limit  $\tilde{F}_{\text{AE,limit}}$  by closing when the spring force exceeds this limit. Simulated trajectories (Fig. 3.3b) show that the force

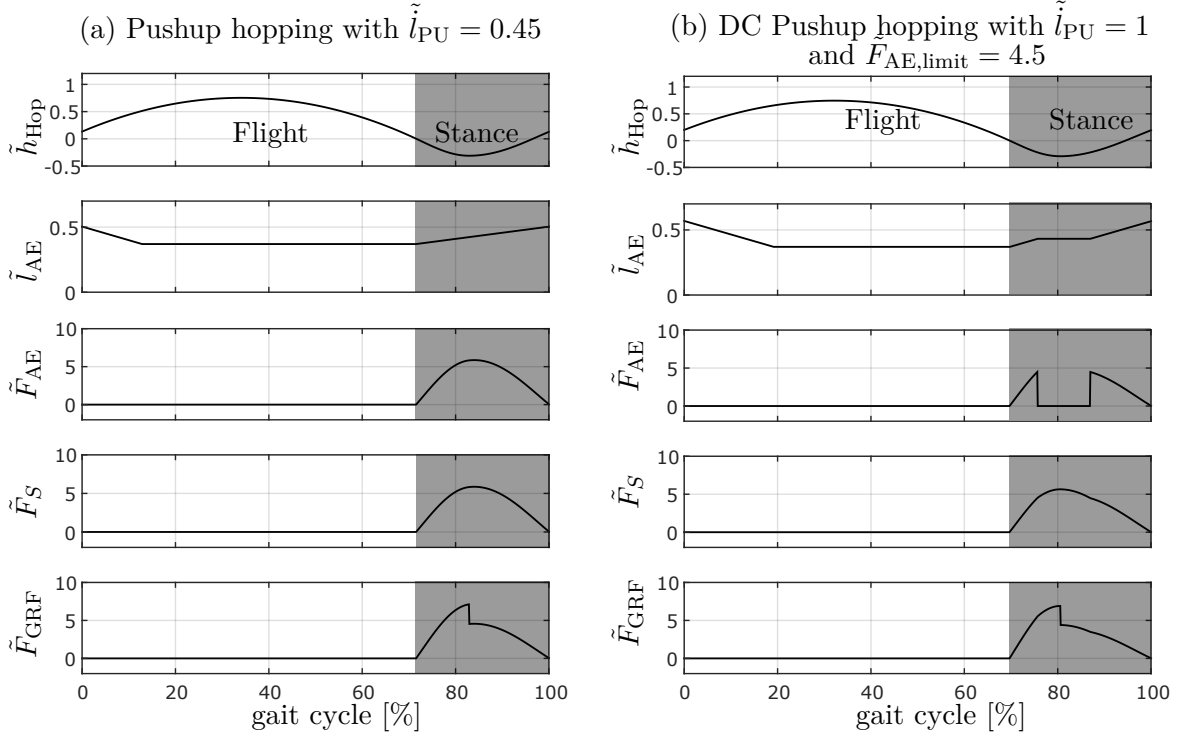


Figure 3.3: Trajectories of hopping parameters during pushup hopping (a) and DC pushup hopping (b). All parameter plots are shown in one gait cycle. The gray areas indicate the stance phase.

at the AE stops rising above  $\tilde{F}_{\text{AE,limit}} = 4.5$  because DC1 closes at 76 % of the hopping cycle and remains closed until 87 %. The equations of motion of DC pushup hopping are almost identical to those of the pushup hopping scheme (see Eq. (3.5) and (3.6)), except for the modification in stance phase as follows:

$$\tilde{F}_{\text{AE}} = \tilde{F}_{\text{S}}, \quad \tilde{F}_{\text{DC1}} = 0 \quad \text{if } \tilde{F}_{\text{S}} \leq \tilde{F}_{\text{AE,limit}} \quad (3.13)$$

and otherwise

$$\tilde{F}_{\text{AE}} = 0, \quad \tilde{F}_{\text{DC1}} = \tilde{F}_{\text{S}}, \quad (3.14)$$

where  $\tilde{F}_{\text{AE,limit}}$  designates the variable force limit set by the controller. As for pushup hopping, DC pushup hopping is also able to remove energy from the system by shortening during stance. In DC pushup hopping, only  $\tilde{F}_{\text{AE,limit}}$  is used as a continuous control variable. The AE speed  $\tilde{l}_{\text{PU}}$  for DC pushup hopping is set to  $\tilde{l}_{\text{PU,max}}$  for energy input or  $\tilde{l}_{\text{PU,min}}$  for energy removal, respectively (see also Tab. 3.1).

For the flight phase actuation with the *preloaded hopping* control scheme (Fig. 3.2c and Fig. 3.4), the discrete couplings DC1 and DC2 are operated differently. When starting from liftoff, both DC1 and DC2 are open. After the actuation element AE shortened to its initial length  $\tilde{l}_{\text{AE},0}$ , DC2 is closed, and subsequently the spring is loaded by lengthening the AE with a preloading distance  $\Delta\tilde{l}_{\text{PR}}$ . The AE is then locked by closing DC1 to protect it from the ground impact, with the clutch taking the load and the AE force going to zero. Before touchdown, the leg is at initial length  $l_{\text{Leg},0}$ , while the actuator length is  $l_{\text{AE}} > l_{\text{AE},0}$ , depending on the amount of preloading of the spring. At touchdown, DC2 opens instantly and releases the stored elastic energy in the mechanical spring. This release introduces a large jump in the ground reaction force  $\tilde{F}_{\text{GRF}}$  at touchdown. During stance, the spring is passively compressed and then bounces back by releasing all of the energy stored through preloading and mass acceleration. Because

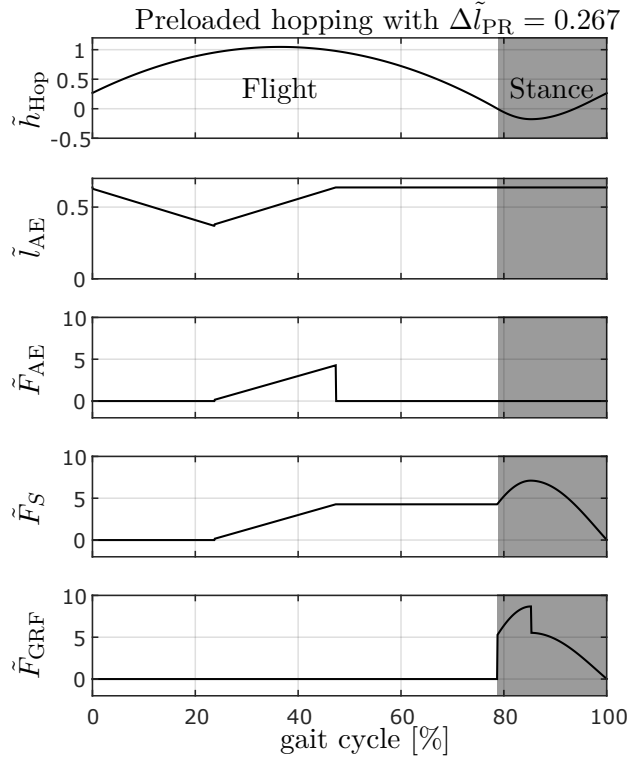


Figure 3.4: Trajectories of hopping parameters during preloaded hopping. All parameter plots are shown in one gait cycle. The gray areas indicate the stance phase.

of the assumption of a massless leg, the equation of motion in this control scheme is the same as the previous one, except for the preloading in the spring at the beginning of stance phase, namely:

$$\tilde{F}_S(t_{TD}) = \tilde{c} \cdot \Delta \tilde{l}_{PR}. \quad (3.15)$$

It is important to mention that preloaded hopping seems to reduce the duty factor, i.e. the percent of the gait cycle the leg is in stance phase, when compared to pushup and DC pushup hopping.

### 3.3 Simulation experiments

This section shows numerical simulation analysis of the hopping robot template and control schemes explained in the previous section. We analyze the hopping control schemes with respect to stability, maximum hopping height, leg efficiency influence and hopping height controllability. All simulation experiments in this chapter were conducted under Matlab.

#### 3.3.1 Mechanical efficiency

During stance without actuation, the leg of the simulation model bounces passively, and the hopping height of the following flight phase  $h_{Apex}(1)$  will be either equal (no mechanical losses during stance) or lower (mechanical losses during stance) than the initial apex height  $h_{Apex}(0)$ . In physical platforms, mechanical losses during stance phase are manifold, with collision losses, dynamic and rolling friction in the bearings, fluid damping of grease, air drag or inner damping of the parts being only a few examples. A general formulation of these losses can be done with the energy balance, comparing the total energy at touchdown and liftoff. The ratio between these two energies can be described as the *mechanical efficiency* of the platform. Since the touchdown

Variable	Dimension	Meaning
<b>(a) Parameters</b>		
$g$	9.81 m/s <sup>2</sup>	Gravitational acceleration
$l_{\text{Leg},0}$	1 m	Initial leg length
$m$	10 kg	Body mass
<b>(b) Dimensionless Parameters</b>		
$\tilde{c}$	[16, 24]	Spring stiffness
$\tilde{l}_{\text{AE},0}$	0.37	AE initial length
$\tilde{l}_{\text{S,rest}}$	0.63	Spring rest length
$\mu$	[0..0.67]	Friction coefficient in FE
<b>(c) Dimensionless Control Input Variables</b>		
$\tilde{F}_{\text{AE,limit}}$	[0..5.92]	Limit AE force (where DC1 opens/closes)
$\Delta\tilde{l}_{\text{PR}}$	[0..0.37]	AE preloading distance
$\tilde{l}_{\text{PU}}$	[-1..1]	AE pushup speed
<b>(d) Dimensionless Limits</b>		
$\tilde{F}_{\text{AE,max}}$	5.92	Maximum allowed AE force
$\tilde{F}_{\text{S,max}}$	[10.08, 15.12]	Max spring force
$\tilde{l}_{\text{AE,max}}$	0.74	Max AE length
$\tilde{l}_{\text{AE,min}}$	0	Min AE length

Table 3.1: Parameters of the simulation model

and liftoff energy are directly proportional to the initial and subsequent apex hopping height (assuming lossless flight phase), we define the mechanical efficiency  $\Psi$  for a certain initial apex height  $\tilde{h}_{\text{Apex}}(0)$  as follows:

$$\Psi_{\tilde{h}_{\text{Apex}}(0)} = \frac{\tilde{h}_{\text{Apex}}(1)}{\tilde{h}_{\text{Apex}}(0)}. \quad (3.16)$$

It is important to mention that the mechanical efficiency as defined in Eq. (3.16) depends on the initial apex height  $\tilde{h}_{\text{Apex}}(0)$  (Fig. 3.5a, see also Fig. 3.2b and Eq. 3.11). For friction losses as implemented in our simulation model, higher initial apex heights lead to a higher mechanical efficiency, with this effect being reduced at higher hopping heights. In contrast to the initial apex height, the influence of the spring stiffness on the mechanical efficiency is much smaller (Fig. 3.5b). In our simulations, both dependencies are included. However, to be able to compare different setups with one scalar, we therefore define the *nominal mechanical efficiency* at initial leg length:

$$\Psi_0 = \frac{\tilde{h}_{\text{Apex}}(1)}{l_{\text{Leg},0}}. \quad (3.17)$$

### 3.3.2 Asymptotic behavior of hopping height

To keep the system simple and the number of control parameter low, the actuation element AE follows predefined trajectories during flight and stance phase, triggered by liftoff and touch-down, but without including any continuous feedback. For pushup and DC pushup hopping for example, this results in a sort of reflex control [130]. And for preloaded hopping, constant energy input during each step is achieved by preloading the spring during the flight phase. The



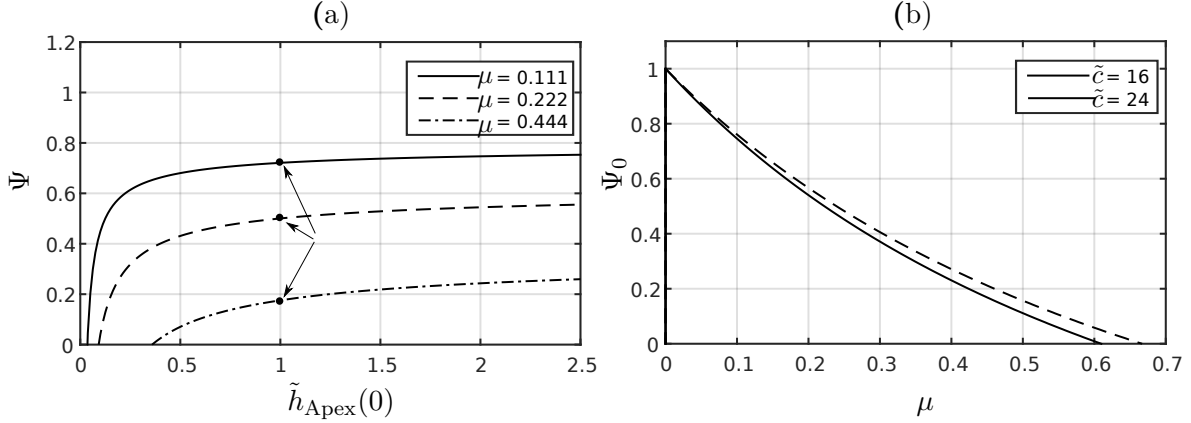


Figure 3.5: (a) Mechanical efficiency  $\Psi$  depending on the initial apex hopping height  $\tilde{h}_{\text{Apex}}(0)$  for three different friction coefficients  $\mu$  with  $\tilde{c} = 16$ . (b) Nominal mechanical efficiency  $\Psi_0$  depending on the friction coefficient  $\mu$  for two different spring stiffnesses  $\tilde{c}$ .

resulting trajectories of the mass  $y_m(t)$  are therefore determined by the passive dynamics of the SEA model introduced in Section 3.2. During the whole parameter range of this model, each specific set of control input variables  $\tilde{F}_{\text{AE,limit}}$ ,  $\Delta\tilde{l}_{\text{PR}}$ ,  $\tilde{l}_{\text{PU}}$  resulted either in a distinct steady state hopping height (if the AE input is large enough) or in no hopping at all (if the AE input is too small). To visualize this behavior, we plotted 15 seconds of hopping for each hopping scheme, starting from two different initial hopping heights (Fig. 3.6).

For pushup hopping, it can be seen that the hopping height always converges to an equilibrium determined by  $\tilde{l}_{\text{PU}}$  regardless of the initial conditions. Convergence is thereby relatively slow and no overshooting is visible. DC pushup hopping shows similar behavior, but the convergence is faster and overshooting can be observed at the first apex when starting at initial apex height 0.1 with  $\tilde{F}_{\text{AE,limit}} = 2.5$ . In the case of pushup hopping, even though its the control strategy of preloaded hopping significantly differs from pushup and DC pushup hopping, a slowly converging behavior without overshooting similar to pushup hopping can be observed.

### 3.3.3 Hopping height with limited actuator peak force

To compare the performance of pushup, DC pushup, and preloaded hopping, we analyze the influence of the peak actuator force on the steady state apex hopping height. Therefore, we conducted a numerical simulation of the hopping robot models by considering the dimensionless peak actuator force  $\tilde{F}_{\text{AE,peak}}$ . Specifically, we chose the control input variables  $\tilde{F}_{\text{AE,limit}}$ ,  $\tilde{l}_{\text{PU}}$ ,  $\Delta\tilde{l}_{\text{PR}}$  in a range that covers the whole hopping space from minimum possible steady state apex height to the point where the peak actuator force reaches the structural limit of the AE ( $\tilde{F}_{\text{AE,max}} = 5.92$ ). We employed a hopping model with two spring stiffness  $\tilde{c} = [16, 24]$ , and applied the pushup, the DC pushup and the preloaded hopping control scheme to compare the resulting steady state apex height.

As shown in Fig. 3.7a, the steady state apex height of preloaded hopping at  $\tilde{F}_{\text{AE,peak}} = \tilde{F}_{\text{AE,max}}$  is 179% higher compared to pushup hopping and the DC pushup hopping apex height is 50% higher compared to pushup hopping.

The main underlying reason of this result lies in the fact that the preloaded hopping scheme consumes energy only during the flight phases for compressing the spring, without the AE getting confronted with the ground reaction force. Therefore, the force limit of the AE can be used completely for the energy input. In contrast, the pushup hopping scheme supplies actuator energy during the stance phase when the spring energy conversion takes place at the same time. This combination confronts the AE with the force of the spring energy conversion, which limits

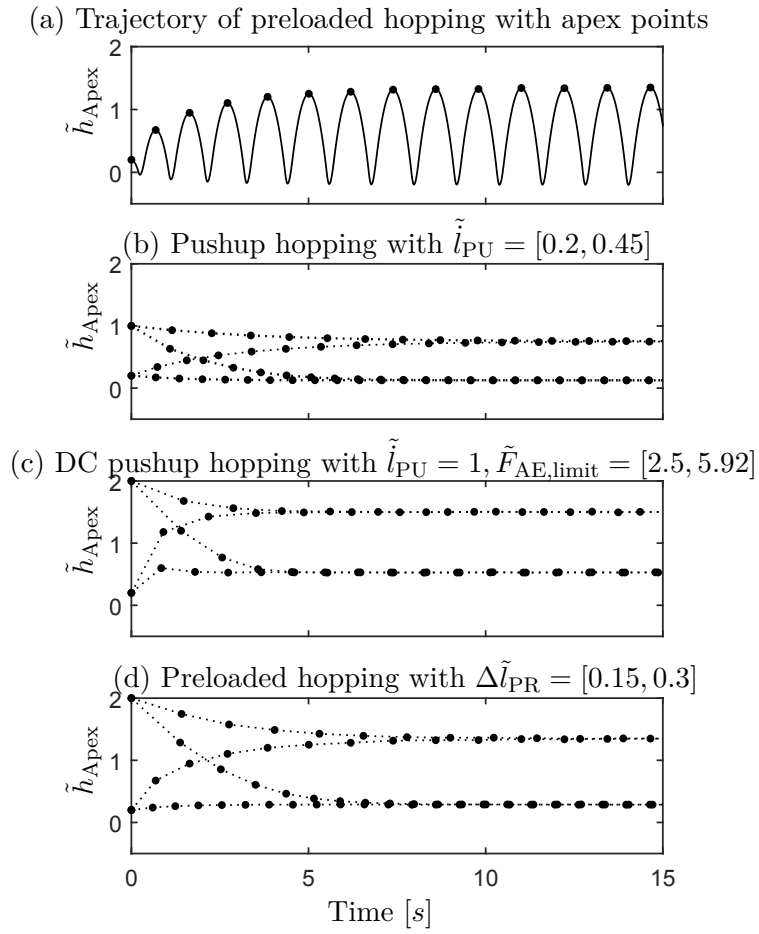


Figure 3.6: Asymptotic behaviour for pushup (b), DC pushup (c) and preloaded hopping (d) with  $\Psi_0 = 0.5$ , starting from two different hopping heights. The apex of each hop is highlighted with a black dot. (a) shows the whole body trajectory for illustration purposes.

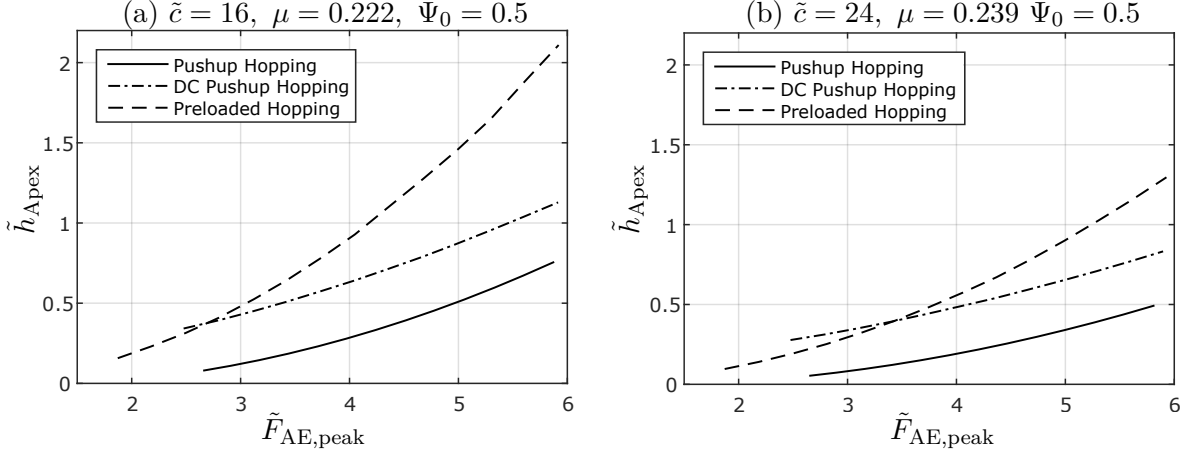


Figure 3.7: Maximum possible apex height  $\tilde{h}_{\text{Apex}}$  of steady state hopping as a function of peak AE force  $\tilde{F}_{\text{AE,peak}}$  for pushup, DC pushup and preloaded hopping at two different spring stiffnesses  $c$ . Friction coefficients  $\mu$  are tuned to allow for identical  $\Psi_0$  for both spring stiffnesses  $c$ .

its capacities for effective energy input.

The DC pushup hopping scheme performs better than the pushup hopping scheme, but due to the high percentage of inactivity during stance while  $\tilde{F}_S > \tilde{F}_{\text{AE,limit}}$ , DC pushup hopping is not able to reach the performance of preloaded hopping at larger hopping heights. However, at lower  $\tilde{F}_{\text{AE,peak}}$ , DC pushup hopping reaches higher steady state apex height than preloaded hopping. At a higher spring stiffness (Fig. 3.7b), the performance of all three hopping schemes is reduced, while DC pushup and preloaded hopping remain superior compared to pushup hopping. To clarify the influence of the spring stiffness in detail and to predict an optimal spring stiffness for each actuation scheme, additional investigations are necessary.

### 3.3.4 Influence of nominal mechanical efficiency to hopping height

Although the previous section showed the significant advantage of the DC pushup and the preloaded hopping scheme to achieve larger hopping heights, these benefits vary with the mechanical efficiency of the system. To show the influence of the nominal mechanical efficiency on the hopping performance, we conducted additional simulation experiments by analyzing the possible steady state apex hopping height with respect to variations of friction coefficient in the leg models. Therefore, we set the control input variables  $\tilde{F}_{\text{AE,limit}}$ ,  $\tilde{l}_{\text{PU}}$ ,  $\Delta\tilde{l}_{\text{PR}}$  in a way that the maximum possible steady state apex hopping height  $\tilde{h}_{\text{Apex}}$  is reached with the peak actuator force  $\tilde{F}_{\text{AE,peak}}$  equal to  $\tilde{F}_{\text{AE,max}}$ . To achieve different nominal mechanical efficiencies  $\Psi_0$ , we vary the friction coefficient  $\mu$  according to Fig. 3.5b such that  $\Psi_0$  covers its full range between 0 and 1. For each friction coefficient, we use exhaustive search to determine the control input variables  $\tilde{F}_{\text{AE,limit}}$ ,  $\tilde{l}_{\text{PU}}$ ,  $\Delta\tilde{l}_{\text{PR}}$  which allow for maximum possible steady state apex hopping height  $\tilde{h}_{\text{Apex}}$  with the peak actuator force  $\tilde{F}_{\text{AE,peak}}$  equal to  $\tilde{F}_{\text{AE,max}}$ . All parameter limits are set according to Tab. 3.1d. As a result, Fig. 3.8 shows numerical simulation of the maximum possible steady state apex height for different nominal mechanical efficiencies  $\Psi_0$  within these limits.

In the case of DC pushup and preloaded hopping, there is a significant trend that the steady state apex height increases as the nominal mechanical efficiency increases, whereas, in the case of pushup hopping, the same metric stays almost the same in the range (or even decreases slightly). From this analysis, it can be seen that the preloaded hopping scheme has an advantage when the nominal mechanical efficiency is  $\Psi_0 > 0.12$ , and DC pushup hopping has an advantage for every  $\Psi_0 > 0$ .

The observation of nearly constant steady state apex height for pushup hopping can be

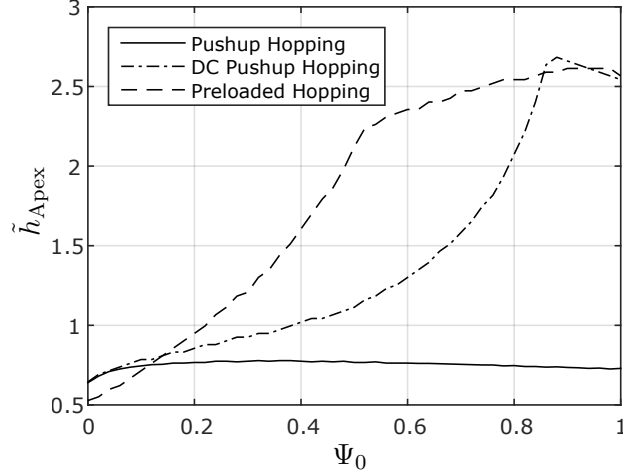


Figure 3.8: Maximum possible apex height  $\tilde{h}_{Apex}$  of steady state hopping as a function of the nominal mechanical efficiency  $\Psi_0$  for pushup, DC pushup and preloaded hopping for  $\tilde{c} = 16$ . All parameters are limited according to Tab. 3.1D.

explained by looking at the energy balance of the stance phase. On the one hand, the necessary energy input for constant hopping height is not constant but increases with decreasing  $\Psi_0$ . On the other hand, the lower  $\Psi_0$  is, the longer the stance phase becomes (the data is not shown in this chapter). In addition, the possible actuator speed and therefore the distance the actuator is able to travel during stance time increases with lower  $\Psi_0$  too. Consequently the actuator can supply the more energy during the longer stance time. This increased energy supply equals the increased energy consumption, which allows for keeping the steady state height constant. At  $\Psi_0 = 0$ ,  $\tilde{l}_{PU}$  is set slightly below its positive limit  $\tilde{l}_{PU,max} = 1$  and is then continuously reduced to  $\tilde{l}_{PU} = 0$  for  $\Psi_0 = 1$ .

In contrast to pushup hopping, the preloaded hopping scheme supplies a constant amount of energy every step thus hopping height increases as the efficiency is improved (i.e. nominal mechanical efficiency  $\Psi_0$  increases). Below  $\Psi_0 = 0.12$ , the energy supply of preloaded hopping is smaller compared to pushup hopping, and therefore the resulting hopping height becomes smaller. The increase of hopping height of preloaded hopping slows down at approximately  $\Psi_0 = 0.52$ , which is due to the leg spring being fully compressed during stance ( $\tilde{F}_S = \tilde{F}_{S,max}$ ). Above  $\Psi_0 = 0.52$ , the robot needs to reduce the preloading distance and therefore the energy input per hop to protect the spring. Below  $\Psi_0 = 0.52$ , the preloading distance is set to  $\Delta\tilde{l}_{PR} = 0.37$ . Above  $\Psi_0 = 0.52$ , the spring preloading is constantly reduced down to  $\Delta\tilde{l}_{PR} = 0$  at  $\Psi_0 = 1$ .

The DC pushup hopping starts at  $\Psi_0 = 0$  with the positive limit  $\tilde{l}_{PU} = 1$ . Since  $\tilde{F}_{S,peak}$  is below  $\tilde{F}_{AE,limit}$  at this point, the performance of DC pushup and pushup hopping is identical. Due to the protection of AE through DC1,  $\tilde{F}_{AE,limit}$  can remain on its maximum up to  $\Psi = 0.86$  and the possible hopping height increases. After  $\Psi = 0.86$ , the spring is maximally compressed and  $\tilde{F}_{AE,limit}$  is reduced down to  $\tilde{F}_{AE,limit} = 0$  at  $\Psi_0 = 1$ .

### 3.3.5 Hopping height controllability

Apex to apex dynamics were used in many locomotion research in the past [131, 132]. In this section, we look at the ability of the different control schemes to control various apex hopping heights between two steps.

Assuming the leg is in a step  $i$  at an apex height  $\tilde{h}_{Apex}(i)$ , how can we design a controller to achieve the target apex height  $\tilde{h}_{Apex}(i+1)$ ? And which of the three control schemes presented in the previous section should be employed for the purpose? In order to answer to this question,

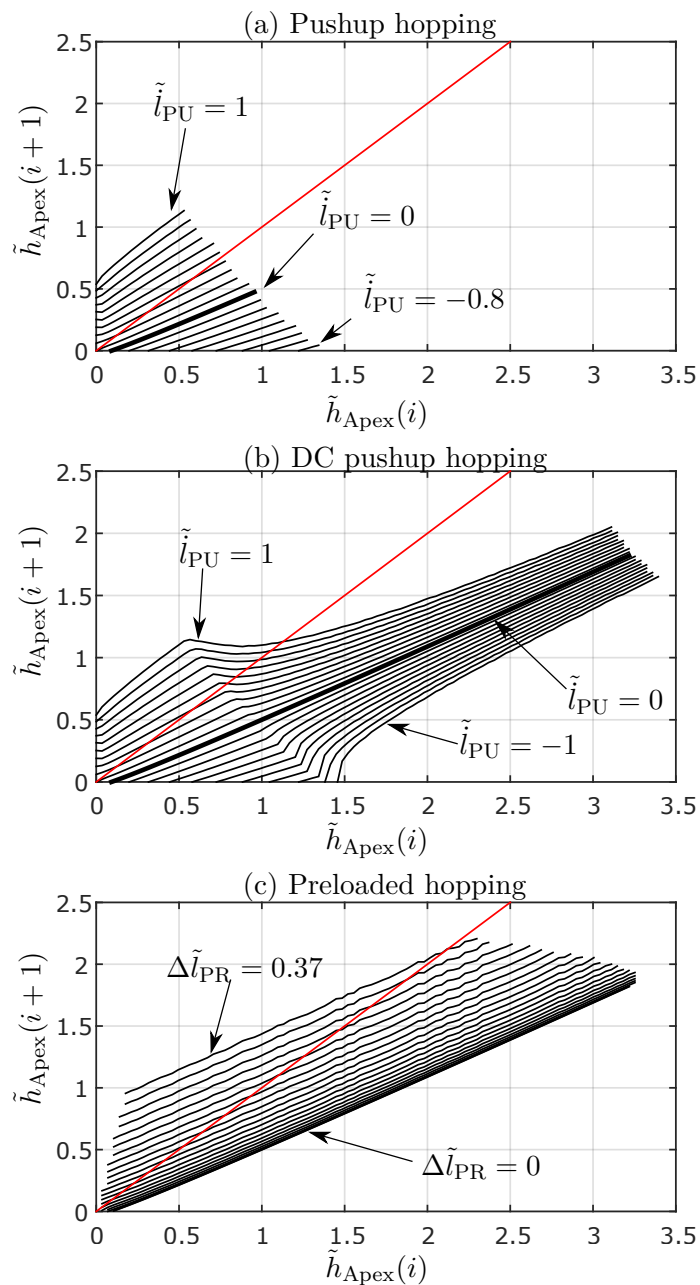


Figure 3.9: First return map of apex height  $\tilde{h}_{\text{Apex}}$  for pushup, DC pushup and preloaded hopping. Parameters are limited according to Tab. 3.1D.  $\tilde{F}_{\text{AE,limit}}$  is 5.92,  $\tilde{c}$  is 16, and friction is 0.222, resulting in a nominal mechanical efficiency of  $\Psi_0 = 0.5$ .

we conducted a series of simulation experiments by examining the parameter space up to the limits shown in Tab. 3.1D, and observed which hopping scheme is able to achieve which apex height factors from a given apex height. The ability to change the apex height between two steps in a certain manner thereby follows the concept of output controllability, with the apex height as the controlled output,  $\tilde{F}_{\text{AE,limit}}$ ,  $\tilde{l}_{\text{PU}}$ ,  $\Delta\tilde{l}_{\text{PR}}$  as the available control inputs and the time between two subsequent hopping apexes as the finite control time.

Fig. 3.9 shows the simulation results of this analysis. First to mention is the red diagonal line, which marks steady state hopping without change in the apex height. Every entry above means increasing the apex height, while every entry below this line leads to a decrease. The black lines label solutions with identical actuator parameters, i.e. constant  $\tilde{l}_{\text{PU}}$  or  $\Delta\tilde{l}_{\text{PR}}$ . The right end of these lines is determined by the system limits,  $\tilde{F}_{\text{AE,max}}$  for pushup hopping, and  $\tilde{F}_{\text{S,max}}$  for DC pushup and preloaded hopping. During several consecutive hops with identical actuator input, the apex height moves along its correspondent line towards the equilibrium on the red steady state hopping height line, which contains the stable fixed points of the hopping motion.

Having said that, we will focus on the three hopping control schemes. For pushup hopping (Fig. 3.9a), the maximum possible steady state apex height is about 0.753. At  $\tilde{h}_{\text{Apex}}(i) = 1$ , the actuator is not able to maintain the hopping height any more, in fact the robot needs to brake down at least to 40% of the previous height to protect the actuator from overload. In contrast, with the DC pushup hopping scheme shown in Fig. 3.9b, maintaining hopping height up to  $\tilde{h}_{\text{Apex}} = 1.128$  becomes possible. In addition, the region around  $\tilde{l}_{\text{PU}} = 0$  is significantly enlarged. There the system can fall down from  $\tilde{h}_{\text{Apex}}(i) = 3.4$  without exceeding actuator or spring limit. The preloaded hopping scheme (Fig. 3.9c) features an even more enlarged steady state hopping height up to  $\tilde{h}_{\text{Apex}}(i) = 2.101$ . On the other hand, the preloaded hopping scheme does not provide much advantage for lowering hopping height, since the AE cannot dissipate energy during stance.

### 3.4 Mechanical realization and physical experiments

The simulation model presented in the previous sections represents a minimalistic template to describe coupling-based series elastic actuation. In this section, we investigate the ability of this template to predict the behavior of a much more complex physical prototype. After introducing this physical platform and its implementation of the pushup and preloaded hopping control schemes, we then conduct a series of physical experiments and discuss how the simulation data from the template matches to the physical data.

#### 3.4.1 Hopping robot platform with discrete couplings

For conducting hopping experiments, we use a multi-purpose one-legged robot platform, the ETH hopping Robot *ETHOP* (Fig. 3.10a and 3.10b). The platform consists of a two-segmented leg equipped with a coupling-based series elastic actuator at the knee joint, and a direct electrical drive at the hip joint. The leg is connected at the hip to a supporting boom with some counterweight. The counterweight is used for eliminating boom, hip motor and some of the leg weight. The foot is equipped with a horizontal wheel to enable sideways motion when bouncing on the ground. A pitch potentiometer at the axis of the supporting boom measures the hopping height of the leg while a linear potentiometer at the spring measures the spring deflection, which is then used to calculate the spring force. Ground contact is detected with a switch at the foot tip. The technical data of the *ETHOP* is summarized in Tab. 3.2, and first hopping experiments were previously reported in [2]. The coupling based series elastic actuator is realized by using a modified Linear Multi Modal Actuator (LMMA, [1]) in series elastic mode. The high level position commands for every of the three motors of the *ETHOP* are created by a state machine

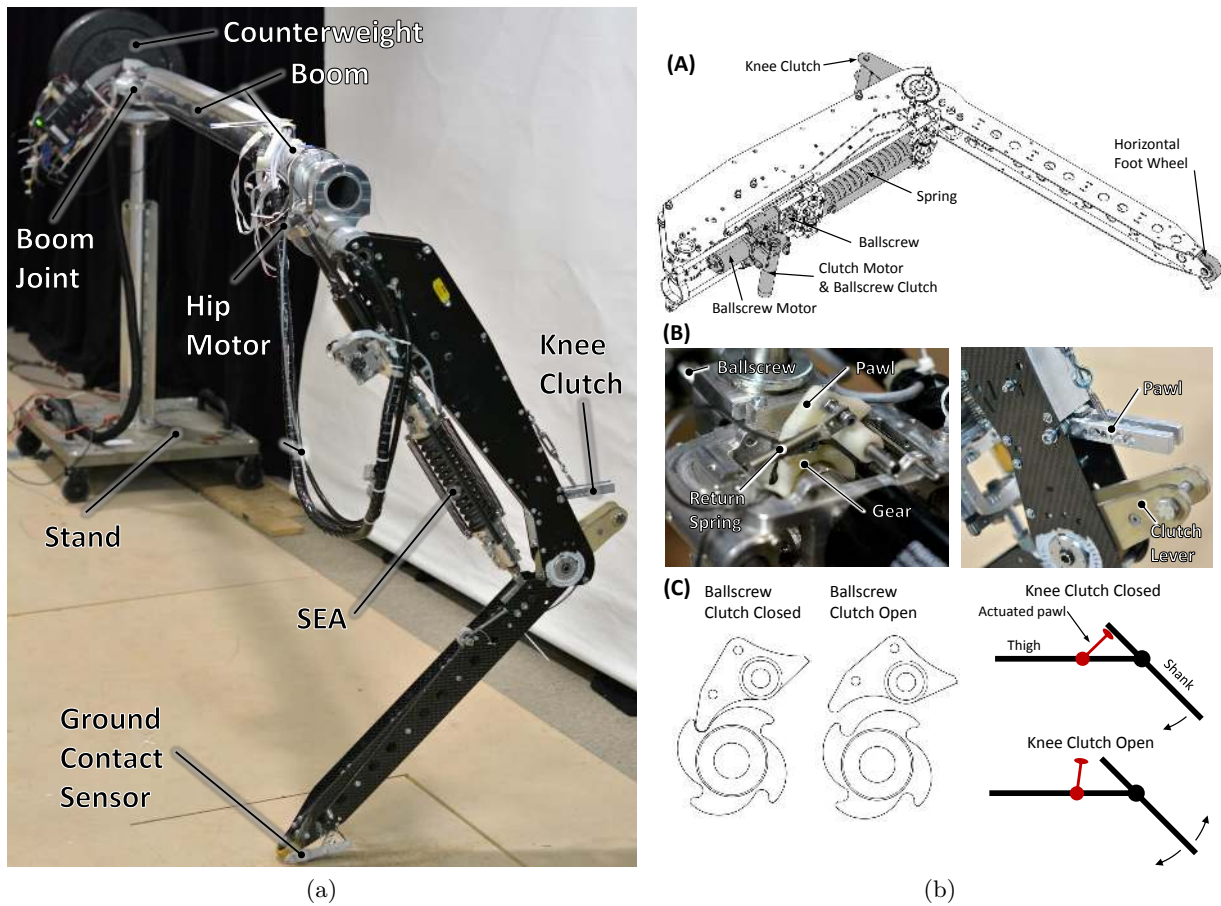


Figure 3.10: (a) Robotic platform ETHOP with the leg, the SEA, the boom and the counterweight. (b) CAD Pictures of the ETHOP robot: (A) Leg of the ETHOP with series elastic actuator (LMMA [1]) and knee ratchet mechanism. (B) Ballscrew and knee ratchet mechanism in detail. (C) Schematics for the ballscrew and the knee ratchet mechanism.

running on a PC with MATLAB at 30 Hz. Low level position control is done by using predefined control functions on the motor controllers themselves, operating at about 1 kHz.

To implement the hopping control schemes in the ETHOP platform, two discrete couplings (Fig. 3.1) are necessary. Thereby, DC2 is necessary to lock the knee and to immediately release it at touchdown. For this purpose, we use a ratchet mechanism with actuated pawl (Fig. 3.10bb and c). In this mechanism, the pawl passively limits knee extension at a certain angle while knee flexion is possible without limits. The pawl is actuated using a servomotor and when pulled backwards, it allows for full knee extension. Since the leg flexes after touchdown, the knee ratchet mechanism is released automatically and therefore features a "opening time" of 0 ms. The passive opening of DC2 at touchdown avoids additional impact losses which can occur if an actively driven DC2 would open significantly before or after touchdown. This guarantees for high performance and accurate control of the preloaded hopping. Coupling DC1 on the other hand is used to lock the drive of the SEA. To realize that in the ETHOP, we use a ratchet mechanism on the ballscrew (Fig. 3.10bB and c) which allows lengthening of the ballscrew at any time but prevents shortening when the pawl is closed. After the preloading distance is reached during preloaded, the motor controller is switched off for the subsequent stance phase and DC1 is holding the full ballscrew torque. Our coupling-based series elastic knee actuator is able to produce up to 2300 N at a total actuator weight of 4.60 kg (see Tab. 3.2A).

There are some notable features in the ETHOP that introduce discrepancies from the theoretical models. For example, the ETHOP has a segmented leg design which acts as a transmission

Table 3.2: Parameters of the ETHOP Robot

Variable	Dimension	Meaning
<b>(a) Physical Parameters</b>		
$F_{CBSEA,max}$	2300 N	Max output force of the coupling-based series elastic actuator
$M_{CW}$	70 kg	Counterweight mass
$f_{AE}$	1 kHz	Sampling rate of the low level AE controller
$f_{PC}$	30 Hz	Sampling rate of the state machine
$k$	55 400 N/m	SEA spring stiffness
$M_{Leg}$	14.7 kg	Leg mass (3.24 kg leg structure, 4.60 kg knee actuator, 6.86 kg hip motor)
$s_{Leg}$	2.212 m	Beam length to hip joint
$\Delta M$	3.8 kg	Robot mass at foot tip
<b>(b) Calculated Values</b>		
$\underline{c}$	1163 N/m	Leg stiffness (Fig. 3.12b)
$s_{CW}$	0.344 m	Beam length to counterweight
$\Theta$	80 kg m <sup>2</sup>	Robot rotational inertia
$\beta$	0.155	Force ratio between SEA spring and ground reaction force (Fig. 3.12c)
$\gamma$	5.66	Length ratio between SEA and leg length (Fig. 3.12d)

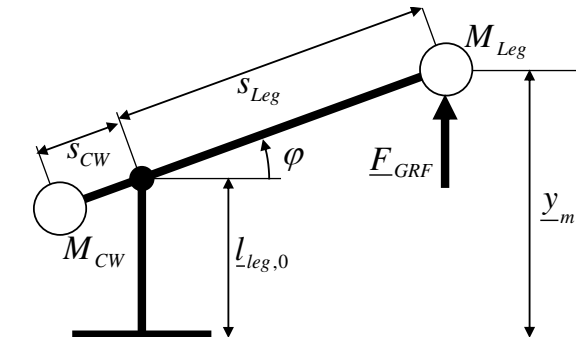
Figure 3.11: Schematic model of the ETHOP robot with leg ( $M_{Leg}$ ,  $s_{Leg}$ ), counterweight ( $M_{CW}$ ,  $s_{CW}$ ), boom, and stance.



Table 3.3: Parameters of the ETHOP Simulation Model

Variable	Dimension	Meaning
<b>(a) Parameters</b>		
$g$	2.27 m/s <sup>2</sup>	Gravitational acceleration
$\tilde{l}_{\text{Leg},0}$	0.992 m	Initial leg length if $\tilde{\dot{l}}_{\text{PU}} \geq 0$
$\tilde{l}_{\text{Leg},0-}$	1.161 m	Initial leg length if $\tilde{\dot{l}}_{\text{PU}} < 0$
$\underline{m}$	16.4 kg	Adapted body mass
<b>(b) Dimensionless Parameters and Limits</b>		
$\tilde{F}_{\text{AE,max}}$	6.03	Maximum AE force for pushup hopping (equals 1450 N on the ballscrew of the CB-SEA)
$\tilde{F}_{\text{S,max}}$	8.73	Max spring force for all hopping schemes (equals 2100 N on the spring of the CB-SEA)
$\tilde{l}_{\text{AE,max}}$	0.195	Max AE length
$\tilde{l}_{\text{AE,min}}$	0	Min AE length
$\underline{\mu}$	0.262	Friction coefficient
<b>(c) Dimensionless Parameters <math>\tilde{\dot{l}}_{\text{PU}} \geq 0</math></b>		
$\tilde{c}$	30.93	Spring stiffness
$\tilde{l}_{\text{AE},0}$	0	AE initial length
$\Delta\tilde{l}_{\text{PR}}$	[0..0.195]	Preloading distance
$\tilde{\dot{l}}_{\text{PU}}$	[0..0.456]	Pushup speed
$\tilde{l}_{\text{S,rest}}$	1	Spring rest length
<b>(d) Changed Dimensionless Parameters if <math>\tilde{\dot{l}}_{\text{PU}} &lt; 0</math></b>		
$\tilde{c}_{\text{Neg}}$	36.23	Spring stiffness for negative pushup
$\tilde{l}_{\text{AE},0,\text{Neg}}$	0.146	AE initial length for negative pushup
$\Delta\tilde{l}_{\text{PR,Neg}}$	0	Preloading distance
$\tilde{\dot{l}}_{\text{PU,Neg}}$	[-0.195..0]	Pushup speed
$\tilde{l}_{\text{S,rest,Neg}}$	0.854	Spring rest length for negative pushup

for the actuator and introduces a non-linear spring behavior of the leg, even though the actuator spring itself is linear. In addition, actuator force and deflection are scaled with respect to the foot tip force and deflection. In order to represent this behavior, we conducted careful parameter tuning of the template, shown in section 3.4.2.

In order to keep the two-segmented leg of the platform always upright, the hip motor actively compensates for the different knee angles during actuation. Due to limitations in its control, this hip motor produces a small negative overall thrust during stance, therefore acting against the knee actuator in propelling the leg. Since this effect was below 2% of the knee actuator energy input for all experiments, we decided to neglect it in the analysis.

The counterweight of the boom reduces the effective gravity of the platform, and therefore lowers the hopping frequency, mainly to give the state-machine controller more time to execute and to prevent the small knee motor from overheating. This lowered gravity is not a fundamental limitation, only an experimental convenience, and can be reproduced in the template too (see Section 3.4.2).

During the stance phase of pushup hopping, the actuator trajectory keeps about 90 ms back its target due to sampling delay in the state machine. The necessary acceleration phase after touchdown is relatively short with values around 50 ms. The constant 90 ms discrepancy becomes relevant at negative or large positive pushup speeds and causes deviations in the hopping height controllability (see Section 3.4.3).

### 3.4.2 Parameter extraction

The ETHOP contains many different kinds of dynamic elements (such as multiple non-rigid bodies, friction, damping, impact, hysteresis, backlash etc.), as well as non-linear effects in all three dimensions. In addition, its boom and counterweight influence the effective gravity and therefore the hopping frequency of the system. However, here we hypothesize that the overall dynamics of ETHOP (mechanical losses, steady state trajectories, hopping performance, and controllability) can be approximated by our one dimensional prismatic template (Fig. 3.1). This section describes how the parameters of this template (see Tab. 3.3) are extracted in order to later simulate the behavior of the physical prototype.

In a first step, we calculate the robot mass  $\underline{m}$  and gravitational acceleration  $\underline{g}$ . Therefore, we approximate the experimental platform by using counterweight  $M_{CW}$ , boom  $s_{Leg}, s_{CW}$  and leg  $M_{Leg}$  (Fig. 3.11). The equation of motion of this planar system during stance phase is

$$\Theta \cdot \ddot{\varphi} + \Delta M \cdot g \cdot s_{Leg} \cdot \cos\varphi = F_{GRF} \cdot s_{Leg} \cdot \cos\varphi, \quad (3.18)$$

with  $\Theta = (M_{Leg} \cdot s_{Leg}^2 + M_{CW} \cdot s_{CW}^2)$  being the robots rotational inertia and  $\Delta M = \frac{M_{CW} \cdot s_{CW} - M_{Leg} \cdot s_{Leg}}{s_{Leg} + s_{CW}}$  being the mass difference between left and right side of the boom joint. The mass difference was measured directly by using a scale and the systems inertia  $\Theta$  was determined from the CAD model of ETHOP. Linearizing around  $\varphi_0 = 0$  with

$$\cos\varphi \approx 1, \quad \sin\varphi \approx \varphi, \quad \underline{y}_m = \varphi \cdot s_{Leg} + \underline{l}_{Leg,0} \quad (3.19)$$

results in

$$\frac{\Theta}{s_{Leg}} \cdot \ddot{\underline{y}}_m - \underline{F}_{GRF} \cdot s_{Leg} + \Delta M \cdot g \cdot s_{Leg} = 0. \quad (3.20)$$

$$\frac{\Theta}{s_{Leg}^2} \cdot \ddot{\underline{y}}_m - \underline{F}_{GRF} + \Delta M \cdot g = 0. \quad (3.21)$$

To fit the model presented in Eq. (3.5), we rewrite Eq. (3.21) as follows:

$$\underline{m} \cdot \ddot{\underline{y}}_m - \underline{F}_{GRF} + \underline{m} \cdot \underline{g} = 0. \quad (3.22)$$

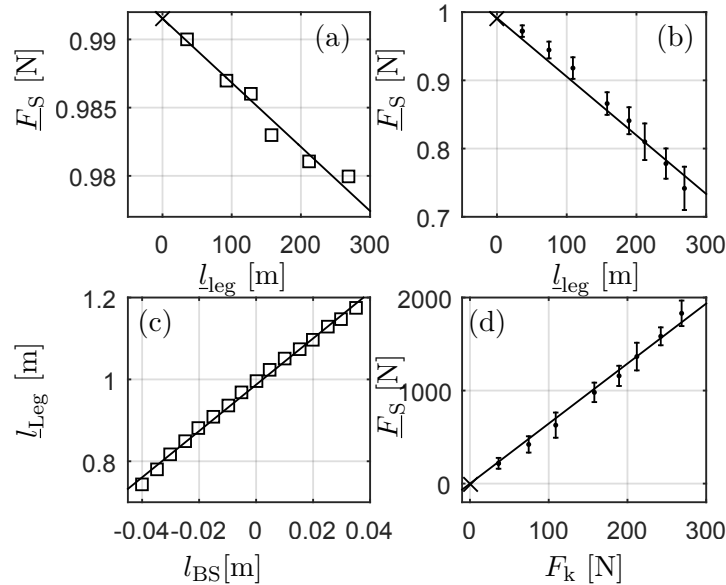


Figure 3.12: Force and length behaviour of the ETHOP leg in physical experiment (dots/squares) and first order least square fit (solid lines). The cross in (a,b,d) represents behaviour at initial leg length. **(a)** Leg length  $l_{Leg}$  with respect to the spring force  $F_S$  during stance with the spring replaced by a rigid tube indicates initial leg length of  $l_{Leg,0} = 0.992$  m. **(b)** Leg length  $l_{Leg}$  with respect to the spring force during stance  $F_S$  with a linearized leg stiffness of  $\underline{c} = F_S/l_{Leg} = 1163$  N/m and  $R^2 = 0.978$ . **(c)** Leg length with respect to the AE length, linearized with  $\gamma = \Delta l_{Leg}/\Delta l_{BS} = 5.66$  and  $R^2 = 0.996$ . **(d)** Force of the SEA spring  $F_k$  with respect to the spring force  $F_S$ , linearized with  $\beta = \Delta F_S/\Delta F_k = 0.155$  with  $R^2 = 0.989$ .

with robot mass

$$\underline{m} = \frac{\Theta}{s_{Leg}^2} = 16.4 \text{ kg} \quad (3.23)$$

and gravitational acceleration

$$\underline{g} = \frac{\Delta m \cdot g}{m} = 2.27 \text{ m/s}^2. \quad (3.24)$$

In a second step, we determine the rest length  $l_{Leg,0}$  of the leg. At ground reaction forces below 20 N, non-linear effects like hysteresis and play of the joint bearings, as well as the masses of upper and lower leg shape the behavior of the physical prototype, which makes it non-trivial to define a rest length of the leg. We solve this problem by replacing the actuator spring with a rigid tube, locking the AE at initial length and measuring leg length and ground reaction force (which is in this case identical to the spring force  $F_S$ ) while adding up to 30 kg mass on top of the platform. Linear least squares fit through the measuring points (Fig. 3.12a) finally leads to an initial leg length of  $l_{Leg,0} = 0.992$  m.

In a third step, we determine the leg stiffness  $\underline{c}$ . Therefore, we repeat the same experiment as described in the second step, but this time with the actuator being equipped with its spring. Since the ETHOP shows hysteresis due to joint friction, we took two different sets of measurements for each added mass. The first set starts from initial leg length slowly shortening to final leg length. The second set starts from below and slowly lengthening to final leg length. Each of the two sets contains three measurements per added mass, so average value and standard deviation for each data point is derived from six measurements in total. From this experiment (Fig. 3.12b), we determine the average leg stiffness as  $\underline{c} = 1163$  N/m.

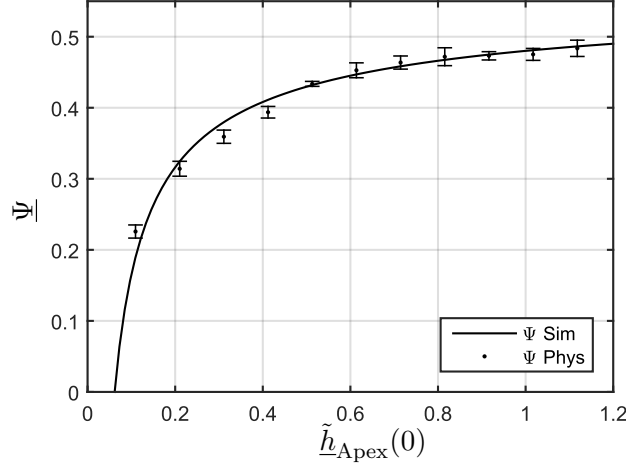


Figure 3.13: Physical and simulated mechanical efficiency  $\underline{\Psi}$  of the ETHOP for different initial apex heights  $\tilde{h}_{\text{Apex}}(0)$ . With  $\underline{\mu} = 0.262$ , the simulation shows best fit with the experimental data, leading to  $\underline{\Psi}_0 = 0.48$ .

In a fourth step, we determine the position ratio by measuring the leg length with the spring replaced by the rigid tube for different AE lengths (Fig. 3.12d) with a load of  $\Delta M = 3.8$  kg. Linear least square fitting shows a position ratio labelled as  $\gamma$  of  $\gamma = \Delta l_{\text{Leg}}/\Delta l_{\text{BS}} = 5.66$ . Similar to the position ratio, out of the data of Fig. 3.12b, we determine the force ratio  $\beta = \frac{\Delta F_{\text{S}}}{\Delta F_{\text{k}}} = 0.155 \approx 1/\gamma$  (Fig. 3.12c).

In a fifth step, we identify the friction coefficient  $\underline{\mu}$  by measuring the mechanical efficiency  $\underline{\Psi}$  of the ETHOP platform by releasing the robot at different heights up to  $\tilde{h}_{\text{Apex}}(0) = 1.1$  (Fig. 3.13). We then fitted the experimental results with the simulation template from Section 3.2, and found that  $\underline{\mu} = 0.262$  shows a reasonable match to the experimental results, leading to a nominal mechanical efficiency  $\underline{\Psi}_0$  of 0.48.

Finally, spring and actuator force limit were determined as  $\underline{F}_{\text{AE,max}} = \beta \cdot F_{\text{BS,max}}$  and  $\underline{F}_{\text{S,max}} = \beta \cdot F_{\text{k,max}}$ . Actuator deflection is determined by  $\Delta l_{\text{Leg}} = \gamma \cdot \Delta l_{\text{BS}}$ . Actuator rest length is set to  $l_{\text{AE},0} = 0$ . Spring rest length finally becomes  $l_{\text{S}} = l_{\text{Leg},0}$ .

For convenience, we define dimensionless parameters for the physical experiment in the same way as described in Section 3.2.2. For preloaded and pushup hopping with positive actuator speed, we use  $l_{\text{Leg},0}$  to normalize the metrics (Tab. 3.3b). For negative pushup hopping, we start from a larger initial length  $l_{\text{Leg},-0}$  to allow the AE to shorten during stance. Therefore, we use this longer leg length (Tab. 3.3c) to normalize the results for negative pushup hopping in Section 3.4.3.

### 3.4.3 Physical hopping experiments

With the physical and the simulation setup established before, we conducted a series of hopping experiments by applying the pushup and preloaded hopping scheme.

#### Trajectory analysis

As in the simulation experiments in Section 3.3, we start with the basic trajectory analysis of the physical platform and its simulation model. Fig. 3.14 shows the time-series trajectories of some of the major variables during the physical experiments with the parameters shown in Tab. 3.3. These physical plots are obtained after some transient phase at the beginning of hopping experiment (the physical hopping dynamics also converge to a steady state after 10 steps or so, similar to Fig. 3.6). In parallel, we conducted simulation experiments with the ETHOP simulation model (Tab. 3.3). The AE input of the simulation is tuned in a way that

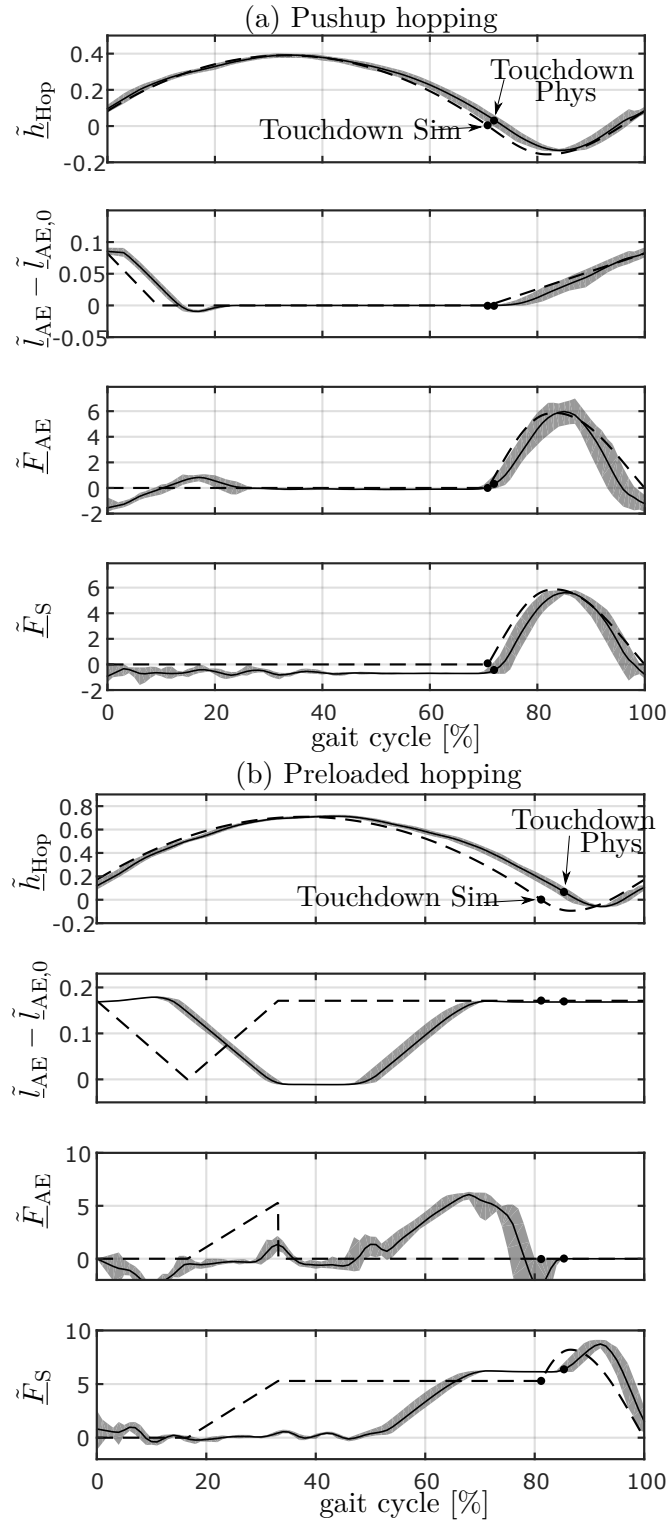


Figure 3.14: Physical (solid) and simulated (dashed) trajectories of steady state hopping with the ETHOP. Minimum and maximum measured parameter values of ten consecutive physical hops are displayed with a gray area around the mean value. (a) Pushup hopping with  $\tilde{l}_{\text{PU,Sim}} = 0.183$ ,  $\tilde{l}_{\text{PU,Phys}} = 0.24$ . (b) Preloaded hopping with  $\Delta\tilde{l}_{\text{PR,Sim}} = 0.171$ ,  $\Delta\tilde{l}_{\text{PR,Phys}} = 0.171$ .

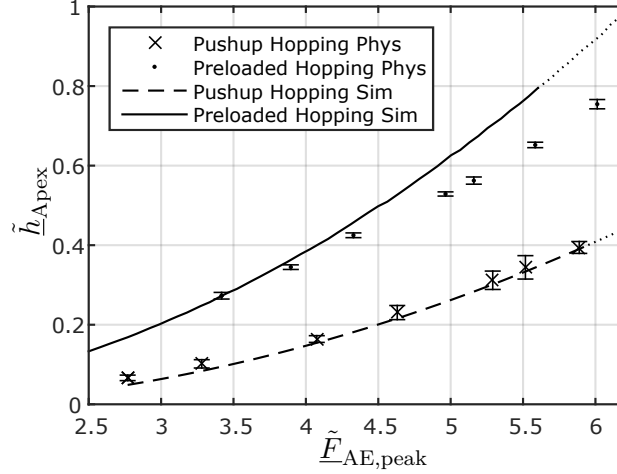


Figure 3.15: Physical and simulated steady state apex height  $\tilde{h}_{\text{Apex}}$  of the ETHOP robot as a function of the peak force of the actuation element AE  $\tilde{F}_{\text{AE,peak}}$ . The mechanical efficiency of the system is around  $\underline{\Psi}_0 = 0.48$ . Dotted lines represent results where either  $\tilde{F}_{\text{AE,max}}$  or  $\tilde{F}_{\text{S,max}}$  is exceeded. Each entry of the physical results is the average of 20 consecutive hops. Errorbars represent two times the standard deviation.

identical hopping heights are reached in simulation and experiment. By using exhaustive search, we determined the control parameters to achieve identical hopping heights are in simulation and experiment. Therefore, the AE inputs for simulation ( $\tilde{l}_{\text{PU,Sim}}, \Delta\tilde{l}_{\text{PR,Sim}}$ ) and physical experiment ( $\tilde{l}_{\text{PU,Phys}}, \Delta\tilde{l}_{\text{PR,Phys}}$ ) are not necessarily identical.

When comparing physical and simulated trajectories with identical apex hopping height, several differences can be observed. For example, the measured duration of the stance phase is significantly shorter for preloaded hopping when compared to the simulation data. This shorter stance phase, whose origins need further investigation, then leads to a higher peak in the spring force during stance. While the preloading distance is identical for simulation and physical experiment, the preloading force is smaller in simulation. The physical leg seems to behave a bit stiffer during preloading than during bouncing on the ground, probably due to non-linear internal transmission in the segmented leg mechanism. For pushup hopping on the other hand, the pushup speed in the simulation is smaller than in the physical experiment. One possible explanation is that the physical actuator needs its larger pushup speed to “compensate” for its acceleration delay after touchdown.

In all experiments the physical leg oscillates after liftoff in both hopping schemes. These oscillations are caused by the lower leg, which acts as a spring mass system together with the actuator spring. This system is excited by the leg extension stopping rapidly at liftoff, which introduces large accelerations to the lower leg. Due to sufficient inner damping, these oscillations fade away before the next touchdown. Another discrepancy can be seen especially in the physical pushup hopping trajectories is a negative AE and spring force. While the upper leg is supported and its effective gravity is reduced, the lower leg mass is pulling downwards with the full earth gravity during flight, which causes the negative force. Finally, while the couplings operate instantly in simulation, they each need about 15% of the step time to do so in the physical prototype, which causes delays after liftoff and before preloading.

The reduction of the duty factor for preloaded hopping, which could be observed in simulation experiments (see Fig. 3.4) was also confirmed by the physical experiments, which show an even larger reduction.

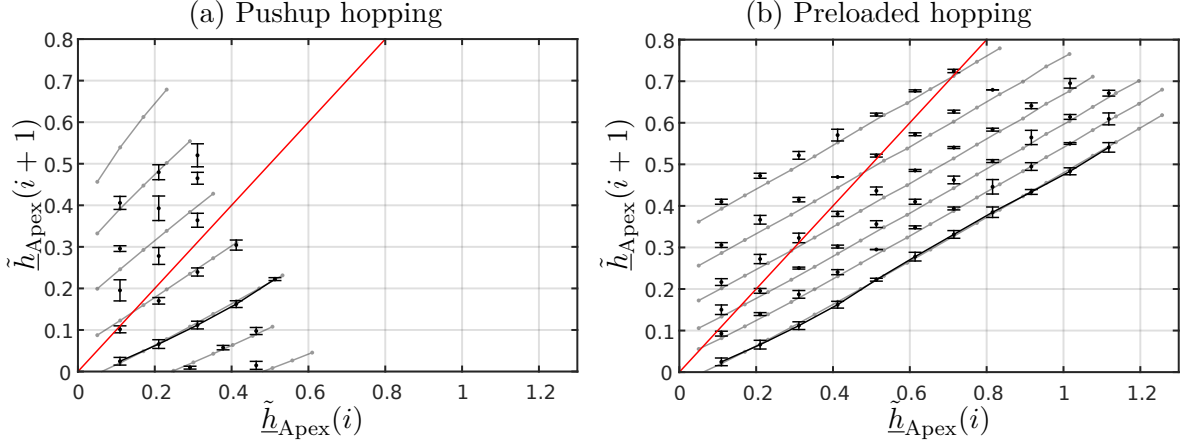


Figure 3.16: Physical (dots) and simulated (grey solid) first return maps for pushup and preloaded hopping for different initial apex heights  $\tilde{h}_{\text{Apex}}(i)$ . Physical results with zero actuation are connected with a black solid line. All limits are set according to Tab. 3.3. Each physical entry is the average of five trials from identical hopping height. Error bars represent two times the standard deviation over trials.

### Hopping height with limited actuator peak force

In the next set of experiments, we investigate the correlation between the steady state apex height  $\tilde{h}_{\text{Apex}}$  and the peak output force of the actuation element  $\tilde{F}_{\text{AE,peak}}$ , to test the feasibility of the simulation analysis in Section 3.3.3. For testing the pushup hopping scheme, we applied a set of different pushup speeds of the electric motor during the stance phases, and identified the corresponding peak actuator forces in the cycles. And for the preloaded hopping scheme, we set the different spring deflection during the preloading in flight phases, where the peak compression force then equals the peak AE force. In parallel to the measurements, we repeated the simulation shown in Section 3.3.3 with the parameter set of the ETHOP simulation model (see Tab. 3.3).

As predicted in Section 3.3.3, preloaded hopping allows the physical platform to reach a significantly higher hopping height with limited actuator force too, namely a 89% increase at maximum AE force.

In the case of pushup hopping, the simulation using the ETHOP parameters represents the basic behavior with an average deviation of  $0.01 \cdot L_{\text{Leg},0}$  (Fig. 3.15), nearly independent from hopping height. For preloaded hopping, the simulation overestimates the physical hopping height by  $0.08 \cdot L_{\text{Leg},0}$  in average. The overestimation at large  $\tilde{F}_{\text{AE,peak}}$  can be seen in the trajectories as well, where the necessary preloading force for the same apex hopping height is lower in simulation compared to the physical prototype.

In addition, the simulation is also able to predict the possible apex hopping height at maximum AE force  $F_{\text{AE,max}}$ . The estimation for pushup hopping is precise, while preloaded hopping is overestimated by about  $0.05 \cdot L_{\text{Leg},0}$ .

### Hopping height controllability

To confirm the hopping height controllability (as analyzed in Section 3.3.5 and displayed in Fig. 3.9), we measured the achievable apex height  $\tilde{h}_{\text{Apex}}(i+1)$  from different initial apex heights  $\tilde{h}_{\text{Apex}}(i) \in [0.11..1.12]$  for pushup and preloaded hopping using the following control parameters:

$$\tilde{l}_{\text{PU}} = [-0.195, -0.097, 0, 0.098, 0.196, 0.293, 0.456], \quad (3.25)$$

$$\Delta \tilde{l}_{\text{PR}} = [0, 0.049, 0.073, 0.098, 0.122, 0.147]. \quad (3.26)$$

For pushup hopping with negative speed, we set the AE initial length to  $\tilde{l}_{AE,0,Neg} = 0.146$ , to allow the AE to shorten during stance. Therefore, actuator input and results for negative pushup speed are normalized with the resulting longer initial leg length (Tab 3.3d). For positive pushup and preloaded hopping, results are normalized with  $\tilde{l}_{AE,0} = 0$  as usual (Tab 3.3c). Again, we ran a simulation with the ETHOP parameters (Tab. 3.3) in parallel.

Fig. 3.16 displays the results of these physical and simulation experiments. Physical measurements are represented by black dots, simulation results with grey lines. The physical measurements at zero actuator input for both pushup and preloaded hopping are connected with a black line. As predicted, the experimental results show that the preloaded hopping scheme can exhibit significantly better performance with a steady state hopping height of  $\tilde{h}_{Apex}(i) = 0.72$  compared to  $\tilde{h}_{Apex}(i) = 0.38$  for pushup hopping.

For pushup hopping, the simulation is able to predict the physical data for  $\tilde{l}_{PU} = [-0.097, 0, 0.098]$ . For higher pushup speeds, the simulation is overestimating the physical hopping height. This discrepancy is caused by the physical actuator which, in contrast to the simulation, does not accelerate instantly (see Fig. 3.14a). On the other hand, the simulation is able to predict the maximum possible increase/decrease in hopping height precisely.

For preloaded hopping, the simulation precisely predicts the gradient for each preloading distance and only slightly underestimates the achievable increase/decrease in hopping height per preloading distance  $\Delta l_{PR}$ . As already shown in Fig 3.15 for steady state hopping, the simulation also overestimates the achievable increase/decrease in hopping height at maximum actuator force.

### 3.5 Discussion

This paper established a template for coupling-based series elastic actuation and demonstrated in simulation and physical experiment how discrete couplings can enhance the dynamics of series elastic actuation in hopping robots. In addition, the prismatic template presented in the simulation section is able to approximate basic behaviour of the much more complex physical platform ETHOP. This includes the benefit of larger actuator peak force, which could be increased in our physical platform by 45 % by making use of couplings.

However, adding discrete couplings leads to two additional degrees of freedom per actuator, increased mechanical, electrical and control complexity as well as additional weight. In order to put the actuator's performance in context, it is necessary to consider the weight of our actuator and compare it to the weight of an already established concept. Since our actuator already contains a series elastic actuation element, it makes sense to establish a comparison between our coupling-based series elastic actuator and a conventional series elastic actuator. Since the ETHOP and its knee actuator are modular laboratory platforms, they contain various functional groups with different maximum loads. In addition, some components can fulfil additional tasks in other experiments, which increases their size and weight. In order to enable a comparison, it is therefore essential to carefully scale these functional groups, both the clutches and the series elastic actuation elements. For scaling, we use the following two strategies: First, we replace multi-functional components with components specialized for the compared task. And second, perform a weight scaling based on [133], by using a linear connection between peak force and component mass.

Our clutch actuator in the physical coupling-based series elastic actuator is a multi-functional component, strong enough to directly drive friction clutches for other experiments (see [2]). Since the pawl actuation of the scaled clutches can be done with the low torque of two micro servos (2 · 0.015 kg) instead of the actual pawl motor, for the calculation we use the weight of the servos instead of the clutch actuator weight.

The drivetrain (motor, ballscrew and guide system) is designed for a peak force output of 2300 N at 1.5 kg. The knee ratchet mechanism is designed for 1500 N at 0.2 kg. The ballscrew



ratchet mechanism is designed for 2.5 N m ballscrew torque at 0.018 kg, resulting in 196 N force at the pawl. As a result of the scaling, for pushup hopping, the scaled drivetrain for  $F_{BS,max} = 2100$  N instead of 1450 N would become 45 % or 0.415 kg heavier. For preloaded hopping, the scaled drivetrain ( $F_{BS,max} = 1450$  N) plus the scaled ratchet mechanisms plus the two micro-servos (see paragraph above) would become 44 % or 0.410 kg heavier. From this analysis, one can see that the ratchet mechanisms can provide increased actuator force at similar additional mass than an enlarged actuator.

In this chapter, we investigated always only one hopping scheme per simulation or physical run. However, since all hopping schemes presented in this chapter are performed on one and the same actuator, and switching between them would be possible between single hops, an advanced controller can choose the suitable scheme on the fly from hop to hop. As an example, starting with pushup hopping for covering distance, then switching to preloaded hopping to jump on a high obstacle, and then switching to DC-pushup hopping to jump back on the ground.

In addition of enhancing actuator dynamics, simulation and real world data indicate that discrete couplings enable the series elastic actuator to vary the effective stiffness of its spring. As shown in Fig. 3.4 and 3.14, the stance phase of preloaded hopping is significantly shorter compared to pushup hopping, which comes along with increased ground reaction force. This behavior can be interpreted as increased leg stiffness. This observation is supported by the fact that spring preloading is a common strategy in variable stiffness actuators [78]. Since variable stiffness is desirable for running over a wide range of forward speeds [29, 49], further research on preloaded hopping towards this goal may be beneficial.

Another important aspect of the proposed approach is the energy consumption and the energy efficiency, even though we have not explicitly addressed this issue so far. The model presented in this chapter features a lossless actuation element and the discrete couplings need no energy to open and close as well. Therefore all three control strategies are nearly equal in energy efficiency. However, with a physical actuator and physical clutches, [125] indicates that a clutch in parallel to the actuation element AE of a series elastic actuator can improve the energy efficiency of the system. In addition, during the flight phase of preloaded hopping for example, particular speed and acceleration of the preloading motion have no effect on the subsequent stance phase, as long as the preloading distance is reached before touchdown. Therefore, the motor can adjust acceleration and speed of the preloading motion to achieve optimal energy efficiency. After evaluating peak actuator force in this paper, energetic efficiency of coupling-based series elastic actuation in comparison to other robotic actuation approaches would be a logical step for future investigations.

Different robotic platforms come with a wide range of different losses, for example damping, friction, or impact. Out of Fig. 3.15 and 3.17, we reason that our ETHOP platform is mainly friction driven. While the friction model can describe both pushup and preloaded hopping with less than 0.08 leg lengths deviation in average (see Section 3.4.3), damping and impact models tend to overestimate the preloaded hopping height with up to 0.29 leg lengths average deviation (see Appendix 3.7). Certainly it needs to be clarified if this is a characteristic of only our system, or if friction losses are in general more suitable to describe preloaded hopping. Nevertheless, Fig. 3.15 and 3.17 show that, at least in simulation, coupling-based series elastic actuation shows better performance independent from the specific choice of the loss model. Therefore, we are confident that CB-SEA will also be beneficial for damping or impact driven systems.

The next step in exploring coupling-based series elastic actuation would be to extend our simulation and physical experiments to forward hopping. Since [124] already demonstrated forward hopping by using preloaded hopping on a parallel mechanism, we are very confident that the same will work too for preloaded hopping on our serial mechanism. And by considering the fact that the Raibert's three-part controller already took advantage of preloading in their pneumatic actuators [134] (by preloading compressed air to the lower chamber of the pneumatic cylinder during flight phases) for achieving one-, two-, and four-legged robots with various stable

gait patterns [37], we are optimistic to be able to extend our approach to more general forms of legged locomotion.

For basic investigation, we demonstrated coupling-based series elastic actuation based on a state machine with predefined trajectories for each state, but without the use of any feedback control. This approach became possible since the passive dynamics of the system seem to stabilize this system within the parameter range we used. For a deeper understanding of the systems passivity, in depth investigations will become necessary. In addition, we believe that adding feedback control could greatly improve the performance of coupling-based series elastic actuation, especially in unstructured terrain. Preloaded hopping for example is a good option to implement energy based control methods as in [84] and future investigations in this directions would be beneficial.

With our physical prototype, we were able to demonstrate conventional and coupling-based actuation by performing pushup and preloaded hopping, respectively. However, our simulation template indicates additional actuation strategies, for example DC pushup hopping, whose physical realization with highly dynamic actuator-coupling pairings would be an important step towards further exploration of couplings in legged robot actuation.

In this paper, we realized the discrete couplings by using ratchet mechanisms which feature short switching times and high load but allow only unidirectional operation at a limited amount of joint angles. But for the sake of flexibility, continuous adjustment of the joint angle at which the coupling closes as well as bidirectional behaviour (coupling locks the joint in both directions) would be desirable. For the future of coupling-based actuation, the development of bidirectional, reliable, fast and light weight high-load couplings is crucial.

### 3.6 Conclusion

This chapter investigates three types of actuation dynamics for monopod hopping robots equipped with coupling-based series elastic actuation (CB-SEA). By introducing discrete couplings in the conventional series elastic actuation, we found that hopping performance such as maximum hopping height under the limitation of maximum actuation forces can be significantly improved (up to 89% in physical experiments, up to 179% in simulation), and that these improvements increase with better mechanical efficiency in the passive leg structures. The use of discrete couplings was also found to be effective to enhance the hopping height controllability, i.e. varying between large differences in hopping height every step. Finally, discrete couplings allow for variation of stance phase duration by preloading the spring, and during flight phase actuation, motor trajectories for preloading the spring can be optimized without influencing the robots overall dynamics.

These basic findings, together with the asymptotic stability of the system during state-machine based reflex control, are confirmed both in simulation and physical experiments. In the physical prototype, the ratchet mechanisms representing the discrete couplings are not heavier than a larger SEA capable of producing the same peak forces than the CB-SEA. Therefore, coupling-based series elastic actuation can introduce more variable actuation dynamics, including variable stiffness actuation and the potential for increasing actuator efficiency, by adding additional mechanical, electrical and control complexity, but without additional weight compared to a standard SEA.

### 3.7 Simulation results for damping and impact losses

This Appendix repeats the simulations shown in Section 3.3.3 for the model presented in Section 3.2, but with damping and impact losses instead of friction.

Damping losses are simulated by replacing the friction element FE (Fig. 3.1) with a damping element  $d \geq 0$ . The damping force during stance is proportional the mass speed  $\dot{y}_m$  and becomes

zero during flight:

$$\text{Stance: } F_d = -\dot{y}_m \cdot d, \quad \text{Flight: } F_d = 0. \quad (3.27)$$

While touchdown is defined according to Eq. (3.3), liftoff occurs when the spring force equals the damping force:

$$F_S + F_d = 0, \quad \dot{y}_m > 0, \quad (3.28)$$

and after liftoff, the spring is assumed to shorten to rest length instantly.

The model for impact losses bases on Fig. 3.1 but with the friction element FE removed. Touchdown and liftoff are defined according to Eq. (3.3) and (3.2). Impact loss occurs at touchdown, where the kinetic energy  $E_{\text{kin}}$  of the mass  $m$  is reduced instantaneously with the impact factor  $\epsilon \leq 1$

$$E_{\text{kin,TD}}^- = \frac{1}{2}m(\dot{y}_{\text{TD}}^-)^2, \quad E_{\text{kin,TD}}^+ = \epsilon \frac{1}{2}m(\dot{y}_{\text{TD}}^-)^2 = \frac{1}{2}m(\dot{y}_{\text{TD}}^+)^2 \quad (3.29)$$

with indices  $-$  labelling pre-touchdown and  $+$  post-touchdown events. Out of Eq.(3.29), the post-impact velocity is determined as

$$\dot{y}_{\text{TD}}^+ = \sqrt{\epsilon} \dot{y}_{\text{TD}}^-. \quad (3.30)$$

To determine the hopping performance with limited actuator peak force, we conducted simulations in the same way as described in Section 3.4.3 in the chapter. For convenience, we use dimensionless values as described in Section 3.4.2, with dimensionless damping coefficient  $\tilde{d} = d \cdot \frac{1}{2\sqrt{m \cdot c}}$  and impact factor  $\tilde{\epsilon} = \epsilon$ . The results are summed up in Fig. 3.17, showing that both impact and damping model overestimate the possible hopping height during preloaded hopping significantly, when compared to the physical data.

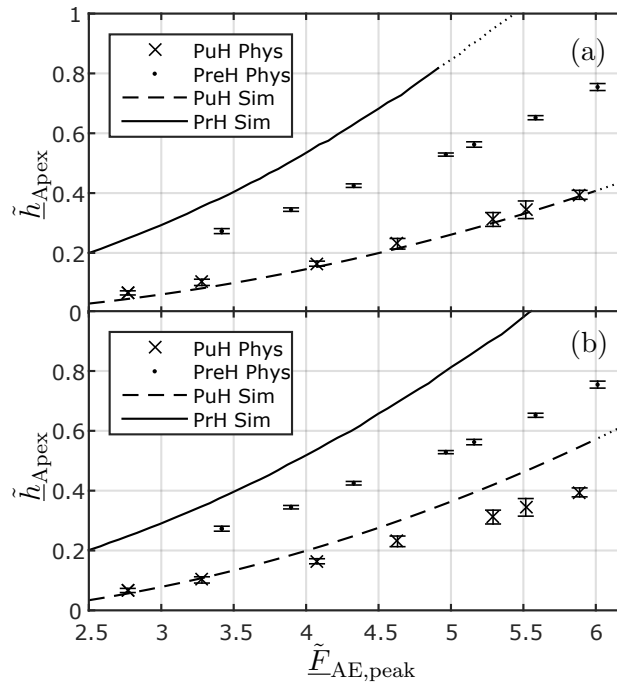


Figure 3.17: Physical and simulated steady state apex height  $\tilde{h}_{\text{Apex}}$  of the ETHOP robot as a function of the peak force of the actuation element AE  $\tilde{F}_{\text{AE,peak}}$ . The mechanical efficiency of the system is around  $\underline{\Psi}_0 = 0.48$ . Dotted lines represent results where either  $\tilde{F}_{\text{AE,max}}$  or  $\tilde{F}_{\text{S,max}}$  is exceeded. Each entry of the physical results is the average of 20 consecutive hops. Errorbars represent two times the standard deviation. (a) Model with damping losses  $\tilde{d} = 0.101$ . (b) Model with impact losses  $\underline{\epsilon} = 0.48$ .



## Chapter 4

# Parallel elasticity for robust and versatile monopod running<sup>1</sup>

In the previous two chapters, we demonstrated how couplings can add additional dynamics to a conventional series elastic actuator, by allowing for additional modes to make use of its spring. Some of these modes can be used to increase the actuator force output (preloading), while others are able to overcome the shortcomings of the initial actuator concept, for example by offering direct actuation instead of SEA for precise manipulation.

Such a coupling-extended SEA can be implemented in a very general robotic leg structure, as demonstrated by the ETHOP robot in the previous chapter. “General” thereby means that the leg structure itself does not introduce strong passive dynamics, for example by containing rigid, lightweight leg segments with no springy behavior and low inertia. The overall behavior of such a robotic leg will therefore be shaped mainly by its actuators, and depending on their configuration, coupling-extended SEA’s allow a general robotic leg structure to become a “specialist” in many different disciplines.

In order to release the full potential of coupling based multi-dynamic actuation, an in-depth understanding of the available dynamics is necessary. Although each dynamic could be investigated by generating it with a multi-dynamic actuator, in many cases it is beneficial to first create a specialist platform which is able to generate only this dynamic. Such a specialist platform allows to avoid many of the compromises in terms of mechanics, actuation, sensing and control, which occur naturally if a platform would need to generate multiple dynamics. Instead, a specialist platform can focus exclusively on its single dynamic, which allows for maximum performance and eliminates disturbances from inactive components, which would occur by using a multi-dynamic actuator. Once basic investigations on this specialist platform are done, the gained knowledge can be used to integrate the dynamic into a multi-dynamic actuator.

Series elastic [39,41], passive springy [35] and preloading dynamics [34] have been investigated in the past by using specialist platforms. Therefore, this dissertation applies the specialist approach to a less considered dynamic, namely the parallel elastic actuation, by introducing a family of robots which we call parallel elastic runners. They are optimized for only one task, namely forward running on level ground. As their name suggests, in contrast to the series elastic actuation of the previous chapters, these runners make use of parallel elastic actuation (PEA),

---

<sup>1</sup>This chapter presents the collaborative project with my colleague F. Giardina under the guidance of my supervisor F. Iida. I contributed to the design of the physical platform and the physical experiments, the analysis of simulation and physical results and the writing of the manuscript. My colleague F. Giardina designed the physical platform, conducted the simulation and physical experiments and contributed to the discussion and the writing of the manuscript, together with my supervisor F. Iida. This chapter has been edited and adapted from the following publication:

- F. Günther, F. Giardina, and F. Iida. Self-stable one-legged hopping using a curved foot. In *Proc. 2014 IEEE Int. Conf. Robotics and Automation (ICRA)*, pages 5133–5138, Hong Kong, China, 2014

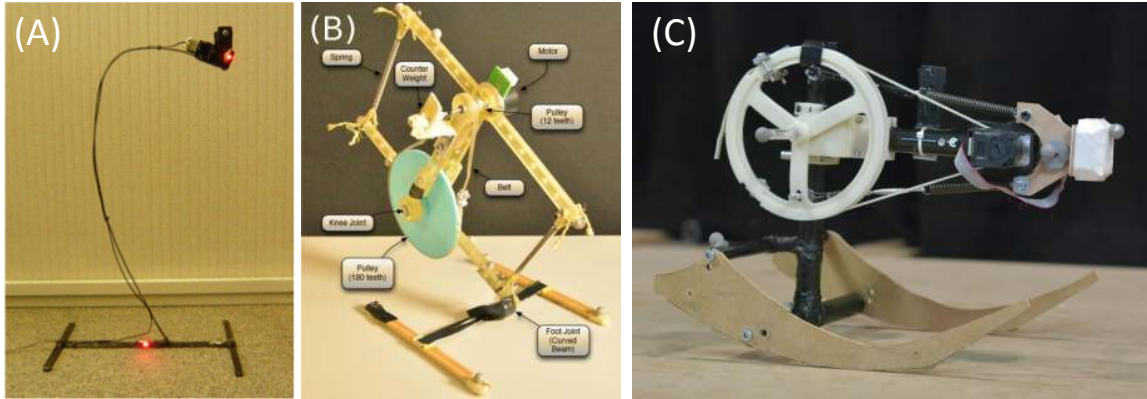


Figure 4.1: Three generations of parallel elastic runners built at our lab. **A** Curved beam hopper with unsprung mass drive. **B** Three body hopper with parallel hip drive. **C** Curved foot runner CHIARO.

where an actuation element acts in parallel to the spring around a joint. This gives the joint a defined rest length (or rest angle), and every deviation from this rest angle induces a counter-moment of the spring. This counter moment can be exploited in multiple ways, ranging from increased robustness up to payload support and safe operation, since the robot keeps its posture even when the actuation element is shut down completely.

When standing on the ground and swinging passively, these parallel elastic runners show a distinctive resonance frequency. When actuated at this resonance frequency, forward running very low actuator input becomes possible. The first generation of parallel elastic runners built in our lab (Fig. 4.1A) contains a curved beam which acts as a springy leg. For actuation, a rotating unsprung mass driven by an electric motor was used [72, 135, 136]. This minimalist design showed good energy efficiency and was able to self-stabilize forward speed depending on the actuator input. Driven by the need to model these robots for simulation, the second generation was an approximation of these curved beam robots using three rigid bodies and two spring loaded joints (Fig. 4.1B). The hip joint was actuated using a motor and a drive belt, while the ankle joint was passive. This robot allowed for efficient implementation in simulation and showed similar motion patterns than the curved beam hoppers [137].

This chapter introduces CHIARO, which was the first agent of our actual generation, containing only two rigid bodies, a spring loaded joint and a curved foot. With CHIARO, we systematically explored the interconnections between geometry, speed and energy efficiency of parallel elastic running.

## 4.1 Introduction

The musculoskeletal body plan of legged animals combines both efficiency and high versatility. The small size of a single body cell compared to the overall structure results in a high total number of these basic functional units. Therewith optimized lightweight and versatile components of high complexity can be realized. Accordingly most of today's versatile legged robots have also a high grade of complexity to be able to solve their tasks, even if the functional range is small compared to biological systems. But for machines in general, high complexity leads to high design, manufacturing and operational effort and the high number of moving parts lowers the overall efficiency due to mechanical interaction. In addition, the high number of parameters complicates a proper system analysis or makes it even impossible. On the other side of the spectrum, simple and/or efficient robots suffer from a narrow range of flexibility and are mostly constrained to flat ground.

Considering efficiency, versatility and complexity for legged robot locomotion, three groups

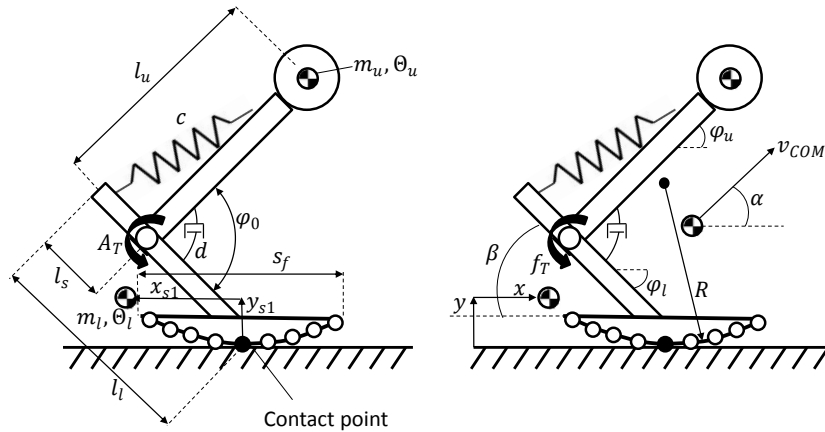


Figure 4.2: Illustration of the physical model used for the simulations. It consists of two rigid bodies (lower and upper leg), which are connected with a spring loaded and damped rotational joint. On the joint, a parallel motor torque is applied. The lower leg is attached to a curved foot which establishes ground contact during stance phase. The foot is discretized by placing 10 contact points uniformly on the outer arc of the foot. During rolling motion in stance either one or two contact points establish ground contact.

of robots can be distinguished. On the side of the efficient locomotors as the first group, today's actuated passive dynamic walkers are able to achieve bipedal walking at the same level of animal's energy efficiency [57]. By optimizing the robot for a certain operational area, the combination of high performance and high efficiency is possible [46]. Although an adaption to different slopes is possible, these robots are restricted to relatively uniform ground and their mechanism shows a high grade of complexity. By taking advantage of free vibration, curved beam hoppers [138] are able to achieve similar efficiency with clearly reduced complexity. The second group covers high versatile robots designed on the one hand as flexible test and demonstration platforms [139] or for specific mission profiles like transportation in rough terrain [140] or testing of human equipment [141]. Complexity and efficiency are of minor matter. The third group contains robots that are efficient, versatile and simple at the same time. By including electric motors and series elasticity, versatile robots were made more efficient [122]. By adding extra features like walking in circles, efficient robots were made more versatile [56]. By combining the mechanics of wheeled robots with compliant legs, complexity of legged robots was reduced [35].

As a contribution to this third group of robots, we combined the simple mechanics of a two segmented one legged hopper with a curved foot. This approach minimizes the number of parameters which simplifies the analysis. The goal of this chapter is to show that this set up can guarantee stable hopping gaits over a wide range of parameters while achieving a good overall efficiency. Further we introduce some first parameter connections to tune the robots forward speed and efficiency.

We structure the rest of the chapter as follows. Section 4.2 describes the basic design and physical modeling of the robot. The simulation set up is explained in Section 4.3 while Section 4.4 presents simulation results on stability, efficiency and parameter interaction. Section 4.5 describes a series of physical experiments to confirm the simulation results and Section 4.6 concludes the chapter with some remarks on future work.

## 4.2 Design and modeling

To explore the behavior of a curved foot on a one legged hopping robot, we started with a simulation to establish the basic characteristics and to find suitable sets of parameters. In parallel, we developed the CAD model of the physical platform to guarantee a good grade of



accordance with the simulation.

### 4.2.1 Simulation model

The planar robot model we use is shown in Fig. 4.2. It consists of two rigid bodies, a foot and an upper part. The bodies are connected with a rotational joint on which a linear push/pull spring is attached. Joint friction is modeled by linear rotational damping in the joint. A curved foot is attached to the lower leg to ensure ground contact during stance phase. On the joint, a parallel motor torque is applied. Note that the motor inertia is neglected.

### 4.2.2 Parameters

As a starting point, the motor (a Maxon EC45-flat with 70 W and a total weight of 141 g) and the robot size (around 0.3 m height) was given. From the conceptual side, the drive belt gear with ratio 1:12.75, the two segmented body and the curved foot was set. To reduce the number of parameters, we decided to constrain the system. First, The curved foot is designed as a circle segment with constant radius. Second, the motor is placed on top of the upper body on the same point where the push-pull spring is attached. Due to the fact that motor and motor plate represent the majority of the upper body mass, we assumed that the center of mass of the upper body coincides with the motor position. Fourth, the lower leg is attached to the middle of the curved foot. Finally, the motor torque input is constant during the run is sinusoidal

$$T_t(t) = r \cdot \sin(\omega_T \cdot t)$$

with  $\omega_T = f_T \cdot 2\pi$ . This leads to the given set of 17 parameters shown in Tab. 4.1. Due to mechanical design issues (see Section 4.5.1), we chose the frequency  $f_T$ , the foot radius  $R$  and the lower leg angle  $\beta$  to be our tuning parameters. The remaining parameters were set as constant based on first simulations where some suitable parameter sets were established.

### 4.2.3 Control strategy

The simulation model, as well as the physical platform, are feed forward controlled without any sensory feedback. All stabilization pitching motion is achieved by exploiting the intrinsic dynamics of the mechanical structure. The stabilization around the x-axis of the physical platform is achieved mechanically using two foot plates with a distance of 0.2 m in z-direction.

### 4.2.4 Hopping pattern

At touchdown, the robot touches the ground with the curved part of the foot. During stance phase, the foot is rolling forward and the knee first bends and then flexes. At take-off, the foot stands either on the curved area or on the front foot tip, depending on the parameter set for the run. During flight phase, the knee bends again while the hopper swings back to its landing position.

## 4.3 Simulation setup

### 4.3.1 Ground contact model

Due to ground contact interactions, namely friction- and impact forces, the robot shows properties of a non-smooth mechanical system. The equations of motion for our system are depending on the minimal coordinates

$$\vec{q} = (x \ y \ \varphi_l \ \varphi_u)^T$$

Table 4.1: Parameters and Variables of the robot model used for simulations

<b>Fixed Parameters</b>		
<b>Letter</b>	<b>Name</b>	<b>Value and Unit</b>
$c$	Spring stiffness	3022 N/m
$d$	Damping coefficient	0.06 N m s
$l_l$	Lower body length	0.2 m
$l_u$	Upper body length	0.16 m
$l_s$	Moment arm spring	0.05 m
$m_l$	Lower body mass	0.239 kg
$m_u$	Upper body mass	0.481 kg
$A_T$	Motor torque amplitude	0.5 N m
$s_f$	Foot length	0.2 m
$x_{s1}$	Horizontal coordinate of lower leg center of mass	-0.063 m
$y_{s1}$	Vertical coordinate of lower leg center of mass	0.045 m
$\theta_l$	Lower body inertia	0.0015 kg m <sup>2</sup>
$\theta_u$	Upper body inertia	0.0016 kg m <sup>2</sup>
$\varphi_0$	Initial Knee angle for relaxed spring	0.7853 rad
<b>Tunable Parameters</b>		
$f_T$	Motor torque angular frequency	2–6 Hz
$R$	Foot Radius	0.2–0.6 m
$\beta$	Lower leg angle	0.4–1.2 rad
<b>Variables</b>		
$x(t)$	Position x-value of lower leg COM	m
$y(t)$	Position y-value of lower leg COM	m
$\varphi_l(t)$	Lower leg angle	rad
$\varphi_u(t)$	Upper leg angle	rad
<b>Computed Variables</b>		
$T_M(t)$	Motor moment function	N m
$\alpha(t)$	Take off angle of lower leg	rad
$\varphi(t)$	Knee angle	rad
$\omega_T(t)$	Motor torque angular velocity	rad/s

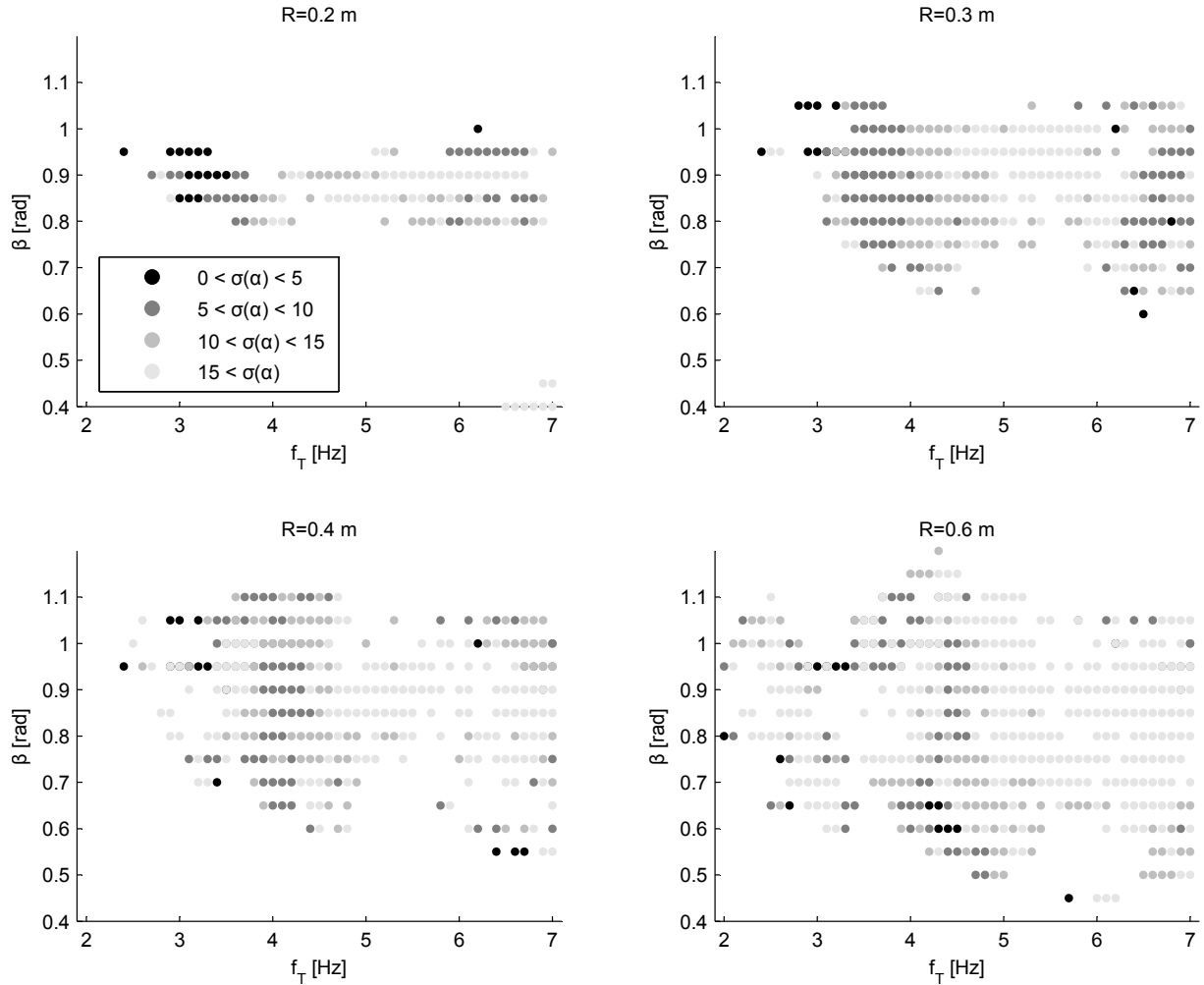


Figure 4.3: Standard deviation plots of  $\alpha$  from simulation data as a function of motor frequency  $f_T$  and lower leg angle  $\beta$  for different foot radii  $R$ . For all radii, the whole frequency and angle range was simulated. Each dot indicates a successful run, which means not falling down during the runtime of 5 s. White areas imply unsuccessful runs. Every run starts from static rest position. Amplitude and frequency were hold constant during each run.

The mathematical equations of motion of our system

$$\mathbf{M} \ddot{\mathbf{q}}(\mathbf{q}, t) - \mathbf{h}(\mathbf{q}, \dot{\mathbf{q}}, t) = 0,$$

can be extended by the contact forces as proposed in [142]. This leads to the following measure equality for a dynamical system

$$\mathbf{M} d\mathbf{u} - \mathbf{h} dt - d\mathbf{R} = 0,$$

where  $\mathbf{M}$  is the mass matrix,  $\mathbf{u}$  is the velocity of the system in minimal coordinates,  $\mathbf{h}$  are the gyroscopic accelerations as well as smooth, generalized forces and  $d\mathbf{R}$  is the measure of the contact forces. By defining force laws for  $d\mathbf{R}$ , which depend on the system's kinematic states, it is possible to set up an optimization problem (linear complementarity problem) for our contact forces. In our case, we assumed a newtonian impact behavior, which has the form

$$v_N^+ = -\varepsilon_N v_N^-, v_T^+ = -\varepsilon_T v_T^-,$$

where  $v_N^+$  is the normal velocity of the colliding body just before impact,  $\varepsilon_N$  is the restitution factor in normal direction and  $v_N^-$  is the velocity of the colliding body right after the impact. The same holds for the tangential direction to the contact, which is labeled with the subscript  $T$ . In our simulation model, we assumed that the restitution number in normal and tangential direction is equal to zero, as no energy should be recovered from the unsprung mass. For the forces in tangential direction, we assumed a coulomb friction model with equal static and dynamic friction coefficient. Once the solution of the optimization problem is found, we can reenter the contact forces in Eq. 4.3.1 and integrate normally.

With this method, it is not necessary to switch the basic differential equations between ground phase and flight phase, as the properties of our system are altered by Lagrangian multipliers.

For our robot, we implemented a time stepping algorithm in order to solve the described system numerically. The curved foot was discretized by placing multiple contact points uniformly on the outer arc of the foot. Claiming that maximally two contact points of the convex foot can be touching the flat ground simultaneously, the numerical effort to solve the optimization problem is manageable and can be executed with a reasonable performance using an enumerative method.

### 4.3.2 Simulation environment

The crucial parameters for the ground interaction are the friction coefficients and the normal- and tangential restitution factors, respectively. As for the first, we assumed a friction coefficient of 0.3 throughout the simulation for all contact points. For the restitution factors, we chose all to be equal to zero for all contact points, which corresponds to a complete dissipation of kinetic energy of the unsprung mass at impact.

For each simulation, the initial conditions were precalculated in order to start from the robot's static equilibrium position. As a consequence, the same initial conditions as for the physical experiment could be guaranteed. However, static stability became a necessary condition for a successful run.

As the simulation requires that maximally two contact points are touching the ground, the integration time step  $\Delta t$  has to be chosen sufficiently small, such that the foot does not immerse in the ground. This problem occurred primarily when a low curvature of the foot arc and a high number of contact points were chosen. We limited the contact point number to  $n = 10$  to overcome this problem instead of increasing the integration step number. With set  $\Delta t = 0.0005$  s, the simulations showed only insignificant changes of the results when fewer contact points were applied to the foot.

## 4.4 Simulation results

We performed several simulations to test both stability and efficiency of the curved foot hopper concept. The parameters  $f_T, R, \beta$  were varied between the runs (see Section 4.2), the other parameters were kept constant. Due to the fact that the system is highly non-linear and good stability measures are not easily found, we used the following stability indicators:

1. Every set of parameters that guarantees a run of 5 s accelerating from deadlock without falling down we call successful.
2. We use the standard deviation of the take-off angle  $\alpha$  as an indicator for the system stability. The lower the standard deviation, the better the system stability.

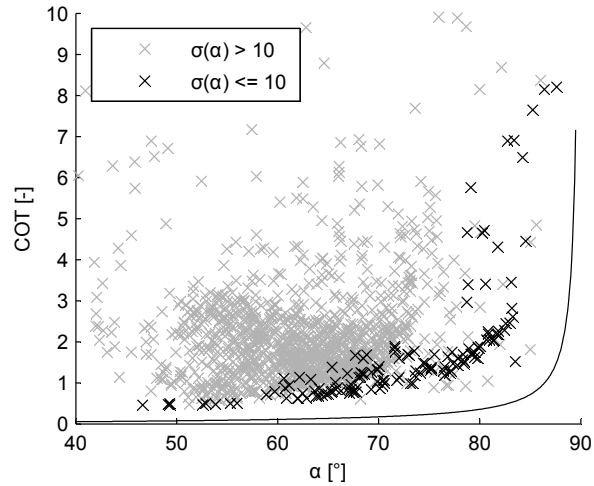


Figure 4.4: Simulated cost of transport as a function of the take-off angle  $\alpha$  of the lower leg. The continuous black line indicates the minimum cost of transport possible for a hopping mass with coefficient of impact  $\epsilon = 0.5$ . The parameter set used was the same used for Fig. 4.3. The lowest cost of transport is  $0.458$  with  $f_T = 2.9\text{Hz}$ ,  $R = 0 : 3\text{m}$ ,  $\beta = 1 : 05\text{rad}$ . Runs with  $\sigma(\alpha) < 10$  contain at least 10 hops.

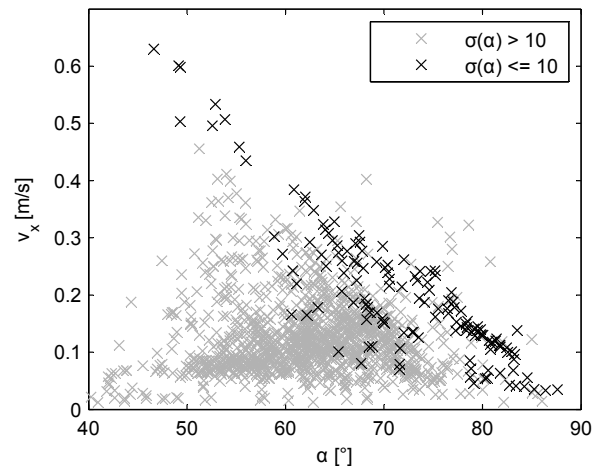


Figure 4.5: Forward-speed as a function of the take-off angle  $\alpha$ . The highest forward-speed is  $0.63\text{m/s}$  with  $f_T = 2.9\text{Hz}$ ,  $R = 0.3\text{m}$ ,  $\beta = 1 : 05\text{rad}$ . Runs with  $\sigma(\alpha) < 10$  contain at least 10 hops.

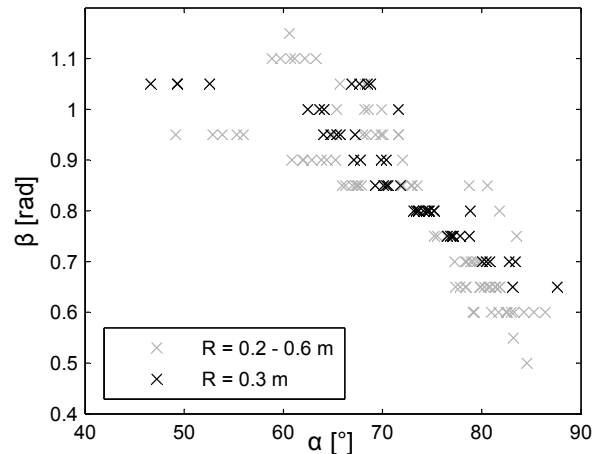


Figure 4.6: Simulated relation between take-off angle  $\alpha$  and lower leg angle  $\beta$  for different foot radii  $R$ . Runs with  $\sigma(\alpha) < 10$  contain at least 10 hops.

#### 4.4.1 Stability

In a first experiment, we explored the robot's behavior for different foot radii  $R$ , angular frequencies  $f_T$  and foot angles  $\beta$ . It turned out that successful hopping on flat ground is possible for a wide range of geometric parameters, input energy and speed. The results of the experiment are shown in Fig. 4.3.

First, it can be seen that the parameter range for successful runs is larger at larger foot radius  $R$ . While there are successful runs for each angular frequency  $f_T$  independent from the foot radius, the range of successful runs for different lower leg angles increases with increasing foot radius. A possible explanation for this behavior is founded in the fact that larger foot radii lead to larger distances between the foot circle center point and the center of mass. This results in increased raising moments. Second, the standard deviation of the take-off angle  $\alpha$  indicates high stability of motion at lower frequencies. For  $R = 0.2$  m it shows a clear link between high cost of transport, low take-off angle  $\alpha$  and low standard deviation of  $\alpha$ . For  $R = 0.6$  m, this connection does not exist.

#### 4.4.2 Cost of transport and forward speed

In a second experiment we explored the parameter influence on the forward-speed and on the efficiency of locomotion, indicated by the cost of transport (COT). The cost of transport is defined as follows

$$COT = \frac{E_{in}}{m \cdot g \cdot s}, \quad (7)$$

with the input energy  $E_{in}$ , the robot mass  $m$ , the gravitational acceleration  $g$  and the travelled distance  $s$ . For the simulation, we calculate the input energy out of the joint torque during the whole run including accelerating from deadlock

$$E_{sim} = \int_{t_0}^{t_1} T_M(t) \cdot d\varphi, \quad (8)$$

Motor, Motor Controller and Gearbox losses are neglected in this experiment.

Fig. 4.4 shows the average costs of transport for the same set of parameters used for Fig. 4.3. The best COT was 0.458 achieved with the parameter set  $f_T = 2.9$  Hz,  $R = 0.3$  m,  $\beta = 1.05$  rad. Fig. 4.5 shows the corresponding average forward-speed. The highest forward-speed achieved was 0.63 m/s with the parameter set of the lowest cost of transport.

It can be seen that runs with a low standard variation of the take-off angle  $\alpha$  show both the highest forward-speed and the lowest cost of transport with respect to the jumping angle. A steady and continuous hopping motion is a direct hint for low cost of transport. This fact is very useful for (automatic) parameter tuning.

While the area for high cost of transport and low forward speed is extensive, the sharp edge at low cost of transport and high forward-speed indicates a theoretical limit for the two parameters. For the minimum cost of transport depending on the take-off angle  $\alpha$  we can formulate a relation as follows

$$COT_{min} = \frac{1}{4}(1 - \epsilon_N)^2 \tan(\alpha), \quad (9)$$

For this function we assumed that only the vertical element of the velocity is lossy due to impact losses determined by the normal restitution coefficient  $\epsilon_N$ . The horizontal element of the velocity is assumed to be lossless which is equal to no friction during stance phase. An ideal foot rolling motion would correspond to this assumption.

Fig. 4.6 shows a nearly linear connection between the lower leg angle  $\beta$  and the resulting take-off angle  $\alpha$ . While  $\alpha$  directly determines the forward-speed (see Fig. 4.5), this result qualifies  $\beta$  as a direct control parameter for the forward-speed.

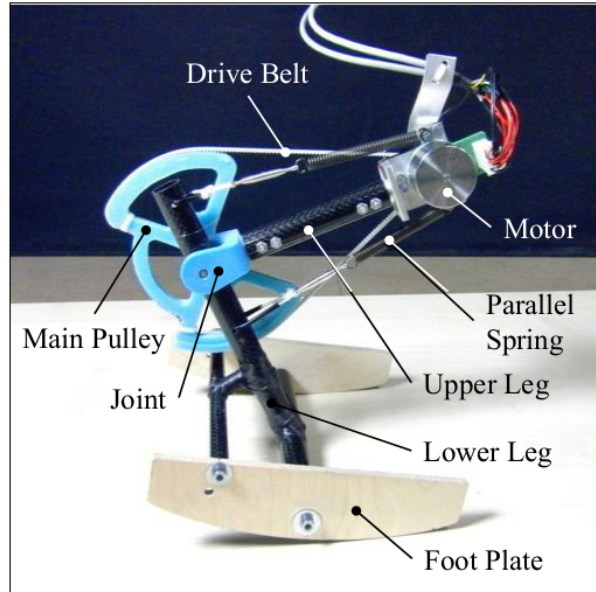


Figure 4.7: Picture of the curved foot hopper CHIARO used for the experiments. All parameters are identical to the model used for the simulations. The joint torque is generated by a brushless outrunner motor (Maxon EC45 flat, 70W) and transmitted with a timing belt drive. The drive has a gear ratio of 1:12.75, the main Pulley is connected to the lower leg. Screwed plywood footplates allow easy change of foot radius  $R$  and lower leg angle  $\beta$ . The push-pull spring of the simulation model is realized using two opposed pull-springs with half of the spring stiffness.

## 4.5 Physical experiments

The CAD model of the physical platform was developed in parallel with the simulations to guarantee a good grade of consistency. In addition, we chose the parameters to vary based on the mechanical constraints, this means we only varied parameters in the simulation for which the modification on the physical platform is easy.

### 4.5.1 Physical platform

The curved foot hopper CHIARO is shown in Fig. 4.7. Upper and lower leg of the robot were made of carbon tubes with a ball bearing knee joint out of 3D print material. This design approach guarantees lightweight and stiff parts with a high grade of modularity and low manufacturing time. The foot is realized using two plywood plates which are screwed to the lower leg. A distance of 0.2m guarantees a save stand and prevents the robot from falling to the side. The manufacturing of the plates is easy and fast, so different foot radii and lower leg angles can be realized by changing the foot plates. The joint torque is generated with a brushless outrunner motor (Maxon EC45 flat, 70W) and transmitted with a timing belt drive. The drive has a gear ratio of 1:12.75, the main Pulley is connected to the lower leg. The pushpull spring of the simulation model is realized using two opposed pull-springs with half of the spring stiffness. The motor mount with the counter bearing to hold the tension of the pulley is made of aluminium. An encoder is mounted on the motor shaft to enable precise tracking of the motor position and knee angle. The whole robot (except the motor mount) can be manufactured and assembled within two days. The motor is torque controlled using a MAXON Escon 50/5 motor driver and a PC with MATLAB. The motor wires are guided in a long loop above the robot to minimize the influence of wiring mass.

Absent any inertial sensing on CHIARO, we used an OptiTrack optical tracking system to

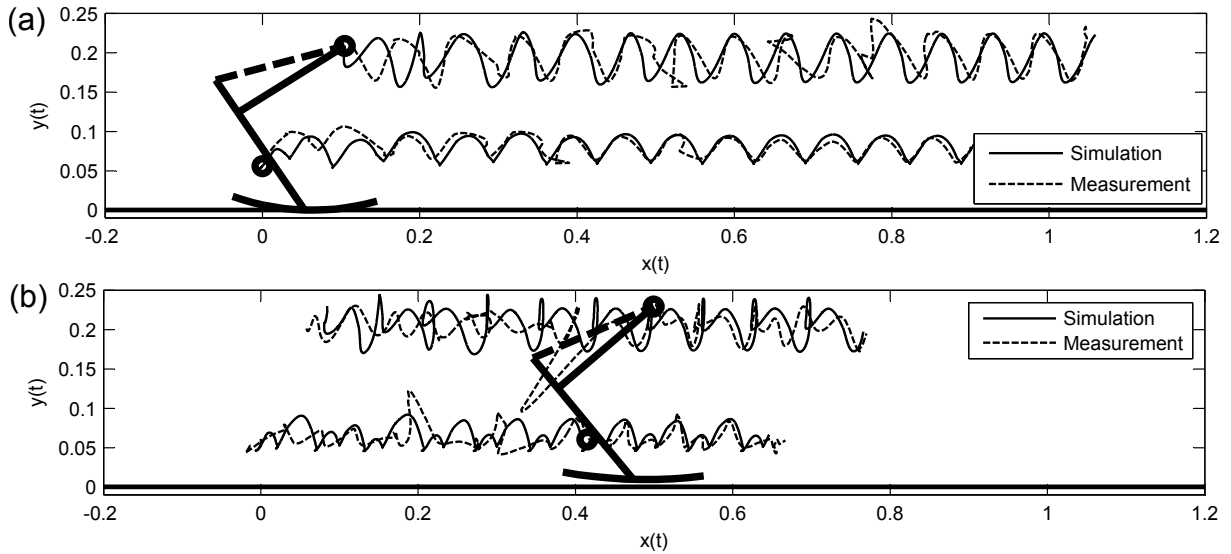


Figure 4.8: Trajectory of upper and lower COM for simulated and physical runs. The parameters were set according to Tab. 4.1. (a) shows a run with low standard variation of  $\alpha$  with  $f_T = 3.4$  Hz,  $R = 0.3$  m,  $\beta = 1.05$  rad. The accordance between experiment (dotted line) and simulation (continuous line) is excellent, the anomalies especially for the upper COM are founded in high noise of the optical tracking system. (b) shows a run with high standard deviation of  $\alpha$  with  $f_T = 4.3$  Hz,  $R = 0.6$  m,  $\beta = 0.9$  rad. The speedup phase of the robot differs between simulation and experiment, but after a few hops at final speed the motion stabilizes and the accordance is good. The anomalies especially for the upper COM are again founded in high noise of the optical tracking system.

record the robot's position and orientation. Due to high noise, the visual tracking data was filtered using a Gaussian filter.

#### 4.5.2 Simulation tuning and accordance analysis

In a first experiment, we tested the accordance between simulation model and physical platform. We chose several successful parameter sets out of the simulation (see section IV-A) and repeated the run with the physical platform with identical parameter set up according to table I. Based on this data we performed a fine tuning of the damping coefficient and friction, while all other simulation parameters were left constant. The results are shown in Fig. 4.8. For low standard deviations of  $\alpha$  the data shows an excellent accordance between simulated and physical values. For higher standard deviations, the basic behavior is still well mapped. Due to more and more chaotic behavior of the robot, the data differs during the acceleration phase.

The accordance of the standard deviation between simulation and experiment was very high for every run performed, so the simulation seems to be a good tool to predict the standard deviation for future runs with other parameter sets. Due to this fact we believe that the simulation can be used for both, subsequent analysis of the physical platform's behavior as well as prediction of future robot behavior, as long as the standard deviation of the analyzed run is low enough.

## 4.6 Conclusion

This chapter investigated a novel one legged hopper that takes advantage of a curved foot. The system is feed forward controlled, all stabilization is done mechanically. Among others, this chapter specifically investigated the influence of the curved foot approach on stability and



efficiency over a wide range of parameters and forward velocities. By keeping the physical platform as simple as possible, we were able to describe the system with a high grade of accuracy. By analyzing the robots behavior using numerical analysis, we were able to gain insights in the interaction of the system parameters and their influence on stability and efficiency and identified stable regions of parameters. We identified the foot angle as a direct determining factor for the hopping angle and thus for the achievable forward-speed. By comparing the simulation with the experiments, we determined excellent accordance which verifies the simulation and empowers it for both, explanation and prediction of robot behavior.

In the future we continue more comprehensive analysis on system borders (max. speed and min. COT) and exploration on parameter interaction with the target to explore the underlying mechanisms of the robots self stabilizing properties.

## Chapter 5

# Improved energy efficiency through body mass support in parallel elastic monopod running<sup>1</sup>

This chapter focuses on the use of springs for improving energy efficiency of legged locomotion. Due to their ability of storing and recoiling energy with very low internal losses, springs can support the actuators of a legged robot in handling the inevitable fluctuations of kinetic energy which occur during legged locomotion. By carefully tuning the springy mechanics, it theoretically becomes possible to perform all fluctuations with the springs, and use the actuators only for energy input to overcome friction and impact losses. Based on this concept of passive dynamic locomotion, various springy dynamics have been employed for efficient legged locomotion, for example preloading for efficient walking [84] and running [34] or series elastic actuation for efficient running [41, 143].

As demonstrated in the previous chapter, parallel elastic actuation, combined with an optimized robot design, can enable robust forward running at various speeds. In addition, the parallel spring is able to provide body weight support. This property is of special interest for energy efficiency, since nature shows that heavier terrestrial animals tend to be more energy efficient [144]. In order to exploit this mechanism, we designed Cargo, a third-generation parallel elastic runner which is able to carry additional payload up to 5 times its own body weight. By exploiting the inherent robustness of these runners, Cargo is able to handle these different payloads without any changes in its morphology.

Cargo is designed as a passive dynamic runner and its parallel spring is intended to handle the large majority of the energy fluctuations which occur during running. The main fluctuation thereby occurs during stance phase, when the vertical component of the center of mass (COM) speed needs to be reversed. To do so, the robot needs to first perform negative work (force contradictory to the COM velocity) to brake the COM down, and then positive work to re-accelerate the COM. Therefore, a significant amount of negative work in any component of the robot indicates that this component contributes to this energy fluctuation. In reverse, if an actuator of a springy robot performs no negative work at all, this indicates that all the energy

---

<sup>1</sup>This chapter presents the collaborative work with my colleague Y. Shu under guidance of my supervisor F. Iida. I designed the experimental platform and contributed to the simulation and physical experiments and the writing of the manuscript, together with my supervisor F. Iida. My colleague Y. Shu contributed to the simulation. This chapter has been adapted and edited from the following publications:

- F. Guenther and F. Iida. Energy efficient monopod running with large payload based on open loop parallel elastic actuation. *Accepted for publication in IEEE Transactions on Robotics*
- F. Günther, Y. Shu, and F. Iida. Parallel elastic actuation for efficient large payload locomotion. In *Proc. 2015 IEEE Int. Conf. Robotics and Automation (ICRA)*, pages 823–828, Seattle, WA, 2015

fluctuations are done by the springs entirely. This case occurs with Cargo, where the actuator performs up to 98 % positive work. Therefore, Cargo is a nearly perfect example of an actuated passive dynamic locomotor.

## 5.1 Introduction

Legged locomotion is an important mode of mobility for robotic systems especially in highly constrained environment such as unstructured and uncertain rough terrains. While we witnessed the significant improvement in control of legged robots in the last decade, there has been only relatively slow progress in the investigation of energy efficiency, even though it is an equally important problem.

In general legged robots have been known to require orders of magnitude more energy for locomotion if compared to the biological systems in the similar sizes and weights. This line of investigations was pioneered by Gabrielli and von Karman in 1950s [145], where the definition of specific resistance (also known as cost of transport, COT) was introduced to compare energy efficiency among various biological and man-made systems. The work was extended by Tucker [146] and Kuo [58] by comparing energy efficiency with respect to body masses. These investigations showed that biological systems of similar weights exhibit the similar range of COT although most of legged robots require significantly more.

The majority of energy efficiency researches was reported in the context of bipedal robot walking [56, 84] (and running, [147]). Here the efficiency is measured with respect to the so-called total cost of transportation (TCOT), which refers to the total use of energy including both mechanical and electrical which is standardized by unit mass and unit travel distance. The current record of TCOT reported so far was achieved by the Cornell Biped ([84], TCOT = 0.2) and the Cornell Ranger ([56], TCOT = 0.19), both robots based on articulated rigid legs.

For running and hopping locomotion, Spring Loaded Inverted Pendulum (SLIP) has been investigated thoroughly in the past [48, 49]. This approach makes use of series elastic actuators [61], i.e. mechanical springs are installed between motors and leg structures, which play a role of shock absorbers as well as energetic buffers to recover some of the kinetic energy over multiple steps. The reported record of this approach (by [86], and [143]) was a mechanical COT of 0.22 and 0.2, respectively. Though not relying on mechanical springs, the MIT Cheetah robot reported an impressive achievement of TCOT 0.5 [148], even though the efficiency is still far from those of the biological systems. Parallel elasticity was investigated for spine [42, 70] and leg actuation [34] on several occasions. However, investigations on its influences to energetic efficiency of leg actuation have just yet started [149]. In general, there is still no commonly agreed principles about the use of mechanical dynamics for locomotion with various speed and body mass.

In this chapter, we investigate an approach that make use of parallel elastic actuation for the purpose of energetic efficiency of hopping locomotion. Unlike the other models investigated in the past, this approach makes use of a mechanical spring incorporated in parallel with relatively low-torque actuator, which is used as the main drive of locomotion. The mechanical spring here can be used to support the variations of payload while it can trigger self-excited vibration for the purpose of locomotion. Through the analysis in simulation and physical robot platform, we will show that this approach enables hopping locomotion with significantly better energy efficiency beyond the existing robots and animals.

Please note that this chapter is an extension of our previous work [4, 6]. We have both extended simulation and real-world experiments in order to thoroughly analyze the proposed approach. The rest of the chapter is structured as follows: Section 5.2 describes the detailed design and physical modeling of the robot. Simulation setup and simulation experiments are presented in Section 5.3. Section 5.4 describes the design of the physical platform which is used in Section 5.5 to confirm the simulation results and measure the payload carrying performance,

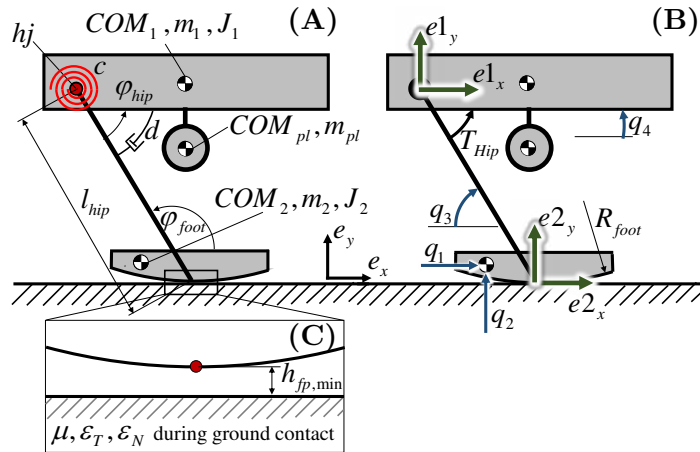


Figure 5.1: Illustration of the physical model (A,B) and the ground contact setup (C, see Section 5.3.1) of Cargo used for the simulations.

followed by discussion and conclusion.

## 5.2 Design and modeling

This Section describes the physical model of Cargo used for simulations and introduces the strategies for payload attachment and actuation.

### 5.2.1 Physical model

In contrast to Cornell Ranger [56] and Cornell Biped [84], which are both walkers with rigid legs, Cargo is realized as a compliant monopod runner with a two-segmented leg and a curved foot, similar to [4]. The physical model of Cargo (Fig. 5.1) is planar and consists of two rigid bodies (lower and upper leg) with mass ( $m_1, m_2$ ), center of mass ( $COM_1, COM_2$ ), and rotational inertia ( $J_1, J_2$ ). Payload is modeled as a point mass ( $m_{pl}, COM_{pl}$ ) and rigidly attached to the upper leg. Upper and lower leg are connected with a rotational hip joint on which a linear torsional spring is attached. On the hip joint, a motor torque can be applied in parallel to the spring. The losses of the spring mechanism are modeled by a linear rotational damper in the joint. The lower body is equipped with a curved foot which establishes ground contact during stance phase.

The curved foot is designed as a circle with constant radius, and its purpose is to introduce self stabilizing dynamics to the system, in order to reduce sensing and control effort. Curved feet in general can improve both robustness and energy efficiency of walking [51, 84] and running [4, 150–152]. The same principle can be observed in nature as human feet roll over the ground during walking, similar to a wheel [153, 154].

Between ground and foot, dynamic friction with friction coefficient  $\mu$  and impact with restitution factor  $\epsilon_N, \epsilon_T$  occur during stance. The rest leg length of Cargo, defined as the distance between ground contact point and COM with the spring at rest length and the robot being balanced, is  $L_{leg,rest} = 0.36$  m. The weight distribution of the robot is designed in a way that, when standing on the ground in *initial posture* (Fig. 5.2), the upper body is roughly horizontal. Previous research [4] indicated that a more horizontal upper body angle is beneficial in terms of energy efficiency.

The payload of Cargo consists of weight plates up to 0.45 m diameter and is attached at a fixed point on the upper body and able to rotate freely around the z-axis. When standing in initial posture, this fixed point lies in line with the robot center of mass and the foot contact

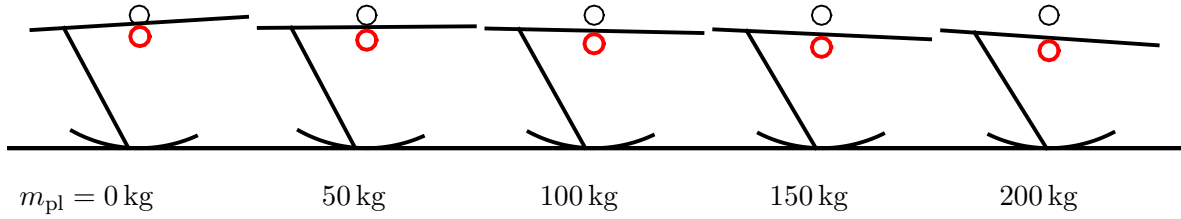


Figure 5.2: Illustration of the initial robot posture depending on the payload without hip torque input. The red circle marks the center of mass of the robot, the black circle represents the center of the foot circle.

point. The robot is balanced without payload (Fig. 5.2 left), and the lower body angle with respect to the ground does not change significantly when adding payload (Fig. 5.2 right).

In order to reduce vertical impact losses, low mass of upper and lower body of Cargo is desirable. Since reduced stress on the structure is key towards the goal of low mass, long stance phases with low vertical accelerations and therefore low stress on the structure would be beneficial. This can be accomplished by choosing a low spring stiffness. On the other hand, a stiff spring would minimize the posture change during bouncing on the ground and therefore ease the analysis. As a compromise, we chose the spring stiffness in a way that the hip angle oscillation remains within  $\pm 0.52$  rad ( $\pm 30^\circ$ ), which allows for hopping with 150 kg payload and 35 N m hip torque. With the max. hip angle oscillation set, the necessary ground clearance of the weight plates finally determines the size of the robot which results in the parameter set displayed in Tab. 5.1.

For the simulation, upper body and payload mass are considered as one body. While payload and upper body mass can simply be summed up:

$$m_{1\text{pl}} = m_1 + m_{\text{pl}}, \quad (5.1)$$

the total center of mass of the upper body  $\vec{r}_{\text{COM1pl}}$  in the inertial frame is calculated as follows:

$$\vec{r}_{\text{COM1pl}} = \frac{m_1 \cdot \vec{r}_{\text{COM1}} + m_{\text{pl}} \cdot \vec{r}_{\text{COMpl}}}{m_1 + m_{\text{pl}}}. \quad (5.2)$$

The total inertia of the upper body  $J_{1\text{pl}}$  follows in a similar way

$$J_{1\text{pl}} = J_{1,\text{hj}} + |\vec{r}_{\text{hj}}^{\text{COMpl}}|^2 \cdot m_{\text{pl}} - m_{1\text{pl}} \cdot |\vec{r}_{\text{hj}}^{\text{COM1pl}}|^2. \quad (5.3)$$

with  $\vec{r}_{\text{hj}}^{\text{COMpl}}$  being the distance between hip joint and payload COM in the inertial frame and  $\vec{r}_{\text{hj}}^{\text{COM1pl}}$  the distance between hip joint and the total COM of the upper body.

Ground friction coefficient, hip joint damping, and gearbox efficiency, were validated using the physical prototype presented in Section 5.4.1. A dynamic friction coefficient of 0.23 between foot disc and ground was measured for the plywood foot sliding on the MDF surface of the test track. Static friction on the same track was about 1.5 times higher. We merged both static and dynamic friction coefficient into a simulation friction coefficient of 0.28. The average damping coefficient was determined to 1.3 N m s/rad by measuring the passive swing motion of the robot after the run. The gearbox efficiency of 0.95 was calculated out of typical values for optimized spur and chain gears.

### 5.2.2 Equations of motion

Similar to [4], the state of the physical model (Fig. 5.1) is expressed using generalized coordinates:

$$\mathbf{q} = (q_1 \ q_2 \ q_3 \ q_4)^T \quad (5.4)$$

Table 5.1: Model parameters

$A_{\text{hip}}$	Hip torque amplitude	[0..55] N m
$L_{\text{leg,rest}}$	Rest leg length	0.36 m
$P_{\text{idle}}$	Power consumption of the on board computer	2 W
$P_{\text{comp}}$	Idle power consumption of the motor controller	0.1 W
$R_{\text{foot}}$	Foot radius	0.42 m
$R_{\text{motor}}$	Electric resistance of the motor	0.3 $\Omega$
$c$	Hip spring stiffness	2276 N m/rad
$d$	Hip damping coefficient	1.3 N m s/rad
$f_{\text{hip}}$	Hip torque frequency	[0..6] Hz
$i_{\text{gear}}$	Gear reduction	148
$k_m$	Motor torque constant	0.0302 N m/A
$l_{\text{hip}}$	Hip length	0.441 m
$m_1$	Upper body mass	19.287 kg
$m_2$	Lower body mass	13.687 kg
$m_{\text{pl}}$	Payload mass	[0 kg..200] kg
$e_1 \vec{r}_{\text{COM1}}$	COM Position upper leg	[0.355; 0.002] m
$e_2 \vec{r}_{\text{COM2}}$	COM Position lower leg	[-0.171; 0.308] m
$\vec{r}_{\text{COMpl}}$	Payload COM	[0.229; -0.043] m
$\epsilon_N, \epsilon_T$	Normal and tangential restitution factor	0
$\eta_{\text{gear}}$	Gear efficiency	0.95
$\eta_c$	Motor controller efficiency	0.9
$\mu_{\text{gr}}$	Ground friction coefficient	0.28
$\varphi_{\text{foot}}$	Foot angle	2.123 rad
$\varphi_{\text{hip,rest}}$	Hip angle with torque spring at rest	1.763 rad
$J_{1,\text{hj}}$	Upper body inertia at hip joint	2.890 kg m <sup>2</sup>
$J_{2,\text{hj}}$	Lower body inertia at hip joint	0.627 kg m <sup>2</sup>
$J_{\text{mot,hj}}$	Motor inertia with respect to the hip joint	0.396 kg m <sup>2</sup>
<b>State variables</b>		
$q(t)$	Generalized position coordinates	m, rad
$u(t)$	Generalized speed coordinates	m/s, rad/s
<b>Simulation variables</b>		
$dt_{\text{sim}}$	Simulation timestep	[0.025..0.5] ms

Table 5.2: Limitations of the physical prototype

$n_{\text{max}}$	Maximum motor speed	1257 rad/s
$I_{\text{mot,max}}$	Maximum continuous motor current	8.27 A
$\Delta\varphi_{\text{hip,max}}$	Maximum hip deflection	$\pm 0.52$ rad

During flight phase, the equations of motion can be displayed as

$$\mathbf{M}d\dot{\mathbf{q}}(\mathbf{q}, t) - \mathbf{h}(\mathbf{q}, \dot{\mathbf{q}}, t)dt = 0 \quad (5.5)$$

with mass matrix  $\mathbf{M}$  and  $\mathbf{h}$  summing up gyroscopic accelerations and smooth, generalized forces, including hip actuation. During stance, the equations of motion are extended by the measure of the contact forces  $d\mathbf{R}$  as proposed in [142]:

$$\mathbf{M}\ddot{\mathbf{q}} - \mathbf{h}dt - d\mathbf{R} = 0. \quad (5.6)$$

By defining system state dependent force laws for  $d\mathbf{R}$ , it is possible to set up an optimization problem (linear complementary problem) for the contact forces. We assumed a Newtonian impact behavior

$$v_{\text{N}}^+ = -\epsilon_{\text{N}} \cdot v_{\text{N}}^-, \quad v_{\text{T}}^+ = -\epsilon_{\text{T}} \cdot v_{\text{T}}^- \quad (5.7)$$

with  $v_{\text{N}}^-, v_{\text{T}}^-$  being the normal/tangential velocities of the colliding body just before impact and  $v_{\text{N}}^+, v_{\text{T}}^+$  the normal/tangential velocities right after impact.  $\epsilon_{\text{N}}, \epsilon_{\text{T}}$  are the normal and tangential impact factors, which we assumed to be zero in our model. This results in no energy to be recovered from the unsprung mass. Friction on the ground is modeled using simplified Coulomb friction with identical static and dynamic friction coefficient  $\mu_{\text{gr}}$ :

$$F_{\text{T}} = -\text{sign}(\vec{v}_{\text{fp}}) \cdot \mu_{\text{gr}} \cdot F_{\text{N}}, \quad (5.8)$$

with  $F_{\text{N}}$  being the normal and  $F_{\text{T}}$  being the tangential component of the foot contact force. Once the solution for the linear complementary problem is found, we can re-enter the contact forces in Eq. (5.6) and integrate normally.

### 5.2.3 Actuation strategy

The hip joint of Cargo is actuated by using open loop clock torque control [155] in a parallel elastic configuration, in which a linear rotational spring is implemented in parallel with a linear damper and a back-drivable actuator. The actuator provides a sinusoidal hip torque on the joint

$$T_{\text{hip}}(t) = A_{\text{hip}} \cdot \sin(2 \cdot \pi \cdot f_{\text{hip}} \cdot t), \quad (5.9)$$

with amplitude  $A_{\text{hip}}$  and frequency  $f_{\text{hip}}$  as the two determining parameters. In Eq. (5.6) the hip actuation is integrated in the  $\mathbf{h}$ -vector as follows:

$$\mathbf{h} = (0 \ 0 \ T_{\text{hip}} \ T_{\text{hip}})^T + \mathbf{h}_{\text{other}}. \quad (5.10)$$

The motor torque which is necessary to create this hip torque is calculated by including gearbox efficiency  $\eta_{\text{gear}}$  as follows:

$$T_{\text{mot}} = \begin{cases} T_{\text{hip}}/\eta_{\text{gear}} & \text{if } T_{\text{hip}} \cdot \dot{\varphi}_{\text{hip}} > 0 \text{ (forward-drive)} \\ T_{\text{hip}} \cdot \eta_{\text{gear}} & \text{elsewhere (back-drive)} \end{cases}. \quad (5.11)$$

The mechanical motor power is calculated as:

$$P_{\text{mot}} = T_{\text{mot}} \cdot \dot{\varphi}_{\text{hip}} \quad (5.12)$$

The electric power input into the motor is calculated by using the electric DC motor model with torque constant  $k_{\text{m}}$ . By using motor current  $I = \frac{T_{\text{mot}}}{k_{\text{m}}}$  and motor voltage  $U = \dot{\varphi}_{\text{mot}} \cdot k_{\text{m}} + I \cdot R_{\text{mot}}$ , electric motor power results in

$$P_{\text{el}} = P_{\text{mot}} + \left( \frac{T_{\text{mot}}}{k_{\text{m}}} \right)^2 \cdot R_{\text{mot}}. \quad (5.13)$$

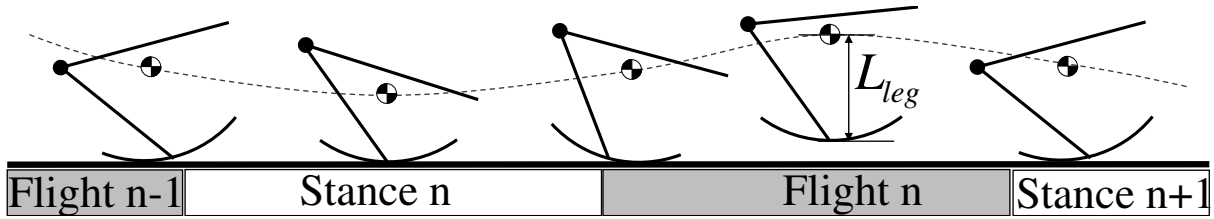


Figure 5.3: Illustration of one step of successful running with the flight phase highlighted in grey for  $m_{pl} = 100$  kg. One step  $n$  starts at touchdown when the foot circle touches the ground and ends at the next touchdown  $n + 1$ .

The motor controller consumes an idle power  $P_{idle} = 2$  W and has an efficiency of  $\eta_c = 0.9$  for both forward- and back-drive. The on board computer consumes  $P_{comp} = 0.1$  W which results in a total power consumption of:

$$P_{tot} = P_{idle} + P_{comp} + P_{el} \cdot \eta_c. \quad (5.14)$$

Positive  $P_{tot}$  thereby indicates that energy is consumed from the power supply, while negative  $P_{tot}$  indicates that energy is recovered into the power supply.

In the physical platform, motor speed, continuous motor current and hip spring deflection are limited according to Tab. 5.2. For the implementation in the simulation, see Section 5.3.4.

## 5.3 Simulation results

In this section, we describe the simulated performance of Cargo for varying hip torque amplitude  $A_{hip}$ , hip torque frequency  $f_{hip}$ , and payload  $m_{pl}$ . After introducing the basic running pattern and stability behavior, we explore the robot's behavior at constant payload  $m_{pl} = 100$  kg for different hip torque and frequency input and establish a filter process to separate periodic running solutions from other types of locomotion. Based on this data, we analyze the periodic running solutions in terms of efficiency and forward speed. And finally, we generalize these findings for variable payload.

### 5.3.1 Simulation setup

To solve the equations of motion (Eq. 5.6) numerically, we implemented a time stepping algorithm based on the midpoint rule in MATLAB. Ground contact is modelled using one single contact point. This point lies on the foot disc vertically below the center of the disc. When the robot is moving, this contact point has not a fixed position on the foot disc but is recalculated for every simulation step (see Fig. 5.1c). As soon as the distance between contact point and ground becomes zero or negative, ground contact is established. With only one contact point, the number of cases for the linear complementary problem (LCP) is  $2^{(3 \cdot 1)} = 8$ , which allows for calculating all LCP cases until a solution is found. If no solution for the LCP was found for the default step size of 0.5 ms, the step size is bisected and the simulation step repeated, if necessary down to a step size of 0.025 ms. A simulation run always starts with the robot standing still in initial position where body weight and spring torque are balanced and the COM of the system lies vertically over the contact point of the foot and the ground. Then the sinusoidal hip torque is applied for 50 cycles, starting from zero torque.

### 5.3.2 Running dynamics

Cargo is designed for forward running on level ground. One step of running (Fig. 5.3) starts at *touchdown* when the upper body bounces downward during *stance* phase and the torque spring in



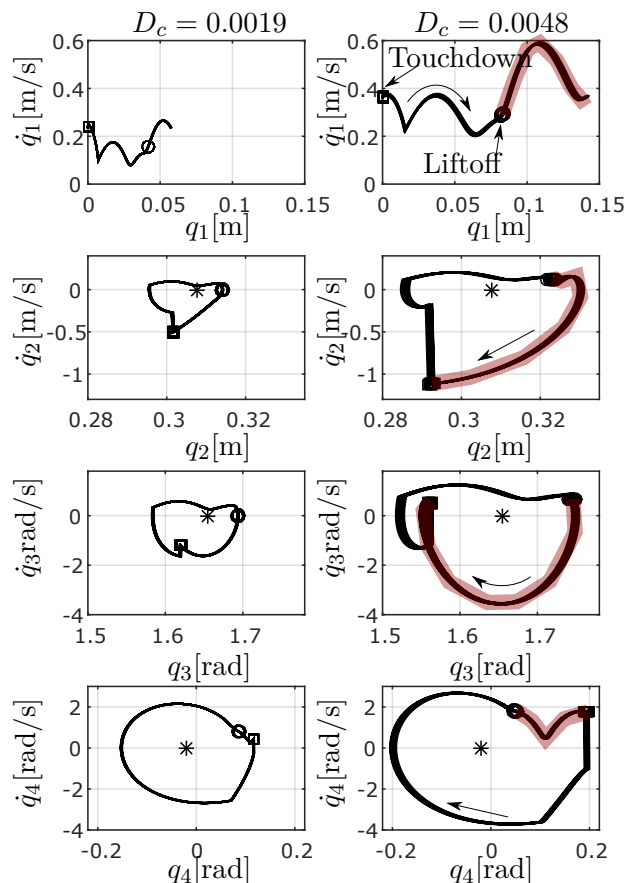


Figure 5.4: Phase plots of the robot state variables and according cyclic deviation  $D_c$  during successful running. The stable fixed point is indicated with a \*. (a) Last 25 steps of the run with lowest resulting cyclic deviation at  $m_{pl} = 100$  kg,  $A_{hip} = 18$  N m,  $f_{hip} = 2.62$  Hz. Touchdown of each step is indicated with a square, liftoff with a circle. The flight phase is highlighted in orange. (b) Last 25 steps of the run with highest cyclic deviation at  $m_{pl} = 100$  kg,  $A_{hip} = 52$  N m,  $f_{hip} = 2.41$  Hz.

the hip joint gets compressed. After mid-stance, the upper body bounces back, gaining vertical speed and a counter-clockwise momentum for the following swing leg motion. During stance, rolling motion and sliding of the foot on the ground occur. At the end of the stance phase, the foot leaves the ground at *liftoff* and the upper body swings backwards during *flight* phase. When shutting down the motor input immediately during running, the robot takes one to three additional steps while continuously braking down to standstill. This running is entirely based on the robot's passive dynamic behavior and looks very similar to the actuated steady state running.

### 5.3.3 Running stability

With 100 kg payload and no motor torque input, Cargo has a stable fixed point at  $q^* = [0 \ 0.308 \ 1.655 \ -0.022]^T$ , which corresponds to its initial posture in Fig. 5.2. With an appropriate set of actuation parameters, Cargo exhibits stable running with small orbital deviations. As shown in phase plots (Fig. 5.4), the robot is capable of cyclic running behaviors, some of which are very stable (Fig. 5.4a), and the others with more deviations (Fig. 5.4b). On the phase plots, the impact at touchdown is the most prominent feature and can be located clearly for each state variable due to the sudden change in speed.

In order to quantify such deviations, here we introduce a metric called *cyclic deviation* defined

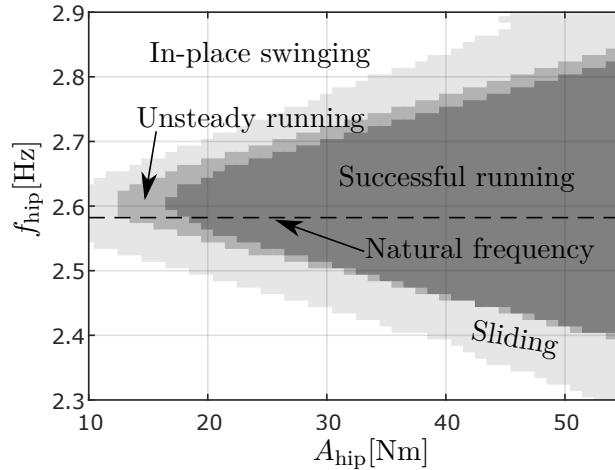


Figure 5.5: Motion patterns for a given hip torque frequency  $f_{\text{hip}}$  and amplitude  $A_{\text{hip}}$  with  $m_{\text{pl}} = 100$  kg. All successful runs together shape the *successful running area*. Above  $A_{\text{hip}} = 55$  Nm, the maximum motor current (see Tab. 5.2) is exceeded and no successful hopping is possible. Outside of the successful running area, unsteady running, sliding or in-place swinging occurs.

as:

$$D_c = \sigma(q_{3,\text{touchdown}}) + \sigma(q_{4,\text{touchdown}}) \quad (5.15)$$

by summing up the averaged standard deviations of state variables  $q_3$  and  $q_4$  at touchdown. Visually,  $D_c$  is connected to the horizontal “thickness” of the line of the overlapped steps at touchdown. The thinner these line at touchdown, the lower  $D_c$  and the more uniform the run.

### 5.3.4 Conditions for successful running

Depending on the specific parameter choice of the motor input, Cargo performs forward running as well as in-place swinging and sliding locomotion. A run starts with the sinusoidal hip torque (Eq. 5.9) being applied to the robot standing still in initial posture. This torque is then applied for 50 cycles before shutting down the power. When applying the hip torque, the robot first builds up the oscillation of the upper body, then accelerates and finally reaches steady state forward running for certain motor input. To separate periodic running solutions from all other types of locomotion, we use a filter process based on the 50 cycles of the motor torque during a simulation run:

1. The average horizontal speed of the robot COM needs to be positive for each of the last 25 motor torque cycles. Patterns without forward locomotion are called in-place swinging.
2. The robot must be in flight phase during at least one simulation time step during each of the last 25 motor torque cycles. The maximum hopping height needs to be at least 0.002 m for each step. Patterns with forward speed but without any flight phases are called sliding. Patterns with forward speed but without enough or high enough flight phases are called unsteady running.
3. Motor and spring limitations (Tab. 5.2) need to be fulfilled during all 50 motor torque cycles.
4. Within the last 25 motor torque cycles, the average forward speed of the fastest cycle must not be more than 1.2 times larger than the average forward speed of the slowest cycle. Any running pattern with larger forward speed deviation is called unsteady running.

We call every locomotion pattern which fulfills these conditions *successful running* and the associated simulation run and parameter set *successful run*.

To explore the robot's behavior for different hip torque parameters, we conducted simulation runs for each possible combination of hip torque amplitude  $A_{\text{hip}}$  and frequency  $f_{\text{hip}}$  with a resolution of 1 N m and 0.1 Hz, respectively. When displaying the successful runs in the motor torque amplitude-frequency plane (Fig. 5.5) a conical shape with the tip towards lower amplitude can be observed, which we call *successful running area*. The frequency at the tip is very close to the natural frequency of the robot, which occurs when the robot stands on the ground and swings passively. While successful running with minimum forward speed and foot clearance is only possible near this natural frequency, with increasing motor torque amplitude, the swinging amplitude around the hip increases too and enables higher energy input. With the actuator energy becoming larger with respect to the spring energy of the system, higher motor torque amplitudes allow for larger deviations from the natural frequency, and therefore a larger usable frequency range.

All successful runs we conducted so far show stable forward running (see Section 5.3.3) and follow the pattern described in Section 5.3.2. Fig. 5.4 thereby shows the lowest and highest cyclic deviation of all successful runs performed at  $m_{\text{pl}} = 100$  kg.

### 5.3.5 Energetic characteristics

The total cost of transport

$$\text{TCOT} = \frac{1}{n} \sum_{i=1}^n \frac{1}{m \cdot g} \cdot \frac{\int_i^{i+1} P_{\text{tot}} \cdot dt}{\int_i^{i+1} v_{\text{COMx}} \cdot dt} \quad (5.16)$$

describes the power spent per speed per body weight during  $n$  steps. For Cargo with 100 kg payload, it distributes smoothly within the successful running area (Fig. 5.6a) with low values at the upper and lower border of the successful running area and a minimum of 0.1499 at minimum amplitude. Up to  $A_{\text{hip}} = 46$  N m, the upper border TCOT is slightly lower compared to the lower border TCOT, while this ratio reverses above  $A_{\text{hip}} = 46$  N m. Plotted separately (Fig. 5.6b), the best TCOT per Amplitude increases with increasing amplitude up to  $A_{\text{hip}} = 46$  N m and then remains nearly constant up to maximum amplitude.

The concept of COT can be applied to parts of the system too to display the energy consumption of subsystems in a dimensionless way. While the TCOT is based on the electrical energy input in the motor controller and on-board computer, the  $\text{COT}_{\text{mech}}$  for example is based on the mechanical energy output at the hip and therefore represents the efficiency of the robot mechanics neglecting the drivetrain. When plotting the minimum  $\text{COT}_{\text{mech}}$  against amplitude (Fig. 5.6b), it first remains nearly constant with a minimum value of 0.1069 along the upper border. Around  $A_{\text{hip}} = 46$  N m, it increases to its higher value along the lower border.

When hopping at minimum TCOT, the spring is doing the whole energy conversion during bouncing with a max spring torque of 629 N m and a max. energy stored in the spring of 87 J. The motor is doing 98 % positive work with a total energy input of 8 J at the hip.

### 5.3.6 Forward speed effects

The forward speed  $v_{\text{COMx}}$  is defined as the x-component of the COM speed vector. For Cargo with 100 kg payload, the forward speed distributes smoothly in the successful running area (Fig. 5.7a) and increases with increasing amplitude and decreasing frequency. The hip torque amplitude can be used (in combination with appropriately tuned frequency) to directly influence the forward speed (Fig. 5.7b). The highest forward speed of 0.3519 m/s is placed at the right lower border of the successful running area. The minimum possible forward speed of 0.1476 m/s can be found at the left tip of the successful running area. Above  $A_{\text{hip}} = 46$  N m, the locations

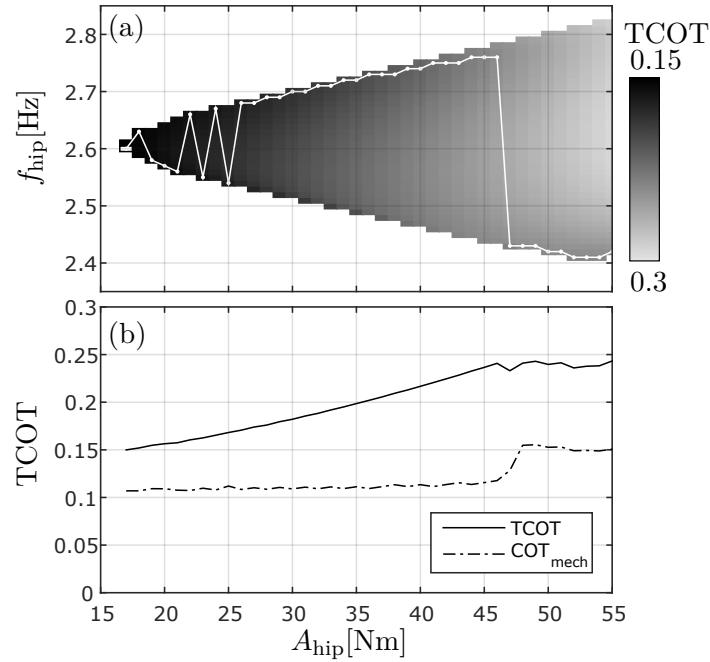


Figure 5.6: (a) TCOT for a given hip torque frequency  $f_{\text{hip}}$  and amplitude  $A_{\text{hip}}$  at  $m_{\text{pl}} = 100$  kg, indicated using gray scale. The white line indicates minimum TCOT for each hip torque amplitude  $A_{\text{hip}}$ . (b) Minimum TCOT for each hip torque amplitude and corresponding  $COT_{\text{mech}}$ .

of the maximum forward speed per amplitude and the minimum TCOT per amplitude (see Fig. 5.6a) within the successful running area are similar.

The liftoff angle is defined as the angle of the robot COM speed vector at liftoff with respect to the horizontal plane. Cargo has a liftoff angle around 0.9 rad (52°) with slightly lower values towards lower amplitude.

The distance the foot contact point travels during stance is at the same time the length of the foot part which has actually ground contact. With values below 0.078 m (22% of the leg length), the normalized effective foot length of Cargo is comparable to humans.

The duty factor or Cargo, which represents the ratio of stance time to total step time, decreases with increasing forward speed, i.e. the flight phases become longer compared to the stance phases (Fig. 5.7b). With a duty factor between 0.66 and 0.81, Cargo spends more time during stance compared to other runners. The ARL Monopod II for example has values between 0.5 and 0.6 (Fig. 10 in [86]) and values for sprinters (both legs added up) lie between 0.4 and 0.72 (Fig. 3 in [156]).

During stance, rolling and sliding of the foot occur simultaneously. The normalized rolling distance indicates the ratio of the length which is traveled by the robot COM in x-direction while rolling, normalized by the step length. The sliding distance is defined accordingly. For very low amplitudes, the foot nearly slides as much as it rolls, while towards larger amplitudes rolling becomes dominant. To clarify the underlying reasons for this behavior, future investigations are necessary.

The maximum rolling distance of 0.0668 m corresponds to a lower leg angular change of  $q_{3,\text{liftoff}} - q_{3,\text{touchdown}} = 0.185$  rad. If we now imagine Cargo with a point foot instead of the foot disc while keeping the leg length constant at  $L = L_{\text{leg,rest}}$ , the same angular change would lead to a distance traveled by the COM of 0.0665 m, nearly equal to the distance with the curved foot. Therefore, when compared to a point foot, the gain in traveled distance of the foot disc is negligible.

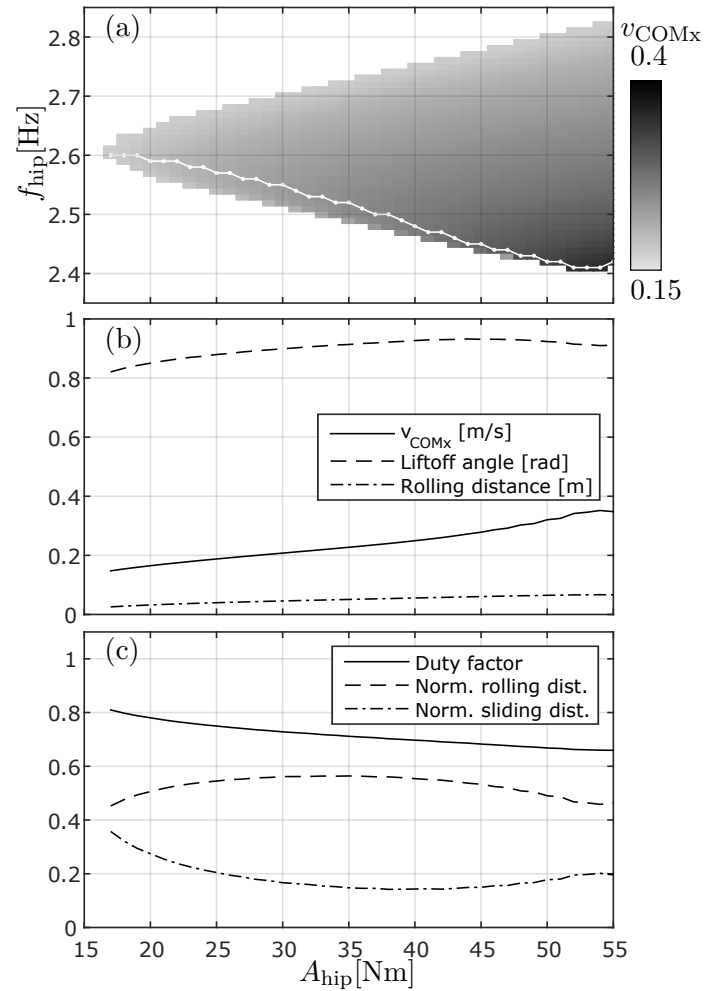


Figure 5.7: (a) Simulated forward speed  $v_{\text{COMx}}$  at  $m_{\text{pl}} = 100$  kg for a given hip torque frequency  $f_{\text{hip}}$  and amplitude  $A_{\text{hip}}$ , represented using grayscale. The white line marks the maximum  $v_{\text{COMx}}$  per amplitude. (b) Maximum  $v_{\text{COMx}}$  and corresponding liftoff angle per amplitude. (c) Duty factor, rolling distance and sliding distance, normalized with the step length.

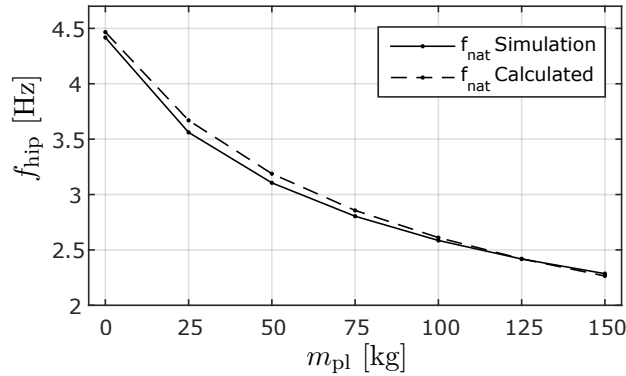


Figure 5.8: First natural frequency  $f_{nat}$  of the simulation model of Cargo depending on the payload. Values out of simulation experiments and calculated using Eq. 5.17.

### 5.3.7 Influence of payload

Cargo is able to run successfully with additional payload between 0 kg and 150 kg. Basic running dynamics (see Section 5.3.2) thereby remain the same for all payloads. In this Section, we analyze the influence of additional payload to efficiency, speed and uniformity of the running locomotion of cargo.

As mentioned earlier, the natural frequency defines the frequency where locomotion with minimum TCOT occurs. This natural frequency can be determined by running a simulation without hip torque input, starting from standstill with the *COM* of the system vertically over the contact point of the foot and the ground. By setting the hip angle to  $\varphi_{hip,rest}$ , the upper body swings passively and the hip angle oscillation corresponds to the natural frequency of the robot.

Since this natural frequency strongly depends on the upper body mass and therefore on the payload, the first step towards variable payload is to develop an estimation of this natural frequency. To do so, we neglect the lower body and assume the upper body to be fixed on a wall at the hip joint. The spring, initially acting between upper and lower body, is acting now between the wall and the upper body. In this configuration, the upper body forms a rotational spring mass system with stiffness  $c$  and inertia  $J_{1pl}$  from Eq. (5.3). The resulting natural frequency can be calculated as:

$$f_{nat} = \frac{1}{2\pi} \sqrt{\frac{c}{J_{1pl}}}. \quad (5.17)$$

The natural frequency per payload predicted by this simplified simulation model is similar to the natural frequency predicted by the complete simulation model (Fig. 5.8), with some deviations at low payloads.

With the calculated natural frequency, the hip torque input parameter search space for each payload is determined as follows:

$$A_{hip} = [0, 1, \dots, 55] \text{ N m} \quad (5.18)$$

and

$$f_{hip}(m_{pl}) = f_{nat}(m_{pl}) \pm 1 \text{ Hz}. \quad (5.19)$$

To explore the influence of payload on Cargo, we conducted simulations for 9 different payloads between 0 and 200 kg. For each payload, simulation and analysis was performed in the same way as described for 100 kg before, within the hip torque parameter space defined by (5.18) and (5.19). As a result, Cargo is able to perform successful running with payloads between 0 and 150 kg. At  $m_{pl} = 175$  kg the forward speed becomes unsteady and therefore no successful

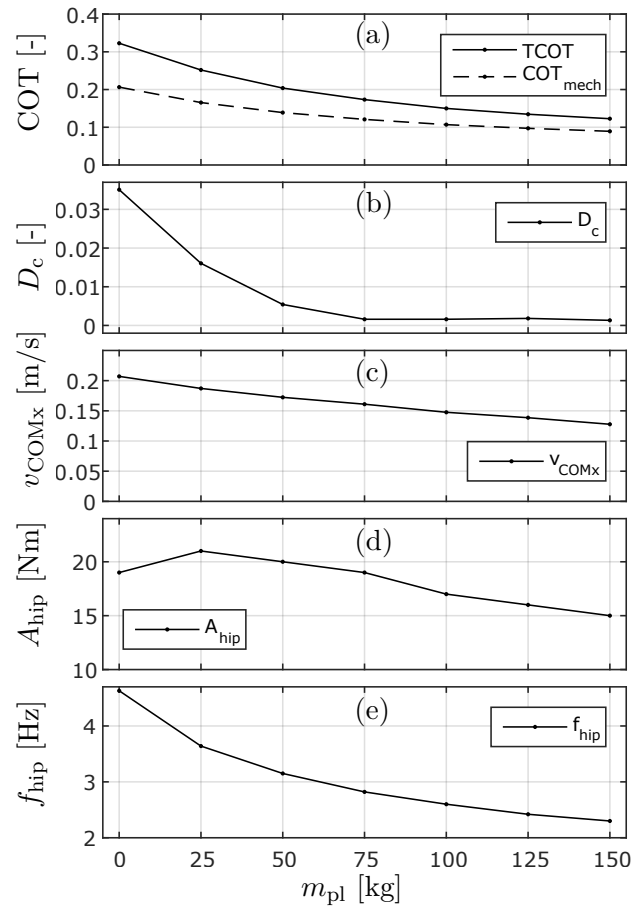


Figure 5.9: Simulated performance of Cargo for payloads between 0 and 150 kg. (a) Minimum total cost of transport  $TCOT_{min}$  per payload. (b) Cyclic deviation  $D_c$  @  $TCOT_{min}$ . (c) Forward speed  $v_{COMx}$  @  $TCOT_{min}$ . (d,e) Amplitude and Frequency @  $TCOT_{min}$ .

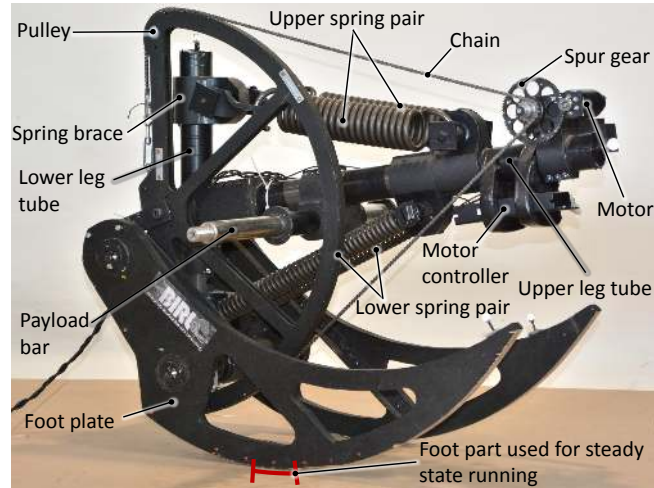


Figure 5.10: Picture of the physical prototype of Cargo used for the experiments. All parameters are similar to the model used for the simulations.

running is possible. For each payload  $m_{pl} \in [0..150]$ kg, the successful running area shows a similar shape as for  $m_{pl} = 100$  kg (see Fig. 5.6) with smooth distribution and minimum TCOT at the left tip of the area and highest  $v_{COMx}$  in the right bottom area. Lower payloads allow larger deviations from the natural frequency for a certain amplitude, therefore the “opening angle” of the successful running area cone becomes larger for lower payloads.

Fig. 5.9 summarizes the  $TCOT_{min}$  for each payload and its corresponding parameters. The  $TCOT_{min}$  (Fig. 5.9a) decreases with increasing  $m_{pl}$  down to its best value of 0.1227 at  $m_{pl} = 150$  kg. The  $COT_{mech}$  decreases with payload as well and the efficiency of the drivetrain (motor, motor controller, gearbox), which can be estimated using  $COT_{mech}/TCOT$ , increases from 0.64 at 0 kg payload to 0.70 at 150 kg.

The corresponding cyclic deviation  $D_c$  (Fig. 5.9b) is low with the exception of 0 and 25 kg payload. At these low payloads, a slow overlaying forward/backward oscillation of the whole robot can be observed which causes the increased  $D_c$ . A similar behavior observed at the physical prototype can be seen in Fig. 5.13a.

The forward speed  $v_{COMx}$  at minimum TCOT for each payload (Fig. 5.9c) is at the same time the minimum possible forward speed for each payload. This speed decreases with increasing payload down to its minimum value of 0.1277 m/s at  $m_{pl} = 150$  kg. The hip torque amplitude (Fig. 5.9d) behaves similar to the forward speed, except for a short increase between 0 and 50 kg payload.

As mentioned earlier, running at minimum TCOT means running near natural frequency. This holds true for all payloads with the frequency at minimum TCOT (Fig. 5.9e) being slightly above the natural frequency at that payload.

## 5.4 Physical platform and data acquisition

We designed a physical platform to verify the simulation results. All parameters are similar similar to the ones of the simulation model (see Tab. 5.1).

### 5.4.1 Experimental platform

The physical platform Cargo (Fig. 5.10) consists of an upper and lower body which are built using a modular system based on 50 mm aluminum tubes and custom aluminum clamping braces for joints, payload, spring attachment and tube connectors. This enables quick adaptation to new geometries without the need for manufacturing new parts. In addition it guarantees for



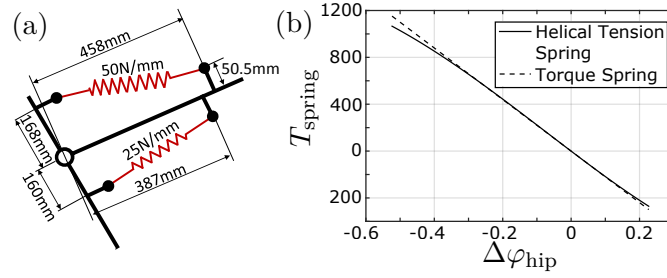


Figure 5.11: (a) Helical tension spring mechanism at the hip of the physical prototype of Cargo. (b) Calculated spring curves for the torsional spring mechanism used for simulations and the helical tension spring mechanism used in the physical prototype.

high stiffness and enables the upper and lower body to be very close to rigid bodies. To avoid frictional losses which occur in a torsional spring setup, we realized the spring on the hip joint by using two helical tension spring pairs instead of a torsional spring (Fig. 5.11a). Within the work range, this setup approximates the torque spring setup with errors less than 2% (Fig. 5.11b). Upper and lower spring were realized as spring pairs and all shafts are supported with ball bearings to further minimize losses.

The two foot plates are designed as circle segments made from 21 mm plywood with a collateral distance of 0.25 m. For convenience and safety, the foot plates are significantly enlarged. During steady state running, only 0.08 m of the sole of the foot has ground contact (see Fig. 5.10). For the payload, we chose commercial weight discs because of their good availability and easy handling. The whole robot was dimensioned to withstand the full tension of the upper springs (7522 N) with a safety margin  $> 2$ .

The two-stage gears of the motor consist of a chain drive (1st stage) and a spur gear (2nd stage) with a total gear reduction of 148. The large wooden chain pulley is rigidly connected to the lower leg to allow the motor to drive the hip joint directly with the spring mechanism being in parallel. In the physical platform, the motor torque  $T_{\text{mot}}$  is sinusoidal, in contrast to the simulation, where the hip torque  $T_{\text{hip}}$  is sinusoidal. Due to the relation shown in Eq. (5.11), a sinusoidal motor torque results in a non-sinusoidal hip torque, depending on whether energy is flowing from the motor to the hip (forward-drive) or the other way around (back-drive). But since back-drive in Cargo occurs usually during less than 10% of the stance time, the hip torque can be approximated using

$$T_{\text{hip}}^* \approx T_{\text{mot}} \cdot \eta_{\text{gear}}, \quad A_{\text{hip}}^* \approx A_{\text{mot}} \cdot \eta_{\text{gear}}. \quad (5.20)$$

## 5.4.2 Data acquisition

The motor of Cargo is torque controlled using the internal current controller provided by the EPOS motor controller. This allows to follow the target current up to 6 Hz with differences lower than 5%. Voltage and current into the EPOS were sampled at 40 kHz to provide information about the electric input power. The sinusoidal input signal for the motor controller was created using two different approaches. For wireless runs on the one hand, we used an on-board computer (Arduino Yun) with a power consumption of 0.1 W. For convenience and measurement purposes on the other hand, we conducted wired runs with the input signal created by a PC using MATLAB. For the calculation of the total input power, the power consumption of the on-board computer was added for both wired and wireless runs.

We used an OptiTrack motion capturing system to capture upper and lower body trajectories of the robot at 125 frames per second. The motion capture data was then used to calculate the generalized coordinates  $q, \dot{q}$  and the forward speed  $v_{\text{COM}_x}$ . For the position data  $q$ , the motion capturing data was used directly without filtering. For the velocity data  $\dot{q}$ , we used a mean

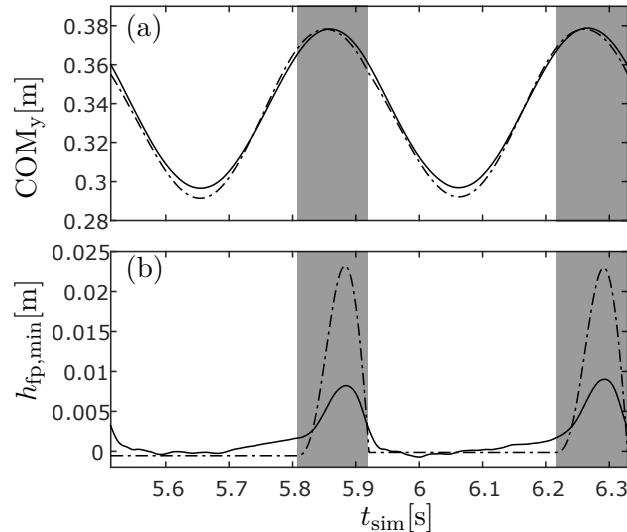


Figure 5.12: Physical (solid) and simulated (dashed) trajectories of the robot COM (a) and the distance between foot and ground (b) for  $m_{\text{pl}} = 100$  kg,  $A_{\text{hip}}^* = 44$  N m,  $f_{\text{hip}} = 2.45$  Hz for two steps.

average filter over five frames.

The motion capturing system is able to detect hopping heights down to 3 mm. To detect smaller hops, we used acoustic feedback since even small hopping heights down to 1 mm lead to an acoustic impact.

All analysis of the physical data is based on the motor controller input, the generalized coordinates and the acoustic impact and was performed in the same way as described in Section 5.3.

## 5.5 Experimental results

We conducted physical runs with Cargo similar to the simulation runs. After starting from standstill by applying the sinusoidal motor torque input, the robot accelerates and stabilizes forward speed after 5 to 7 steps. Due to limitations of the test track, one run consists of 30 motor torque cycles and the last 15 cycles were used for analysis. After extracting the generalized coordinates  $q, \dot{q}$  (see Eq. (5.4)) out of the motion capturing data, we synchronized them with the measured motor controller input power and determined the total cost of transport TCOT (5.16) and the forward speed  $v_{\text{COM}_x}$  in the same way as we did for the simulation data. In addition, the definitions for the successful run (Section 5.3.4) apply to the physical platform in the same way as for the simulation model. We conducted 3 to 5 runs per parameter set to determine mean values and standard deviation.

### 5.5.1 Trajectories and running stability

During successful runs, the physical platform as well as the simulation model show a bouncing motion of the COM, which is typical for spring-mass systems (Fig. 5.12a). In addition, a flight phase can be observed in both cases (Fig. 5.12b). While the bouncing of the COM is similar for physical and simulation experiment, the simulation shows larger swinging around the hip during flight, which leads to larger ground clearance compared to the physical data.

When plotting phase plots of the experimental data (Fig. 5.13), the overall shape and localization within the parameter plane is similar to simulation data with identical parameters. Due to varying ground friction, the cyclic deviation  $D_c$  in the experiment is higher than in simulation. The physical upper body behavior ( $q_4$ ) is well represented by the simulation, while

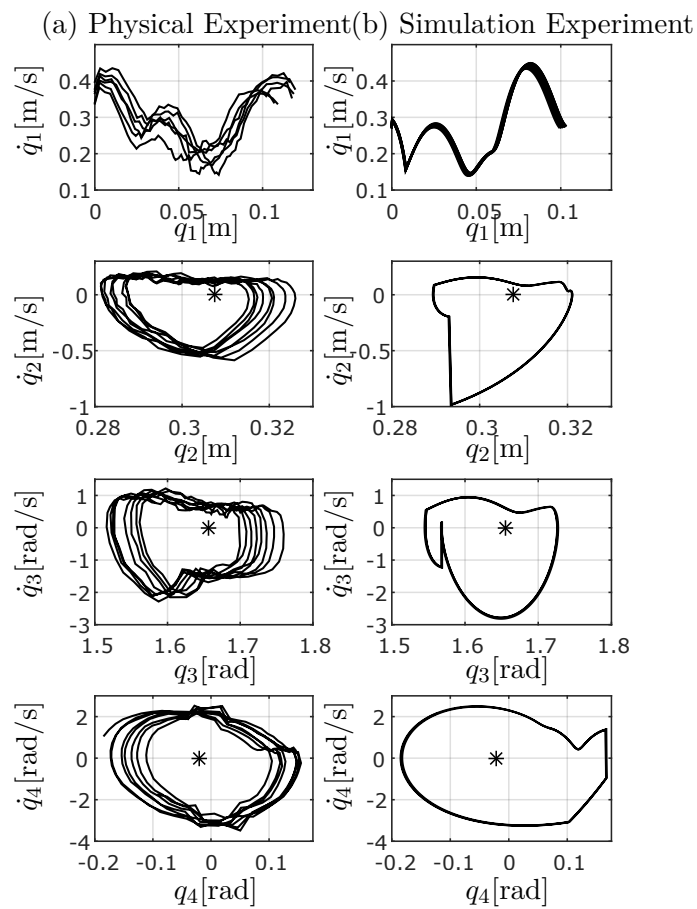


Figure 5.13: Phase plot of the robot state variables  $q, \dot{q}$  for  $m_{pl} = 100$  kg,  $A_{hip}^* = 44$  Nm,  $f_{hip} = 2.45$  Hz. The stable fixed point is indicated with a \*. (a) Physical values for 15 steps with  $D_c = 0.0522$ . (b) Simulation values for 25 steps with  $D_c = 0.0033$ .

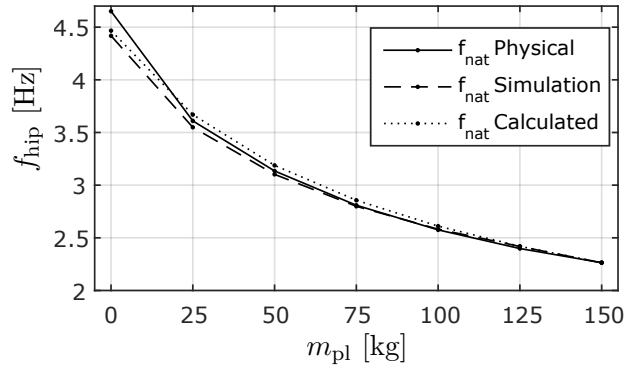


Figure 5.14: First natural frequency  $f_{nat}$  of Cargo depending on the payload for physical and simulation experiment and calculated with Eq. 5.17.

( $q_1$ ) indicates that the touchdown occurs “later” in simulation, i.e. when  $q_1$  is decreasing again. Larger differences occur in the flight phase swinging ( $q_3$ ) and impact behavior ( $q_2$ ) of the lower leg. In contrast to the simulation, the physical drivetrain has some elasticity, a non-ideal current controller and complex losses at low amplitudes, and we assume that this may cause the differences between simulation and experimental  $q_2$  and  $q_3$ . Finally, the plot of  $q_2$  to  $q_4$  shows three similar patterns which are slightly shifted against each other along the x-axis. This represents a forward-backward rocking motion of the whole robot, affecting both upper and lower body.

During all physical experiments, the robot kept track very well, with a deviation to the left/right below 5 cm over a 5 m running distance.

### 5.5.2 Natural frequency

To validate the simulation model, we examined the natural frequency  $f_{nat}$  of the physical platform for different payloads and compared it with the simulation values. The natural frequency is thereby the oscillation of the upper body when standing on the ground. This frequency was measured by swinging up the robot by hand and then let the oscillation die out. The natural frequency of the physical platform thereby shows good match with the simulation data (Fig. 5.14).

### 5.5.3 Energetic characteristics and forward speed effects

In contrast to the simulation, we did not measure through the whole motor input space during the physical experiments. Instead, assuming that the shapes of simulated and physical successful running area are similar, we explored only the lower border of the area where the higher forward speeds are located. For the energetic characteristics and the forward velocity effects, we conducted measurements for five different amplitudes. For each amplitude, we executed various runs through the frequency-range around the lower border of the result plane. Based on this data, we reconstructed the lower border of the successful running area and extracted the minimum TCOT and the according  $v_{COMx}$  from this data.

One basic finding of the simulations was the fact that the minimum TCOT occurs at minimum amplitude and close to natural frequency. This could be confirmed with the experiments (Fig. 5.15a) with 100 kg payload. In addition, the physical TCOT shows the expected increase towards larger hip torque amplitudes and physical and simulation TCOT match well at higher amplitudes. At lower amplitudes, however, the simulation overestimates the TCOT. Another finding from the simulations was that the hip torque amplitude can be used to control the forward speed. The physical platform shows the same behavior (Fig. 5.15b) as forward speed increases with enlarging amplitude. The physical experiment shows higher forward speed per amplitude and the speed difference to the simulation is nearly independent from the amplitude.

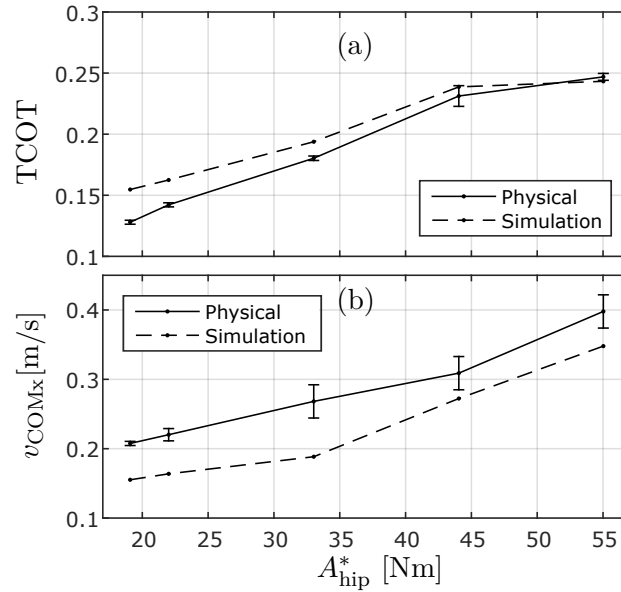


Figure 5.15: (a) Physical and simulated  $\text{TCOT}_{\min}$  of Cargo for hip torque amplitudes between 19 Nm and 55 Nm at  $m_{\text{pl}} = 100$  kg and  $f_{\text{hip}} = [2.58 \ 2.56 \ 2.50 \ 2.45 \ 2.42]$  Hz. (b) Corresponding physical and simulated  $v_{\text{COMx}}$  for  $\text{TCOT}_{\min}$ .

To clarify the underlying reasons for this behavior, future investigations are necessary.

#### 5.5.4 Influence of payload

In simulation, for each payload Cargo shows its best performance near natural frequency and minimum hip torque amplitude (see Section 5.3.7). To find this point in the physical experiment, we slightly varied the hip torque frequency around the previously measured physical natural frequency and executed various runs with increasing amplitude, starting from  $A_{\text{hip}}^* = 10$  Nm. For the analysis, we then considered the run with the lowest hip torque amplitude that has a clearly detectable flight phase for each step. To cover the whole payload range, we repeated this procedure for  $m_{\text{pl}} = [0, 25, 50, 75, 100, 125, 150]$  kg.

The results of the physical experiments for the best performance at different payloads as well as simulation results with identical motor input are shown in Fig. 5.16. Over the whole payload range except for 0, the physical prototype undercut the simulated TCOT by about 0.03. At  $m_{\text{pl}} = 150$  kg, a physical TCOT of 0.0994 was reached. The physical cyclic deviation shows the same decrease with increasing payload as in simulation, although is generally higher. The reason for this is probably the ground friction which slightly varies with each step in the physical experiment. The forward speed in simulation is in average 0.07 m/s lower in simulation when compared to the physical experiment. As a result, the physical platform of Cargo realizes its TCOT per payload at higher input power, compared to simulation. As already indicated for 100 kg payload in Fig. 5.15, the lower forward speed seems to be a universal difference between simulation and physical experiment, and future investigations are necessary to clarify the underlying reasons. While the frequency of simulation and physical experiment fit well, the simulation amplitude shows a slightly larger decrease with increasing payload when compared to the physical data.

## 5.6 Discussion

This chapter introduced the minimalist monopod runner Cargo which is able to set a new benchmark in energy efficient legged locomotion on a level surface. With a TCOT of 0.0994

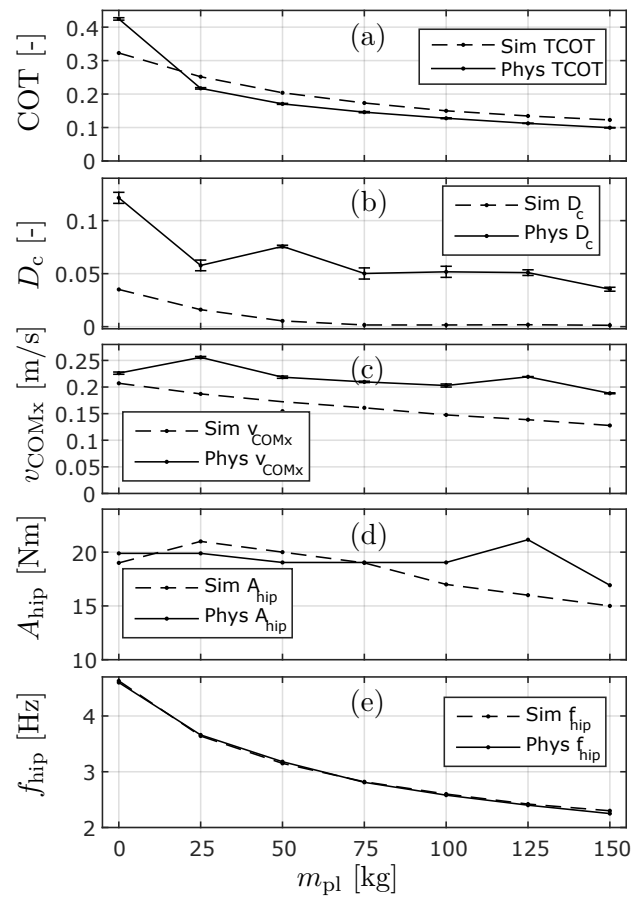


Figure 5.16: Real world performance of Cargo at different payloads between 0 and 150 kg. (a) Minimum total cost of transport  $TCOT_{min}$  per payload. The lowest  $TCOT_{min} = 0.0994$  is reached at  $m_{pl} = 150$  kg. (b) Cyclic deviation  $D_c$  @  $TCOT_{min}$ . (c) Forward speed @  $TCOT_{min}$ . (d,e) Amplitude and Frequency @  $TCOT_{min}$ .

under experimental conditions, it outperforms the most efficient legged robot so far [56] by nearly 100%. When compared to animal walking, Cargo is able to keep up with the most efficient legged animals (African elephants with a TCOT down to 0.11 [12]). Regarding the fact that previous efficient legged robots were bipedal walkers, Cargo presents evidence that running spring mass systems can be very energy efficient too.

Parallel elastic systems allow for powerful actuation at low economic cost (most of the torque is produced by the spring and springs are much cheaper than gearboxes for the same torque) as well as safe operation, since a robot with parallel spring mechanism doesn't collapse if the power is shut down. In addition, parallel elastic actuation provides for body mass support by the springs, so the motor can be used only for energy input, which can lead to better energy efficiency. Profiting from these advantages, cargo demonstrated that the typical drawbacks of PEA, like fixed rest hip angle and the motor inertia adding up to the lower leg inertia [67], can be handled if the robot is designed adequately. Namely, due to low hopping height and low motor inertia, the impact losses remain low, and the mechanical design allows automatic adaption to different payloads and forward speeds regardless of the fixed rest length of the leg. However, a deeper investigation of the advantages of parallel elastic actuation may be beneficial, especially by clarifying if similar results could be achieved with series elastic actuation too.

In Cargo, the parallel hip spring does the large majority of the energy conversion during bouncing, while the motor only inputs positive work to overcome the various losses (see Section 5.3.5). In addition, the spring acts as a mechanical P-controller by pulling the hip back into initial position. Together with the internal damping of hip and gearbox, this system is able to deal with large disturbances like impact or gravitational accelerations. Together with the morphology, this P-controller is able to stabilize the whole gait without any additional feedback. Therefore, Cargo is a good example how purely mechanical feedback can lead to high performance legged robots.

The fact that Cargo can handle different payloads and forward speeds without any adaptations in geometry or spring stiffness and without feedback control is quite remarkable. This ability presumes that the system is able to self-regulate its angular momentum at liftoff and therefore its landing angle at touchdown. This self regulation mechanism can be observed in simulation as well as in experiment. To clarify the properties of this mechanical feedback, further investigations are necessary.

In order to achieve superior energy efficiency, we aimed to reduce the computational power necessary by making use of a self stabilizing mechanical design and use the motor only for energy input in order to compensate for losses. The curved foot is a major contributor to Cargo's ability to self-stabilize and in fact, it even allows for static stabilization during standstill. This static stabilization is caused by the tumbler effect, with the foot radius being larger than the distance between COM and ground. As a result, no sensory feedback is necessary and all high-level computation can be done with an Arduino at very low energy consumption.

Recent work indicates that curved feet may be beneficial for running based on the spring loaded inverted pendulum (SLIP), both in terms of robustness [151, 152] and energy efficiency [151]. However, the behavior was only investigated up to a normalized foot radius of 0.7. Even though Cargo seems to profit from increased robustness and energy efficiency too, for further understanding it is necessary to close the gap in terms of normalized foot radius between actual literature (0.7) and Cargo, which has a normalized foot radius of  $R_{\text{foot}}/L_{\text{leg,rest}}$  of 1.17.

At first sight, Cargo seems to travel most of the distance rolling on its large foot. However, in steady state running, part of the foot disc which is actually used does not exceed 0.078 m in simulation and 0.08 m in physical experiments, respectively. Compared to the leg rest length  $L_{\text{leg,rest}}$  of 0.36 m, the effective foot length is therefore surprisingly short. In addition, the curved foot contributes only marginally to the distance traveled (see Section 5.3.6). The contributions of the curved foot lie rather in increased robustness and probably increased energy efficiency due to reduced impact [151].

## 5.7 Conclusion

This chapter investigated a novel one legged payload carrier that takes advantage of parallel elastic actuation. The system is clock torque controlled, all stabilization is done mechanically. We successfully demonstrated payload transport between 0 and 150 kg and a minimum TCOT below 0.1 under experimental conditions. The mechanics need no adaptation to different payloads, since any corrections can be done by varying torque amplitude and frequency of the hip motor.

At the same body weight and forward speed, Cargo features a way better TCOT than a walking human and outperforms the most efficient legged robot so far [56] by nearly 100%. Therefore, we think that it has the potential to further explore the general minimum TCOT for legged machines. In addition, it is one of the simplest machines that is able to swing its leg forward, and therefore can run freely without external support.





## Chapter 6

# Conclusion and future directions

The aim of this dissertation is to provide a more general understanding of springy dynamics in legged locomotion. Elastic elements like springs can improve energy efficiency, power output and robustness of legged robot locomotion in a similar way as they contribute to animal locomotion. While some applications of springs in legged robots like series elastic actuation are well investigated, others are still not sufficiently understood. Since actuators and muscles show significant differences in terms of inertia and scalability, it is not possible to apply biological principles directly to legged robots. In fact, we believe that an in-depth understanding of all possible interactions between springs, actuators and the robots morphology is necessary to make them successful in legged robots.

### 6.1 Contributions of the dissertation

This dissertation contributes towards a more general understanding of springy dynamics in legged locomotion, by investigating unconventional applications of springs. Two contributions can be identified in this work. The first one is the introduction and investigation of coupling-extended series elastic actuation, which allows for a large variation of springy dynamics in a robotic limb joint. The second contribution investigates another springy dynamic called parallel elastic actuation for robust versatile and energy efficient monopod running.

These two contributions have been investigated in four chapters throughout this dissertation:

**1. Coupling-based series elastic actuation through linear multimodal design:** Conventional series elastic actuators feature one single spring stiffness. Their only way of exhibiting different springy dynamics is the change of their actuator length when mounted on the joint of a segmented leg, which leads to different rest length and, in case of a segmented leg design, different overall spring stiffness of the whole leg. In this dissertation, we have equipped such a series elastic actuator with mechanical couplings which allow for changing the configuration of the spring to enable additional dynamics. In Chapter 2, we have presented an investigation of a physical prototype of such a coupling-extended series elastic actuator (CE-SEA) suitable for actuation in legged robots, whose three couplings allow for nine different dynamics, including passive springy behavior, series elastic actuation, direct actuation and completely passive behavior.

The friction couplings of this actuator allow for coupling at arbitrary positions and are able to dissipate energy while enabling. This eases control and increases reliability, since coupling of parts with arbitrary relative speeds becomes possible. With an opening and closing speed of 200 ms, these clutches are more suitable for single preplanned changes in spring configuration, for example in the transition from manipulation to walking or vice versa. However, in Chapter 2.7 and 2.8, we have demonstrated that the switching is fast enough for continuous, reflex-based operation modes like preloaded hopping.

**2. Improving hopping height control of legged robots by using coupling-based series elastic actuation:** Preloading of a spring is used to amplify actuator power or to insert a defined amount of energy into the system. In Chapter 3 of this dissertation, we have presented a hopping scheme which preloads the spring of the CE-SEA during the flight phase and decouples from the spring during stance phase. In addition, we have used another mode of the CE-SEA, namely the actuator locking mode, to protect the actuator from the high spring forces during stance phase. In contrast to the experiments shown in Chapter 2, here we have equipped the LMMA with ratchet pawl mechanisms instead of friction clutches. The ratchet pawl mechanisms can be realized in a compact and lightweight way, and their fast opening and closing time (down to a few milliseconds with magnetic actuation) makes them suitable for continuous and fast operation, for example for reflex-based actuation patterns like preloaded actuation or actuation with actuator locking.

In simulation and physical experiments we have demonstrated that both preloading and actuator locking allow for higher hopping heights with limited actuator force output. In addition, we have shown that the necessary ratchet pawl mechanisms can be realized at an additional weight which is similar to the additional weight an enlarged SEA suitable for the larger hopping height would have. Or, in other words, the ratchet pawl mechanisms have no disadvantage in weight, but provide the advantage of increased variability in actuator dynamics.

**3. Parallel elasticity for robust and versatile monopod running:** In order to go beyond the bio-inspired regime of series elastic actuation, this dissertation has exploited parallel elastic actuation as an alternative springy dynamic. In Chapter 4, we have showed that parallel elastic actuation allows for robust forward running at a large variation of forward speeds, which has been exploited in the monopod runner CHIARO. By making use of the ability of the parallel elastic mechanism to act as a mechanical P-controller, we have demonstrated that various forward speeds and stride frequencies are achievable without sensory feedback, by using sinusoidal open loop motor torque inputs with only amplitude and frequency as input parameters.

With its minimalist design containing only two rigid bodies, a single spring stiffness at the hip and no sensory feedback, CHIARO represents the opposite of complex biological systems with their highly redundant musculoskeletal design. Beside making use of multiple springy dynamics in a general multi-dynamic setup as illustrated in Chapter 2 and 3, CHIARO demonstrates how important it is to first fully investigate each of these springy dynamics in a specialized platform.

**4. Improved energy efficiency through body mass support in parallel elastic monopod running:** In a parallel elastic setup, the spring can support the body weight of a robot and the motor can be used for loss compensation only. In Chapter 5, we have shown that monopod running with parallel elastic actuation can heavily profit from this weight support and that this approach can show better energy efficiency than any other legged robot.

The topic of load support is an important factor for more complex legged robots too, since most of them spend large amounts of energy even when standing still. Parallel elastic actuation, integrated in a flexible way for example by making use of clutches, can help reduce this energy expenditure by providing passive weight support.

## 6.2 Future research and applications

Future research on springy dynamics in legged robot locomotion could lead towards an universal approach for coupling-based multi-dynamics actuation, unifying a large number of dynamics useful for legged locomotion. Four possible research applications have been identified.

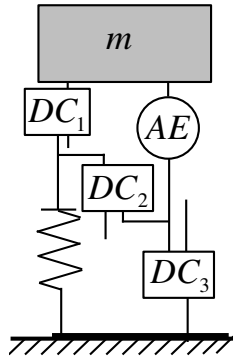


Figure 6.1: Coupling based linear multi-modal actuator which allows for passive, direct, series elastic and parallel elastic drive.

### 6.2.1 Coupling-based multi-dynamics Actuation

This dissertation demonstrated how discrete couplings are able to enlarge the number of dynamics of a series elastic actuator in Chapter 2 and 3. With a slight reconfiguration (Fig. 6.1), the same clutch based actuator is able to perform parallel elastic actuation too. Since parallel elastic actuation can be beneficial in terms of mechanical feedback as shown in Chapter 4 well as for energy efficiency through body weight support as shown in Chapter 5, such a coupling based multi-modal actuator would be the next step to unify all basic springy and non springy dynamics which are relevant for legged locomotion. The second-generation CE-SEA as presented in Chapter 3 is able to produce 70 N m continuous and up to 140 N m peak torque at up to 1.55 rad/s rotational speed at the joint. Compared to conventional high-end SEA's, our CE-SEA is heavier and requires more space. But since Chapter 3 has shown that clutches based on ratchet mechanisms can be realized at similar force to weight ratio than an enlarged actuator, we believe that the disadvantages in weight and volume of the LMMA can be reduced or even neglected with an optimized overall design.

### 6.2.2 Coupling development

Coupling based actuation demands for lightweight, fast, precise and powerful couplings. The ratchet-pawl mechanisms we used in Chapter 3 fulfill these requirements, but they work only in one direction and can close couple only at discrete positions. Friction clutches as used in Chapter 2 work in both directions and offer full flexibility in terms of closing position, but their power density is low and the closing time high. Although a large variety of coupling devices has been investigated so far [82], none of them fulfils all specifications for successful use in high-performance coupling-based actuators. Therefore, one of the major steps towards coupling-based actuation would be the development couplings which are fast, precise, lightweight, powerful, multi-directional and position-independent.

### 6.2.3 Unify series and parallel elastic actuation

In the past, series and parallel elastic actuation have been investigated as an “either-or” approach [67], and to the best of the authors knowledge, no robotic platform features both series and parallel actuation at one joint so far, which would allow for an in-depth comparison under experimental conditions. With the segmented runners CHIARO in Chapter 4 and Cargo in Chapter 5, this dissertation presents a robotic concept which would allow for both, parallel and series elastic actuation. By making use of the same springs used for the parallel setup, preliminary simulations showed that robust running with series elastic actuation is possible too.

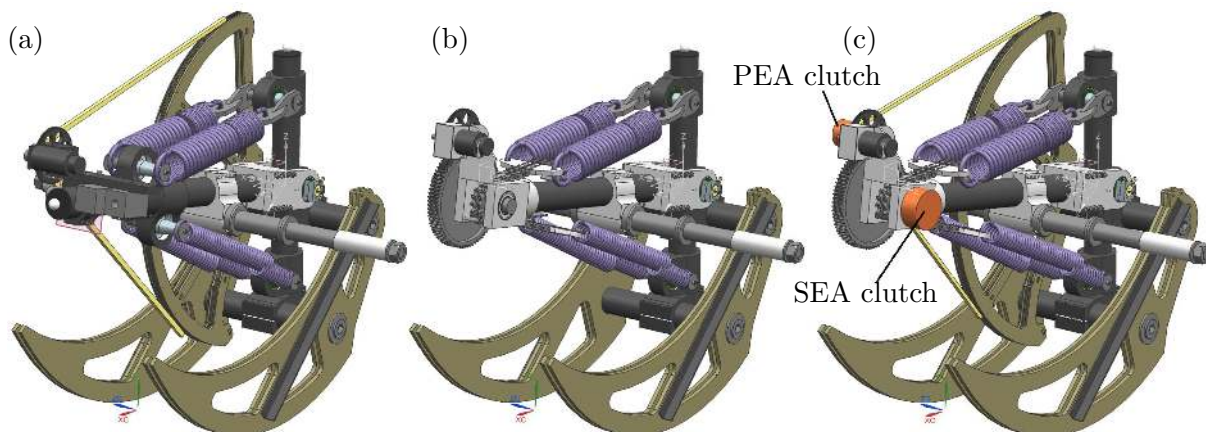


Figure 6.2: Case study for different springy dynamics on Cargo. (a): Parallel elastic configuration, as introduced in Chapter 5. (b): Series elastic configuration, using the same springs as the parallel elastic configuration. One gear stage is added, and the springs are connected with a chain to the gears. (c): Multi-dynamics approach containing series and parallel elastic actuation, as well as two rotary clutches. The PEA clutch either connects either the PEA or the SEA stage of the gearbox with the motor, therefore deciding if cargo is actuated in series or parallel elastic mode. When in parallel elastic mode, the SEA clutch locks the rest length of the spring.

Since Cargo is mainly driven by its passive dynamics, the hopping pattern for series elastic running looks similar to the parallel elastic case, although the energy efficiency seems to be lower at low forward speeds. However, series elastic actuation seems to be advantageous at higher forward speeds.

In terms of mechanical implementation, Fig. 6.2b shows a concept study of Cargo with series elastic drive. By making use of the springs and the first gear stage of the parallel elastic setup, the SEA-Cargo contains two additional gear stages, namely an additional spur gear and finally a chain gear stage leading to the springs. This concept can be extended to coupling-based multi-dynamics actuation shown in Fig. 6.2c. Here parallel drive (6.2a) and serial drive (6.2b) are integrated within the same platform. By making use of two rotary clutches in the first and the second gear stages, this approach is able to switch between parallel elastic actuation (high energy efficiency at low speeds) and series elastic actuation (better energy efficiency at higher speeds).

#### 6.2.4 Complexity Trade-Offs

Springs usually increase the number of mechanical parts and degrees of freedom, and therefore the complexity of the system. Larger complexity usually leads to larger economical costs and larger chances of system failure. In addition, design and understanding of highly complex systems is challenging. From an engineers point of view, a trade-off has to be made between mechanical simplicity (no springs) and performance (springs at the right places).

Legged robots are a young “species” of engineered mobile machines, and like many other examples (cars, planes, ships) showed in the past, most of these species start with low complexity and low performance. For example, the first cars had (if even) very simple suspension, only one gear, no noise reduction, no closed driver cell and no aerodynamic optimization or safety mechanisms whatsoever. Over the decades, the development went on and all these features were added in order to increase the performance. While for the first cars the simplicity-performance trade-off of their time lead to very simple designs, a modern car contains several magnitudes more parts while still representing an optimal trade-off of its time.

From this perspective, it is understandable that today's successful autonomous legged mobile robots have rather simple design. However, we believe that legged robots may face the same development as most other mobile machines, going towards larger complexity and higher performance. In order to master this transition, not only is it necessary to explore and investigate alternative dynamics by making use of springs and clutches. It becomes also inevitable to think about complexity management, may it be through classical approaches like modularization, or using autonomous design and manufacturing, with robots designing and building more complex robots themselves.



## Appendix A

# Comparison between muscles and electric actuation element

This Appendix shows the calculations for Tab. 1.1 in Section 1.1.4. For convenience, the same Table is displayed again as Tab. A.1 in this Appendix. Based on the literature we found, we decided to take the human quadriceps muscle of an average 25 year old male as the reference for a comparison. However, it became necessary to combine the quadriceps data with other literature data for bonobos and starlings in order to gather all the information necessary. Due to the lack of complete datasets for lightweight off-the-shelf servo drives, we decided to design our own based on commonly used electric motors and gearboxes. This enabled us to combine motor and gearbox sizes in a way that weight and output torque become similar to a quadriceps muscle. In the following, each entry of Tab. A.1 is explained in detail.

**Electric actuation element mass** For the comparison, we design an electric actuation element with a performance similar to the quadriceps of a 25 year old male. We consider a combination of a RoboDrive ILM 70x18 motor (Fig. A.1) with a mass of  $m_{\text{motor}} = 0.34$  kg and a HarmonicDrive CPL-32-80-2A (Fig. A.2) with a mass of  $m_{\text{gearbox}} = 0.54$  kg. With the necessary housing, bearings, encoders and power electronics assumed to be twice as heavy as the motor plus the gearbox, we get an electric actuation element mass of:

$$m_{\text{elAE}} = 3 \cdot (m_{\text{motor}} + m_{\text{gearbox}}) = 2.64 \text{ kg.} \quad (\text{A.1})$$

**Muscle mass** For the comparison, we consider the human quadriceps of a 25 year old male [157] with a total weight of

$$m_{\text{muscle}} = \frac{4.49 \text{ kg}}{2} = 2.245 \text{ kg.} \quad (\text{A.2})$$

Table A.1: Typical performance metrics for muscles and electric actuation elements

Parameter	Electric actuation element	Vertebrae muscle
Mass [kg]	2.64	2.245
Continuous power [W/kg]	182	104
Peak power [W/kg]	889	615
Peak torque density [N m/kg]	97	104
Inertia [kg m <sup>2</sup> ]	1.027	0.000917



**Electric actuation element continuous output power** From the data sheet of the ILM 70x18 motor, we can read the maximum continuous torque (where no overheating happens) as  $M_{\text{motor,cont}} = 1.25 \text{ N m}$ . While the output power increases with speed, the motor speed has no influence on the maximum continuous torque. Therefore, we choose the maximum possible speed, which is limited by the gearbox to  $u_{\text{motor,cont}} = 4600 \text{ rpm} = 482 \text{ rad/s}$ . The gearbox efficiency with oil lubrication,  $u_{\text{motor}} > 3500 \text{ rpm}$ , a gear ratio of  $i_{\text{gear}} = 80$  and a gearbox temperature of  $40^\circ \text{C}$  can be determined as  $\eta_{\text{gear}} = 0.8$  (Fig. A.3). With these values, we can calculate the maximum continuous output power as

$$\underline{P}_{\text{elAE,cont}} = \frac{u_{\text{motor,cont}} \cdot M_{\text{motor,cont}} \cdot \eta_{\text{gear}}}{m_{\text{elAE}}} = 182 \text{ W/kg}. \quad (\text{A.3})$$

**Muscle continuous output power** is derived from flying starlings [158] with a continuous power output of

$$\underline{P}_{\text{muscle,cont}} = 104 \text{ W/kg}. \quad (\text{A.4})$$

**Electric actuation element peak output power** The motor can produce a maximum peak torque of  $M_{\text{motor,peak}} = 4 \text{ N m}$ . Again the maximum possible speed is limited by the gearbox to  $u_{\text{motor,peak}} = 7000 \text{ rpm} = 733 \text{ rad/s}$ . The gearbox efficiency is again  $\eta_{\text{gear}} = 0.8$ . With these values, we can calculate the maximum peak output power as

$$\underline{P}_{\text{elAE,peak}} = \frac{u_{\text{motor,peak}} \cdot M_{\text{motor,peak}} \cdot \eta_{\text{gear}}}{m_{\text{elAE}}} = 889 \text{ W/kg}. \quad (\text{A.5})$$

**Muscle peak output power** is derived from jumping bonobos [159] with a peak power output of

$$\underline{P}_{\text{muscle,peak}} = 615 \text{ W/kg}. \quad (\text{A.6})$$

**Electric actuation element peak torque density** With the peak motor torque  $M_{\text{motor,peak}} = 4 \text{ N m}$ , the gearbox efficiency  $\eta_{\text{gear}} = 0.8$ , and the gear ratio of  $i_{\text{gear}} = 80$ , we can determine the peak torque density as:

$$\underline{M}_{\text{elAE,peak}} = \frac{M_{\text{motor,peak}} \cdot \eta_{\text{gear}} \cdot i_{\text{gear}}}{m_{\text{elAE}}} = 97 \text{ N m/kg}. \quad (\text{A.7})$$

**Muscle peak torque density** Isometric peak quadriceps torque of 25 year old males [160] is determined as the average peak torque at  $0$  and  $120^\circ$  knee angle:

$$M_{\text{muscle,peak}} = \frac{262 \text{ N m} + 204 \text{ N m}}{2} = 233 \text{ N m}. \quad (\text{A.8})$$

Together with the quadriceps mass from [157], the resulting torque density is

$$\underline{M}_{\text{muscle,peak}} = \frac{233 \text{ N m}}{2.245 \text{ kg}} = 104 \text{ N m/kg}. \quad (\text{A.9})$$

**Electric actuation element inertia per peak torque** The inertia of the electric actuation element consists of the rotor inertia  $J_{\text{rotor}}$  of the motor, the input inertia of the gearbox  $J_{\text{gearbox}}$ , and the inertia of the connection shaft between rotor and gearbox input, which is assumed to be the same size as the rotor inertia itself. These inertias are finally scaled with the gearbox ratio  $i$ :

$$J_{\text{elAE}} = i^2 \cdot (2 \cdot J_{\text{rotor}} + J_{\text{gearbox}}) = 1.027 \text{ kg m}^2. \quad (\text{A.10})$$

**Muscle inertia per peak torque** The inertia of the quadriceps muscle with one fixed end and the other end changing length is calculated assuming a constant muscle area  $A_{\text{muscle}}$  and muscle density  $\rho_{\text{muscle}}$  over muscle length  $L = 1$ :

$$J_{\text{muscle,lin}} = \rho_{\text{muscle}} \int_0^L A_{\text{muscle}} \cdot l^2 dl = \frac{\rho_{\text{muscle}}}{3} [A_{\text{muscle}} \cdot l^3]_0^{L=1} = \frac{1}{3} \rho_{\text{muscle}} \cdot A_{\text{muscle}} \cdot L = \frac{1}{3} m_{\text{muscle}}. \quad (\text{A.11})$$

With a quadriceps lever at the knee of  $s_{\text{muscle}} = 0.035$  m [161], the rotational inertia of the quadriceps around the knee joint can be determined as

$$J_{\text{muscle,rot}} = s_{\text{muscle}}^2 \cdot J_{\text{muscle,lin}} = 0.000\,917 \text{ kg m}^2. \quad (\text{A.12})$$




---

## Servo kits ILM

**Structural integrated drive engineering leading to highest power density by maximum degree of freedom in design**

With the stator-rotor installation kits of the ILM series RoboDrive offers solutions for structurally integrated drive engineering. The RoboDrive technology provides the highest power density at maximum torque range and overload capability in a compact design. The flexible concept offers solutions for a variety of demanding drive applications. On request alternative voltage levels and customized torque-speed characteristics can be realized.

The implementation of customer-specific solutions to achieve a compact and thermally optimized design is supported by detailed documentation, engineering services based on the RoboDrive-development expertise.




**Key features:**

- Frameless motors for highest design flexibility
- Hollow-shaft capability
- Low voltage 12 V - 48 V
- Highest torque density and dynamics due to excellent copper fill factor
- Redundant windings available
- Low thermal losses by concentrated coils
- Thermally optimized actuator design by structural integration and thermally conductive epoxy casting
- Weight and installation space optimized drive system design based on load-profile analysis
- High control quality by high bandwidth and lowest harmonics

**Basic data**

	ILM 25x 04	ILM 25x 08	ILM 38x 06	ILM 38x 12	ILM 50x 08	ILM 50x 14	ILM 70x 10	ILM 70x 18	ILM 85x 04	ILM 85x 13	ILM 85x 23	ILM 85x 26	ILM 115x 25	ILM 115x 50
Power P [W]	60	60	95	165	155	180	270	275	405	430	410	410	735	760
Rated torque $T_r^*$ [Nm]	0.024	0.048	0.1	0.2	0.27	0.5	0.74	1.25	0.43	1.43	2.3	2.6	5.4	11.2
Peak torque $T_{max}$ at 20% deviation from linearity [Nm]	0.1	0.2	0.4	0.7	0.9	1.4	2.3	4	1.2	4.5	7.3	8.3	12.2	40
Rotation speed $n_{max}^{**}$ at $U_r$ [rpm]	24,000	12,000	9,000	8,000	5,500	3,500	3,500	2,100	9,000	2,900	1,700	1,500	1,300	650
Diameter D [mm]	25	25	38	38	50	50	69	69	85	85	85	85	115	115
Length L [mm]	10.8	15.2	15.3	22.3	16.4	22.8	22.6	30.5	17.6	27.2	37.2	40.7	39	68.4
Weight m [g]	16	29	52	86	86	135	230	340	200	370	550	590	1,200	2,170
Rotor inertia J [kgcm <sup>2</sup> ]	0.0023	0.004	0.01	0.02	0.049	0.086	0.21	0.34	0.28	0.61	0.98	1.15	3.65	7.90

\* When installed in aluminum, highly dependent on installation situation. Nominal operational temperature of the stator: -40°C to 125°C.  
\*\* Theoretical no-load rotation speeds at  $U_r$ . Variations can arise from operation with different inverters. Higher rotation speeds or change of the voltage level can be achieved by adapting the interconnection scheme.

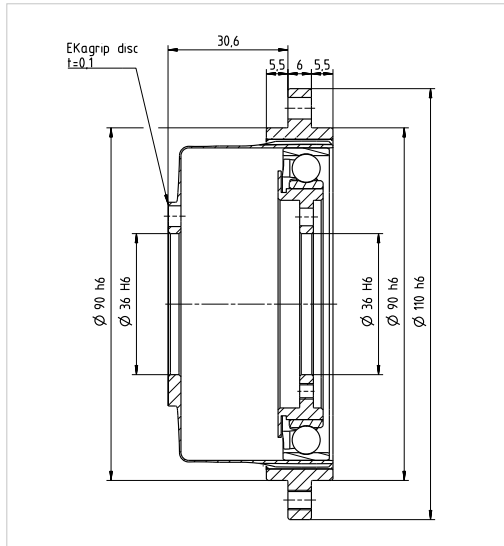
Figure A.1: Technical data of the RoboDrive ILM 70x18 motor. Copyright TQ-Systems GmbH, 2016

Table 12.1

	Unit	CPL-32-2A					
		30	50	80	100	120	160
Ratio	$i$ [ ]	30	50	80	100	120	160
Repeatable peak torque	$T_{R}$ [Nm]	100	216	304	333	353	372
Average torque	$T_{A}$ [Nm]	75	108	167	216	216	216
Rated torque	$T_{N}$ [Nm]	54	76	118	137	137	137
Momentary peak torque	$T_{M}$ [Nm]	200	382	568	647	686	686
Maximum input speed (oil lubrication)	$n_{in(max)}$ [rpm]	7000					
Maximum input speed (grease lubrication)	$n_{in(max)}$ [rpm]	4800					
Average input speed (oil lubrication)	$n_{av(max)}$ [rpm]	4600					
Average input speed (grease lubrication)	$n_{av(max)}$ [rpm]	3500					
Moment of inertia	$J_m$ [ $\times 10^{-4}$ kgm <sup>2</sup> ]	0.924					
Weight	$m$ [kg]	0.54					

Illustration 12.2

CPL-32-2A [mm]



QUICKLINK [www.harmonicdrive.de/CAD3030](http://www.harmonicdrive.de/CAD3030)

4.3.2 Efficiency Tables

Tables Oil

Efficiency for Oil Lubrication at Rated Torque.

Illustration 25.1

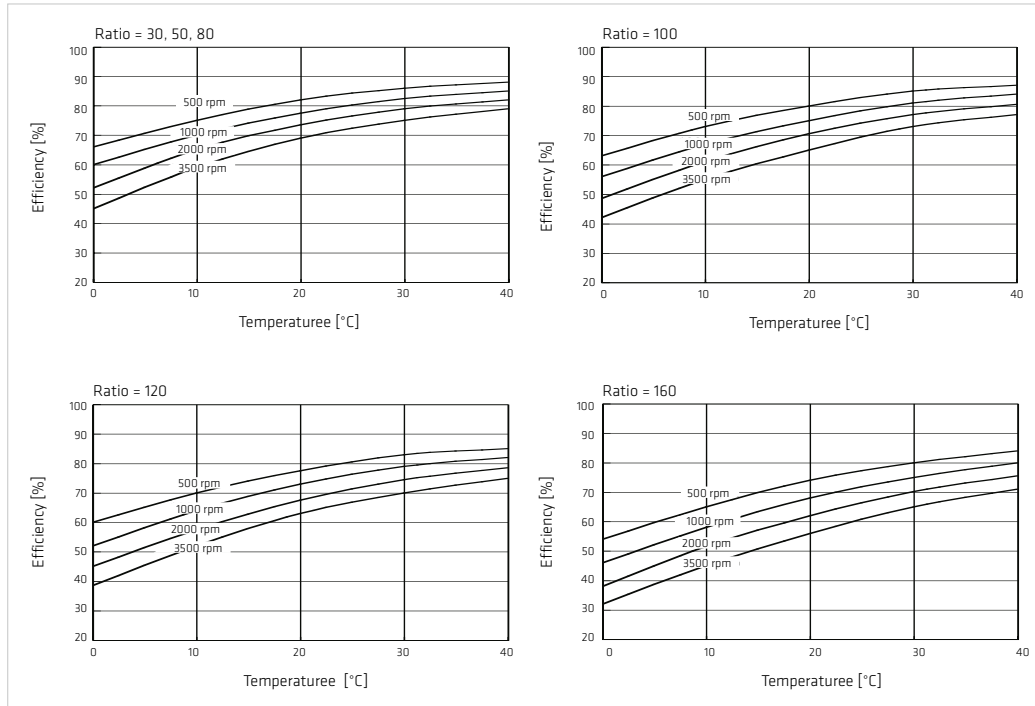


Figure A.3: Efficiency for HarmonicDrive gearboxes. Copyright HarmonicDrive AG, 2016

# Bibliography

- [1] D. Leach, F. Günther, N. Maheshwari, and F. Iida. Linear multimodal actuation through discrete coupling. *IEEE/ASME Transactions on Mechatronics*, 19(3):827–839, 2014.
- [2] F. Günther and F. Iida. Preloaded hopping with linear multi-modal actuation. In *Proc. 2013 IEEE/RSJ Int. Conf. Intelligent Robots and Systems (IROS)*, pages 5847–5852, Tokyo, Japan, 2013.
- [3] F. Guenther, H.Q. Vu, and F. Iida. Improving hopping height control of legged robots by using coupling-based series elastic actuation. *Conditionally accepted for publication in IEEE Transactions on Robotics*.
- [4] F. Günther, F. Giardina, and F. Iida. Self-stable one-legged hopping using a curved foot. In *Proc. 2014 IEEE Int. Conf. Robotics and Automation (ICRA)*, pages 5133–5138, Hong Kong, China, 2014.
- [5] F. Guenther and F. Iida. Energy efficient monopod running with large payload based on open loop parallel elastic actuation. *Accepted for publication in IEEE Transactions on Robotics*.
- [6] F. Günther, Y. Shu, and F. Iida. Parallel elastic actuation for efficient large payload locomotion. In *Proc. 2015 IEEE Int. Conf. Robotics and Automation (ICRA)*, pages 823–828, Seattle, WA, 2015.
- [7] R.McN. Alexander. Tendon elasticity and muscle function. *Comparative Biochemistry*, 133:1001–1011, 2002.
- [8] T.J. Roberts and E. Azizi. Flexible mechanisms: the diverse roles of biological springs in vertebrate movement. *The Journal of Experimental Biology*, 214:353–361, 2011.
- [9] G.A. Lichtwark and A.M. Wilson. Is achilles tendon compliance optimised for maximum muscle efficiency during locomotion? *Journal of Biomechanics*, 40:1768–1775, 2007.
- [10] M.H Raibert, H.B. Brown Jr., M. Chepponis, E. Hastings, S.E. Shreve, and F.C. Wimberly. Dynamically stable legged locomotion research. Technical report, Carnegie Mellon University, 1981.
- [11] X Zhou and S. Bi. A survey of bio-inspired compliant legged robot designs. *Bioinspir. Biomim.*, 7(4):1–20, 2012.
- [12] V.A. Langman, M.F. Rowe, T.J. Roberts, N.V. Langman, and C.R. Taylor. Minimum cost of transport in asian elephants: do we really need a bigger elephant? *The Journal of Experimental Biology*, 215:1509–1514, 2012.
- [13] T.V. Dailey and N.T. Hobbs. Travel in alpine terrain: energy expenditures for locomotion by mountain goats and bighorn sheep. *Canadian Journal of Zoology*, 67:2368–2375, 1989.

## BIBLIOGRAPHY

- [14] K.D. Hunt, J.G.H. Cant, D.L. Gebo, M.D. Rose, S.E. Walker, and D. Youlatos. Standardized descriptions of primate locomotor and postural modes. *Primates*, 37(4):363–387, 1996.
- [15] A.M. Wilson, J.C. Lowe, K. Roskilly, P.E. Hudson, K.A. Golabek, and J.W. McNutt. Locomotion dynamics of hunting in wild cheetahs. *Nature*, 498:185–189, 2013.
- [16] G.A. Cavagna, N.C. Heglund, and C.R. Taylor. Mechanical work in terrestrial locomotion: two basic mechanisms for minimizing energy expenditure. *American Journal of Physiology*, 233(5):R243–R261, 1977.
- [17] T.J. Roberts. The integrated function of muscles and tendons during locomotion. *Comparative Biochemistry and Physiology - Part A: Molecular & Integrative Physiology*, 133(4):1087–1099, 2002.
- [18] A.A. Biewener. Muscle-tendon stresses and elastic energy storage during locomotion in the horse. *Comparative Biochemistry and Physiology Part B*, 120:73–87, 1998.
- [19] R.I. Griffiths. The mechanics of the medial gastrocnemius muscle in the freely hopping wallaby (*thylogale billardieri*). *Journal of experimental Biology*, 147:439–456, 1989.
- [20] A. Lai, A.G. Schache, Y.C. Lin, and M.G. Pandy. Tendon elastic strain energy in the human ankle planar-flexors and its role with increased running speed. *The Journal of Experimental Biology*, 217:3159–3168, 2014.
- [21] G.A. Lichtwark. A catapult action for rapid limb protraction. *Nature*, 421:35–36, 2003.
- [22] W. Gronenberg. Fast actions in small animals: springs and click mechanisms. *The Journal of Comparative Physiology*, 178:727–734, 1996.
- [23] T.J. Roberts and E. Azizi. The series-elastic shock absorber: tendons attenuate muscle power during eccentric actions. *Journal of Applied Physiology*, 109:396–404, 2010.
- [24] N. Konow and T.J. Roberts. The series elastic shock absorber: tendon elasticity modulates energy dissipation by muscle during burst deceleration. *Proceedings of the Royal Society of London B: Biological Sciences*, 282, 2015.
- [25] H. Higuchi and Y. Umazume. Localization of the parallel elastic components in frog skinned muscle fibers studied by the dissociation of the a- and i-bands. *Journal of Biophysics*, 48:137–147, 1985.
- [26] H.L. Granzier and T.C. Irving. Passive tension in cardiac muscle: Contribution of collagen, titin, microtubules, and intermediate filaments. *Biophysical Journal*, 68:1027–1044, 1995.
- [27] L. Tskhovrebova, J. Trinick, J.A. Sleep, and R.M. Simmons. Elasticity and unfolding of single molecules of the giant muscle protein titin. *Nature*, 387:308–312, 1997.
- [28] A.V. Hill. The heat of shortening and the dynamic constant of muscle. *Proceedings of the Royal Society of London B: Biological Sciences*, 126(843):136–195, 1938.
- [29] R.McN. Alexander. Three uses for springs in legged locomotion. *The International Journal of Robotics Research*, 9(2):53–61, April 1990.
- [30] D. Dyjre-Poulsen, H.H. Smedegaard, J. Roed, and E. Korsgaard. Equine hoof function investigated by pressure transducers inside the hoof and accelerometers mounted on the first phalanx. *Equine Veterinary Journal*, 26(5):362–366, 1995.

- [31] M.B. Bennett and R.F. Ker. The mechanical properties of the human subcalcaneal fat pad in compression. *Journal of Anatomy*, 171:131–138, 1990.
- [32] J.R. Ralphs and M. Benjamin. The joint capsule: structure, composition, ageing and disease. *Journal of Anatomy*, 184:503–509, 1994.
- [33] D.T. Harryman, J.A. Sidles, S.L. Harris, F.A. Matsen, and S. Washington. The role of the rotator interval capsule in passive motion and stability of the shoulder. *Journal of Bone and Joint Surgery*, 74(A):53–66, 1992.
- [34] B. Brown and G. Zeglin. The bow leg hopping robot. In *Proc. 1998 IEEE Int. Conf. Robotics & Automation (ICRA)*, pages 781–786, Leuven, Belgium, 1998.
- [35] R. Altendorfer, N. Moore, H. Komsuoglu, M. Buehler, H.B. Brown Jr, D. McMordie, U. Saranli, R. Full, and D. Koditschek. Rhex: A biologically inspired hexapod runner. *Autonomous Robots*, 11:207–213, 2001.
- [36] T McGeer. Principles of walking and running. In *Mechanics of animal locomotion. Advances in comparative and environmental physiology 11*, pages 114–140, Heidelberg, Germany, 1992.
- [37] M.H. Raibert. *Legged Robots That Balance*. Massachusetts Institute of Technology, Cambridge, MA, USA, 1986.
- [38] M. Ahmadi and M. Buehler. Stable control of a simulated one-legged running robot with hip and leg compliance. *IEEE Transactions on Robotics and Automation*, 13(1):96–104, 1997.
- [39] A. Ramzani, J.W. Hurst, K.A. Hamed, and J.W. Grizzle. Performance analysis and feedback control of atrias, a three-dimensional bipedal robot. *Journal of Dynamic Systems, Measurement, and Control*, 136:1–12, 2014.
- [40] I. Poulakakis, J.A. Smith, and M. Buehler. Modeling and experiments of untethered quadrupedal running with a bounding gait: The scout ii robot. *International Journal of Robotics Research*, 24(4):239–256, 2005.
- [41] M. Hutter, C.D. Remy, M.A. Hoepflinger, and R. Siegwart. Efficient and versatile locomotion with highly compliant legs. *IEEE/ASME Transactions on Mechatronics*, 18(2):449–458, 2013.
- [42] G. A. Folkertsma, S. Kim, and S. Stramigioli. Parallel stiffness in a bounding quadruped with flexible spine. In *Proc. 2012 IEEE/RSJ Int. Conf. Intelligent Robots and Systems (IROS)*, pages 2210–2215, Algarve, Portugal, 2012.
- [43] U. Scarfogliero, C. Stefanini, and P. Dario. Design and development of the long-jumping ”grillo” mini robot. In *Proc. 2007 IEEE Int. Conf. Robotics and Automation (ICRA)*, pages 467–472, Rome, Italy, 2007.
- [44] M. Kovac, M. Schlegel, J.C. Zufferey, and D. Floreano. Steerable miniature jumping robot. *Autonomous Robots*, 28(3):295–306, 2006.
- [45] Q.V. Nguyen and H.C. Park. Design and demonstration of a locust-like jumping mechanism for small-scale robots. *Journal of Bionic Engineering*, 9(3):271–281, 2012.
- [46] S. Cotton, Mihai. I., C. Olaru, M. Bellman, T. Van der Ven, J. Godowski, and J Pratt. Fastrunner: A fast, efficient and robust bipedal robot. concept and planar simulation. In *Proc. 2012 IEEE Int. Conf. Robotics and Automation (ICRA)*, pages 2358–2364, Saint Paul, MN, 2012.



## BIBLIOGRAPHY

- [47] R.J. Full and D.E. Koditschek. Templates and anchors: Neuromechanical hypotheses of legged locomotion on land. *The Journal of Experimental Biology*, 202:3325–3332, 1999.
- [48] R. Blickhan. The spring-mass model for running and hopping. *Journal of Biomechanics*, 22(11/12):1217–1227, 1989.
- [49] T.A. McMahon and G.C. Cheng. The mechanics of running: How does stiffness couple with speed? *Journal of Biomechanics*, 23(1):65–78, 1990.
- [50] S. Mochon and T.A. McMahon. Ballistic walking. *Journal of Biomechanics*, 13:49–57, 1980.
- [51] T. McGeer. Passive dynamic walking. *The International Journal of Robotics Research*, 9(2):62–82, 1990.
- [52] R. Altendorfer, D. Koditschek, and P. Holmes. Stability analysis of legged locomotion models by symmetry-factored return maps. *The International Journal of Robotics Research*, 23(10-11):979–999, 2004.
- [53] H. Celik and S.J. Piazza. Simulation of aperiodic bipedal sprinting. *Journal of Biomechanical Engineering*, 135:1–8, 2013.
- [54] H. Geyer, A. Seyfarth, and R. Blickhan. Compliant leg behaviour explains basic dynamics of walking and running. *Proceedings of the Royal Society B: Biological Sciences*, 232:315–328, 2006.
- [55] T. McGeer. Passive bipedal running. *Proceedings of the Royal Society of London B: Biological Sciences*, 240(1297):107–134, 1990.
- [56] P.A. Bhounsule, J. Cortell, and A. Ruina. Design and control of ranger: An energy efficient, dynamic walking robot. In *Proc. 15th Int. Conf. Climbing and Walking Robots (CLAWAR 2012)*, pages 441–448, Baltimore, MD, 2012.
- [57] S.H. Collins, A. Ruina, R. Tedrake, and M. Wisse. Efficient bipedal robots based on passive-dynamic walkers. *Science*, 307:1082–1085, 2005.
- [58] A.D. Kuo. Choosing your steps carefully. *IEEE Robotics and Automation Magazine*, 14(2):18–29, 2007.
- [59] S. Seok, A. Wang, D. Otten, and S. Kim. Actuator design for high force proprioceptive control in fast legged locomotion. In *Proc. 2012 IEEE/RSJ Int. Conf. Intelligent Robots and Systems (IROS)*, pages 1970–1975, Algarve, Portugal, 2012.
- [60] B. Feinstein, B. Lindegaard, E. Nyman, and G. Wohlfart. Morphologic studies of motor units in normal human muscles. *Acta Anatomica (Basel)*, 23:127–142, 1955.
- [61] G.A. Pratt and M.M. Williamson. Series elastic actuators. In *Proc. 1995 IEEE/RSJ Int. Conf. Intelligent Robotics and Systems (IROS)*, pages 399–406, Pittsburgh, PA, 1995.
- [62] J. Pratt, B. Krupp, and C. Morse. Series elastic actuators for high fidelity force control. *Industrial Robot: An International Journal*, 29(3):234–241, 2002.
- [63] N. Paine, S. Oh, and L. Sentis. Design and control considerations for high-performance series elastic actuators. *IEEE/ASME Transactions on Mechatronics*, 19(3):1080–1091, 2014.

- [64] M. Laffranchi, N.G. Tsagarakis, F. Cannella, and D.G. Caldwell. Antagonistic and series elastic actuators: a comparative analysis on the energy consumption. In *Proc. 2009 IEEE/RSJ Int. Conf. Intelligent Robots and Systems (IROS)*, pages 5678–5684, St. Louis, USA, 2009.
- [65] Ernesto Carlos Martinez-Villalpando. *Design and Evaluation of a Biomimetic Agonist-Antagonist Active Knee Prosthesis*. PhD thesis, Massachusetts Institute of Technology, 2012.
- [66] T. Yano, J.H. Lee, and S. Okamoto. Walking experiment of biped robot with antagonistic actuation using non-linear spring. In *Proc. 2016 Int. MultiConf. Engineers and Computer Scientists (IMECS)*, 2016.
- [67] Y. Yesilevskiy, W. Xi, and C.D. Remy. A comparison of series and parallel elasticity in a monopod hopper. In *Proc. 2015 IEEE Int. Conf. Robotics and Automation (ICRA)*, pages 1036–1041, Seattle, WA, 2015.
- [68] S. Shirata, A. Konno, and M. Uchiyama. Design and evaluation of a gravity compensation mechanism for a humanoid robot. In *Proc. 2007 IEEE/RSJ Int. Conf. Intelligent Robots and Systems (IROS)*, page 3635–3640, 2007.
- [69] R.McN. Alexander, N.J. Dimery, and K.F. Ker. Elastic structures in the back and their role in galloping in some mammals. *Journal of Zoology*, 207:467–482, 1985.
- [70] M. Khoramshahi, A. Parsa, A. Ijspeert, and M.N. Ahmadabadi. Natural dynamics modification for energy efficiency: A data-driven parallel compliance design method. In *Proc. 2014 IEEE Int. Conf. Robotics and Automation (ICRA)*, pages 2412–2417, Hong Kong, China, 2014.
- [71] U. Mettin, P.X. LaHera, L.B. Freidovich, and A.S. Shiriaev. Parallel elastic actuators as a control tool for preplanned trajectories of underactuated mechanical systems. *The International Journal of Robotics Research*, 29(9):1186–1198, 2010.
- [72] M. Reis and F. Iida. An energy efficient hopping robot based on free vibration of a curved beam. *IEEE Transactions on Mechatronics*, 19(1):300–311, 2014.
- [73] X. Liu and I. Poulakakis. On the energetics of a switchable parallel elastic actuator design for monopodal running. In *Proc. 2015 IEEE Int. Conf. Robotics and Biomimetics (ROBIO)*, pages 769–774, Zhuhai, China, 2015.
- [74] D. Robinson. *Design and analysis of series elasticity in closed-loop actuator force control*. PhD thesis, Massachusetts Institute of Technology, Cambridge, MA, 2000.
- [75] J. Rummel and A. Seyfarth. Stable running with segmented legs. *The International Journal of Robotics Research*, 27(8):919–934, 2008.
- [76] Y. Zhang, J. Luo, K Hauser, H.A. Park, M. Paldhe, C.S.G. Lee, R. Ellenberg, B. Killen, P. Oh, J.H. Oh, J. Lee, and I. Kim. Motion planning and control of ladder climbing on drc-hubo for darpa robotics challenge. In *Proc. 2014 IEEE Int. Conf. Robotics & Automation (ICRA)*, page 2086, Hong Kong, China, 2014.
- [77] M. Hutter. *StarLETH & Co. Design and Control of Legged Robots with Compliant Actuation*. PhD thesis, ETH Zurich, 2013.
- [78] B. Vanderborght, Albu-Schaeffer, A. A. Bicchi, E. Burdet, D.G. Caldwell, R. Carloni, M. Catalano, O. Eiberger, W. Friedl, G. Ganeshd, M. Garabini, M. Grebenstein, G. Grioli, S. Haddadina, H. Hoppnera, A. Jafari, M. Laffranchi, D. Lefeber, F. Petit, S. Stramigioli, N. Tsagarakis, M. Van Damme, R. Van Ham, L.C. Visser, and Wolf S. Variable impedance actuators: A review. *Robotics and Autonomous Systems*, 61:1601–1614, 2013.

## BIBLIOGRAPHY

- [79] C.T. Farley, J. Gasheen, and T.A. McMahon. Running springs: Speed and animal size. *The Journal of Experimental Biology*, 185:71–86, 1993.
- [80] T.J. Roberts and R.L. Marsh. Probing the limits to muscle-powered accelerations: lessons from jumping bullfrogs. *The Journal of Experimental Biology*, 206:2567–2580, 2003.
- [81] A.A. Biewener and R. Blickhan. Kangaroo rat locomotion: design for elastic energy storage or acceleration? *Journal of experimental Biology*, 140:243–255, 1988.
- [82] M. Plooij, G. Mathijssen, P. Cherelle, D. Lefeber, and B. Vanderborght. Lock your robot: A review of locking devices in robotics. *IEEE Robotics & Automation Magazine*, 22(1):106–117, 2015.
- [83] B. Li, Q. Deng, and Liu Z. A spherical hopping robot for exploration in complex environments. In *Proc. 2009 IEEE Int. Conf. Robotics and Biomimetics (ROBIO)*, pages 402–407, Guilin, China, 2009.
- [84] S.H. Collins and A. Ruina. A bipedal walking robot with efficient and human-like gait. In *Proc. 2005 IEEE Int. Conf. Robotics and Automation (ICRA)*, pages 1983–1988, Barcelona, Spain, 2005.
- [85] H. Wang, Y.F. Zheng, Y. Jun, and P. Oh. Drc-hubo walking on rough terrains. In *Proc. IEEE Int. Conf. Technologies for Practical Robot Applications (TePRA)*, pages 1–6, Woburn, MA, 2014.
- [86] M. Ahmadi and M. Buehler. Controlled passive dynamic running experiments with the arl-monopod ii. *IEEE Transactions on Robotics*, 22(5):974–986, 2006.
- [87] M.A. Daley and J.R. Usherwood. Two explanations for the compliant running paradox: reduced work of bouncing viscera and increased stability in uneven terrain. *Biology Letters*, 6(3):418–421, 2010.
- [88] N. Hogan. Impedance control: An approach to manipulation. In *American Control Conference*, pages 304–313, San Diego, CA, USA, 1984.
- [89] G. Zeng and A. Hemami. An overview of robot force control. *Robotica*, 15(5):473–482, 1997.
- [90] M. Zinn, O. Khatib, B. Roth, and J.K. Salisbury. Playing it safe [human-friendly robots]. *Robotics Automation Magazine, IEEE*, 11(2):12–21, June 2004.
- [91] C.M. Thompson and M.H. Raibert. Passive dynamic running. In V. Hayward and O. Khatib, editors, *Experimental Robotics I*, volume 139 of *Lecture Notes in Control and Information Sciences*, pages 74–83. Springer Berlin / Heidelberg, 1990.
- [92] D. Paluska and H. Herr. The effect of series elasticity on actuator power and work output: Implications for robotic and prosthetic joint design. *Robotics and Autonomous Systems*, 54(8):667–673, 2006.
- [93] F. Iida, J. Rummel, and A. Seyfarth. Bipedal walking and running with spring-like biarticular muscles. *Journal of Biomechanics*, 41(3):656–667, 2008.
- [94] A. Seyfarth, F. Iida, R. Tausch, M. Stelzer, O. von Stryk, and A. Karguth. Towards bipedal jogging as a natural result of optimizing walking speed for passively compliant three-segmented legs. *The International Journal of Robotics Research*, 28(2):257–265, 2009.

- [95] B.Y. Yi, J.H. Lee, W.K. Kim, and I.H. Suh. Design of multi-degree-of-freedom spring mechanisms: biomimetic approach. In *Proc. 2000 IEEE/RSJ Int. Conf. Intelligent Robots and Systems (IROS)*, volume 3, Takamatsu, Japan, October 2000.
- [96] G. Tonietti, R. Schiavi, and A. Bicchi. Design and control of a variable stiffness actuator for safe and fast physical human/robot interaction. In *Proc. 2005 IEEE Int. Conf. Robotics and Automation (ICRA)*, pages 526–531, Barcelona, Spain, April 2005.
- [97] R. Schiavi, G. Grioli, S. Sen, and A. Bicchi. Vsa-ii: a novel prototype of variable stiffness actuator for safe and performing robots interacting with humans. In *IEEE International Conference on Robotics and Automation (ICRA)*, pages 2171–2176, Pasadena, CA, May 2008.
- [98] A. Jafari, N.G. Tsagarakis, B. Vanderborght, and D.G. Caldwell. A novel actuator with adjustable stiffness (awas). In *Proc. 2010 IEEE/RSJ Int. Conf. Intelligent Robots and Systems (IROS)*, pages 4201–4206, Taipei, Taiwan, October 2010.
- [99] J. Choi, S. Hong, W. Lee, S. Kang, and M. Kim. A robot joint with variable stiffness using leaf springs. *IEEE Transactions on Robotics*, 27(2):229–238, April 2011.
- [100] B.S. Kim, J.B. Song, and J.J. Park. A serial-type dual actuator unit with planetary gear train: Basic design and applications. *IEEE/ASME Transactions on Mechatronics*, 15(1):108–116, February 2010.
- [101] R. Van Ham, B. Vanderborght, M. Van Damme, B. Verrelst, and D. Lefeber. Maccepa, the mechanically adjustable compliance and controllable equilibrium position actuator: Design and implementation in a biped robot. *Robotics and Autonomous Systems*, 55(10):761–768, March 2007.
- [102] A. Jafari, N. Tsagarakis, and D. Caldwell. Exploiting natural dynamics for energy minimization using an actuator with adjustable stiffness (awas). In *Proc. 2011 IEEE Int. Conf. Robotics and Automation (ICRA)*, pages 4632–4637, Shanghai, China, 2011.
- [103] J.W. Hurst, J.E. Chestnutt, and A.A. Rizzi. An actuator with physically variable stiffness for highly dynamic legged locomotion. In *Proc. 2004 IEEE Int. Conf. Robotics and Automation (ICRA)*, pages 4662–4667, New Orleans, LA, 2005.
- [104] D.J. Braun, M. Howard, and S. Vijayakumar. Exploiting variable stiffness in explosive movement tasks. In *Robotics: Science and Systems*, Los Angeles, CA, 2011.
- [105] K. Koganezawa, Y. Shimizu, H. Inomata, and T. Nakazawa. Actuator with non linear elastic system (anles) for controlling joint stiffness on antagonistic driving. In *Proc. 2004 IEEE Int. Conf. Robotics and Biomimetics (ROBIO)*, pages 51–55, Shenyang, China, August 2004.
- [106] H. Herr and A. Wilkenfeld. User-adaptive control of a magnetorheological prosthetic knee. *Industrial Robot: An International Journal*, 30(1):42–55, 2003.
- [107] J.A. Blaya and H. Herr. Adaptive control of a variable-impedance ankle-foot orthosis to assist drop-foot gait. *IEEE Transactions on Neural Systems and Rehabilitation Engineering*, 12(1):24–31, March 2004.
- [108] J. Nikitczuk, B. Weinberg, P. Canavan, and Mavroidis. C. Active knee rehabilitation orthotic device with variable damping characteristics implemented via an electrorheological fluid. *IEEE/ASME Transactions on Mechatronics*, 15(6):952–960, 2010.

## BIBLIOGRAPHY

- [109] T.C. Bulea, R. Kobetic, C.S. To, M.L. Audu, J. R. Schnellenberger, and R.J. Triolo. A variable impedance knee mechanism for controlled stance flexion during pathological gait. *IEEE/ASME Transactions on Mechatronics*, 17(5):822–832, 2012.
- [110] D. Chapuis, R.B. de Grave, O. Lambercy, and R. Gassert. ReFlex, a haptic wrist interface for motor learning and rehabilitation. In *IEEE Haptics Symposium*, pages 417–424, 2010.
- [111] S.B. Choi, S.R. Hong, C.C. Cheong, and Y.K. Park. Comparison of field-controlled characteristics between er and mr clutches. *Journal of Intelligent Material Systems and Structures*, 10(8):615–619, 1999.
- [112] G.M. Roach and L.L. Howell. Evaluation and comparison of alternative compliant over-running clutch designs. *Journal of Mechanical Design*, 124(3):485–491, 2002.
- [113] A. Shafer and M. Kermani. On the feasibility and suitability of mr fluid clutches in human-friendly manipulators. *IEEE/ASME Transactions on Mechatronics*, 16(6):1073–1082, 2011.
- [114] Y. Tenzer, B.L. Davies, and F.R.y. Baena. Four-state rotary joint control: Results with a novel programmable brake. *IEEE/ASME Transactions on Mechatronics*, 17(5):915 – 923, 2011.
- [115] H. Lee and Y. Choi. A new actuator system using dual-motors and a planetary gear. *IEEE/ASME Transactions on Mechatronics*, 17(1):192–197, 2012.
- [116] D. Chapuis, X. Michel, R. Gassert, C. Chew, E. Burdet, and H. Bleuler. A haptic knob with a hybrid ultrasonic motor and powder clutch actuator. In *Second Joint EuroHaptics Conference and Symposium on Haptic Interfaces for Virtual Environment and Teleoperator Systems*, pages 200–205, Tsukuba, Japan, March 2007.
- [117] H. Arai and S. Tachi. Position control of manipulator with passive joints using dynamic coupling. *IEEE Transactions on Robotics and Automation*, 7(4):528–534, August 1991.
- [118] J. Gilbert and A. Abu Hassan. Design and control of a multimode drive system. In *Proc. 5th Int. Workshop Adv. Motion Contr.*, page 611–616, Coimbra, Portugal, 1998.
- [119] D. Wollherr, F. Zonfrilli, and Y. Nakamura. Active-passive knee control for the humanoid ut-theta. In *Proc. 2005 Int. Conf. Advanced Robotics (ICAR)*, pages 692–697, 2005.
- [120] G.J. Stein, R. Zaharonský, and P. Múča. On dry friction modelling and simulation in kinematically excited oscillatory systems. *Journal of Sound and Vibration*, 311(1–2):74–96, 2008.
- [121] M. Wiercigroch J. Wojewoda, A. Stefański and T. Kapitaniak. Hysteretic effects of dry friction: Modelling and experimental studies. *Philosoph. Trans. R. Soc. Mathemat. Phys. Eng. Sci.*, 366(1866):747–765, 2008.
- [122] M. Hutter, C. Gehring, C.M. Bloesch, M.A. Hoepflinger, C.D. Remy, and R. Siegwart. Starleth: A compliant quadrupedal robot for fast, efficient, and versatile locomotion. In *Proc. 15th Int. Conf. Climbing and Walking Robot (CLAWAR 2012)*, pages 1–8, Baltimore, MD, 2012.
- [123] D. Koepl and J.W. Hurst. Impulse control for planar spring-mass running. *Journal of Intelligent and Robotic Systems*, 74:589–603, 2014.
- [124] G. Zeglin and B. Brown. A survey of bio-inspired compliant legged robot designs. In *Proc. 1998 IEEE Int. Conf. Robotics & Automation (ICRA)*, pages 1983–1988, Leuven, Belgium, 1998.

- [125] E.J. Rouse, L.M. Mooney, and H.M. Herr. Clutchable series-elastic actuator: Implications for prosthetic knee design. *The International Journal of Robotics Research*, 33(16):1611–1625, 2014.
- [126] J. Zhao, J. Xu, B. Gao, N. Xi, F.J. Cintron, M.W. Mutka, and L. Xiao. Msu jumper: A single-motor-actuated miniature steerable jumping robot. *IEEE Transactions on Robotics*, 29(3):602–614, 2013.
- [127] D.F.B. Haeufle, M.D. Taylor, S. Schmitt, and H. Geyer. A clutched parallel elastic actuator concept: towards energy efficient powered legs in prosthetics and robotics. In *Proc. 2012 IEEE RAS/EMBS Int. Conf. Biomedical Robotics and Biomechatronics*, pages 1614–1619, Rome, Italy, 2012.
- [128] M. Plooij, M. van Nunspeet, M. Wisse, and H. Vallery. Design and evaluation of the bi-directional clutched parallel elastic actuator (bic-pea). *IEEE Robotics & Automation Magazine*, 22(1):106–117, 2015.
- [129] H. Olsson, K.J. Astroem, C. Caudas de Wit, M. Graefvert, and P. Lischinsky. Friction models and friction compensation. *European Journal of Control*, 4(3):176–195, 1998.
- [130] M.D. Berkemeier and K.V. Desai. Control of hopping height in legged robots using a neural-mechanical approach. In *Proc. 1999 IEEE Int. Conf. Robotics & Automation (ICRA)*, pages 1695–1701, Detroit, MI, 1999.
- [131] A. Seyfarth, H. Geyer, M. Guenther, and R. Blickhan. A movement criterion for running. *Journal of Biomechanics*, 35(5):649–655, 2002.
- [132] A. Seyfarth, H. Geyer, and H. Herr. Swing-leg retraction: a simple control model for stable running. *The Journal of Experimental Biology*, 206(15):2547–2555, 2003.
- [133] J.H. Marden. Scaling of maximum net force output by motors used for locomotion. *The Journal of Experimental Biology*, 208(9):1653–1664, 2005.
- [134] M.H. Raibert, H.B. Brown Jr., and M. Chepponis. Experiments in balance with a 3d one-legged hopping machine. *The International Journal of Robotics Research*, 3(2):75–92, 1984.
- [135] M. Reis, X. Yu, N. Maheshwari, and F. Iida. Morphological computation of multi-gaited robot locomotion based on free vibration. *Artificial Life*, 19(1):97–114, 2013.
- [136] X. Yu and F. Iida. Minimalistic models of an energy efficient vertical hopping robot. *IEEE Transactions on Industrial Electronics*, 61(2):1053–1062, 2014.
- [137] B. Mathis. Efficient locomotion of a segmented beam hopper based on free vibration. Master’s thesis, Department of Mechanical and Process Engineering, ETH ZÄjrich, 2013.
- [138] M. Reis and F Iida. Hopping robot based on free vibration of an elastic curved beam. In *Proc. 2011 IEEE/ASME International Conference on Advanced Intelligent Mechatronics (AIM)*, pages 487–493, Budapest, Hungary, 2011.
- [139] Y. Sakagami, R. Watanabe, C. Aoyama, S. Matsunaga, N. Higaki, and K. Fujimura. The intelligent asimo: System overview and integration. In *Proc. 2002 IEEE Int. Conf. Intelligent Robots and Systems (IROS)*, pages 467–472, Lausanne, Switzerland, 2002.
- [140] M. Raibert, K. Blankespoor, G. Nelson, and R. Playter. Bigdog, the rough-terrain quadrupet robot. In *Proc. 17th World Congress, The Int. Federation of Automatic Control*, pages 10822–10825, Seoul, Korea, 2008.

## BIBLIOGRAPHY

- [141] G. Nelson, A. Saunders, N. Neville, B. Swilling, J. Bondaryk, D. Billings, C. Lee, R. Playter, and M. Raibert. Petman: A humanoid robot for testing chemical protective clothing. *Journal of the Robotics Society of Japan*, 30(4):372–377, 2012.
- [142] C. Glocker and C. Studer. Formulation and preparation for numerical evaluation of linear complementarity systems. *Multibody System Dynamics*, 13(4):447–463, 2004.
- [143] D. Renjewski, A. Sprowitz, A. Peekema, M. Jones, and J. Hurst. Exciting engineered passive dynamics in a bipedal robot. *IEEE Transactions on Robotics*, 31(5):1244–1251, 2015.
- [144] R. McN. Alexander. Models and the scaling of energy costs for locomotion. *The Journal of Experimental Biology*, 208:1645–1652, 2005.
- [145] G. Gabrielli and T. Karman. What price speed? *Mechanical Engineering*, 72(10):775–781, 1950.
- [146] V.A. Tucker. The energetic cost of moving about. *American Scientist*, 63:413–419, 1975.
- [147] D. Owaki, M. Koyama, S. Yamaguchi, S. Kubo, and A. Ishiguro. A 2-d passive-dynamic-running biped with elastic elements. *IEEE Transactions on Robotics*, 27(1):156–162, 2011.
- [148] S. Seok, A. Wang, M.Y. Chuah, D. Otten, J. Lang, and S. Kim. Design principles for highly efficient quadrupeds and implementation on the mit cheetah robot. In *Proc. 2013 IEEE Int. Conf. Robotics and Automation (ICRA)*, pages 3307–3312, Karlsruhe, Germany, 2013.
- [149] I. Wanders, G. A. Folkertsma, and S. Stramigioli. Design and analysis of an optimal hopper for use in resonance-based locomotion. In *Proc. 2015 IEEE Int. Conf. Robotics and Automation (ICRA)*, Seattle, WA, pages 5197–5202, 2015.
- [150] R. Ringrose. Self-stabilizing running. In *Proc. 1997 IEEE Int. Conf. Robotics and Automation (ICRA)*, pages 487–493, Albuquerque, NM, 1997.
- [151] J.Y. Jun and E. Clark. Effect of rolling on running performance. In *Proc. 2011 IEEE Int. Conf. Robotics and Automation (ICRA)*, pages 2230–2235, Shanghai, China, 2011.
- [152] K.J. Huang, C.K. Huang, and P.C. Lin. A simple running model with rolling contact and its role as a template for dynamic locomotion on a hexapod robot. *Bioinspir. Biomim.*, 9(4):1–20, 2014.
- [153] A.H. Hansen, D.S. Childress, and E.H. Knox. Roll-over shapes of human locomotor systems: effects of walking speed. *Clinical Biomechanics*, 19:407–414, 2004.
- [154] P.G. Adamczyk, S.H. Collins, and A.D. Kuo. The advantages of a rolling foot in human walking. *The Journal of Experimental Biology*, 209:3953–3963, 2006.
- [155] J. Seipel and P. Holmes. A simple model for clock-actuated legged locomotion. *Regular and Chaotic Dynamics*, 12(5):502–520, 2007.
- [156] T.F. Novacheck. The biomechanics of running. *Gait and Posture*, 7:77–95, 1998.
- [157] T. Kostka. Quadriceps maximal power and optimal shortening velocity in 335 men aged 23–88 years. *Eur J Appl Physiol*, 95:140–145, 2005.
- [158] A.A. Biewener. Pectoralis muscle force and power output during flight in the starling. *Journal of experimental Biology*, 164:1–18, 1992.

- [159] M.N. Scholz, K. D’Aout, M.F. Bobbert, and P. Aerts. Vertical jumping performance of bonobo (*pan paniscus*) suggests superior muscle properties. *Proceedings of the Royal Society B*, 273:2177–2184, 2006.
- [160] T.J. Overend, D.A. Cunningham, J.F. Kramer, M.S. Lefcoe, and D.H. Paterson. Knee extensor and knee flexor strength: Cross-sectional area ratios in young and elderly men. *Journal of Gerontology: Medical Sciences*, 47(6):M204–M210, 1992.
- [161] S.D. Masouros, A.M.J. Bull, and A.A. Amis. (i) biomechanics of the knee joint. *Orthopaedics and Trauma*, 24(2):84–81, 2010.
- [162] D. Leach, F. Günther, N. Maheshwari, and F. Iida. Linear multi-modal actuation through discrete coupling. In *Proc. 2012 IEEE Int. Conf. Robotics and Automation (ICRA)*, pages 2437–2442, Algarve, Portugal, 2012.
- [163] C. Siegenthaler, C. Pradalier, F. Günther, G. Hitz, and R. Siegwart. System integration and fin trajectory design for a robotic sea-turtle. In *Proc. 2013 IEEE/RSJ Int. Conf. Intelligent Robots and Systems (IROS)*, pages 3790–3795, Tokyo, Japan, 2013.





# List of publications

## Journal papers

1. D. Leach, F. Günther, N. Maheshwari, and F. Iida. Linear multimodal actuation through discrete coupling. *IEEE/ASME Transactions on Mechatronics*, 19(3):827–839, 2014
2. F. Guenther, H.Q. Vu, and F. Iida. Improving hopping height control of legged robots by using coupling-based series elastic actuation. *Conditionally accepted for publication in IEEE Transactions on Robotics*
3. F. Guenther and F. Iida. Energy efficient monopod running with large payload based on open loop parallel elastic actuation. *Accepted for publication in IEEE Transactions on Robotics*

## Reviewed conference papers

1. D. Leach, F. Günther, N. Maheshwari, and F. Iida. Linear multi-modal actuation through discrete coupling. In *Proc. 2012 IEEE Int. Conf. Robotics and Automation (ICRA)*, pages 2437–2442, Algarve, Portugal, 2012
2. F. Günther and F. Iida. Preloaded hopping with linear multi-modal actuation. In *Proc. 2013 IEEE/RSJ Int. Conf. Intelligent Robots and Systems (IROS)*, pages 5847–5852, Tokyo, Japan, 2013
3. C. Siegenthaler, C. Pradalier, F. Günther, G. Hitz, and R. Siegwart. System integration and fin trajectory design for a robotic sea-turtle. In *Proc. 2013 IEEE/RSJ Int. Conf. Intelligent Robots and Systems (IROS)*, pages 3790–3795, Tokyo, Japan, 2013
4. F. Günther, F. Giardina, and F. Iida. Self-stable one-legged hopping using a curved foot. In *Proc. 2014 IEEE Int. Conf. Robotics and Automation (ICRA)*, pages 5133–5138, Hong Kong, China, 2014
5. F. Günther, Y. Shu, and F. Iida. Parallel elastic actuation for efficient large payload locomotion. In *Proc. 2015 IEEE Int. Conf. Robotics and Automation (ICRA)*, pages 823–828, Seattle, WA, 2015



# Curriculum vitae

## **Fabian Günther**

born on 25 December 1984, citizen of Germany

- |             |  |
|-------------|--|
| 2000 - 2004 | Gymnasium Köniz<br>Matura  |
| 2005        | KABA Gilgen AG, Schwarzenburg<br>Workshop training   |
| 2004 - 2010 | ETH Zürich<br>BSc ETH in Mechanical Engineering  |
| 2011 - 2013 | Dynamic Devices, Zürich, Switzerland<br>Industrial internship  |
| 2009 - 2013 | ETH Zürich<br>MSc ETH in Mechanical Engineering  |
| 2011 - 2016 | Bio-Inspired Robotics Lab, ETH Zürich<br>Doctoral studies in the group of Prof. Dr. Fumiya Iida at the Institute of Robotics and Intelligent Systems |
| 2014 - 2016 | University of Cambridge, United Kingdom<br>Academic visitor at the department of engineering   |